

Stratified-Medium Sound Speed Profiling for CPWC Ultrasound Imaging

by

Derrell D'Souza

B.E., University of Mumbai, 2016

A Thesis Submitted in Partial Fulfillment of the
Requirements for the Degree of

Master of Applied Science

in the Department of Electrical and Computer Engineering

© Derrell D'Souza, 2020

University of Victoria

All rights reserved. This dissertation may not be reproduced in whole or in part, by photocopying or other means, without the permission of the author.

Stratified-Medium Sound Speed Profiling for CPWC Ultrasound Imaging

by

Derrell D'Souza
B.E., University of Mumbai, 2016

Supervisory Committee

Dr. Daler Rakhmatov, Supervisor
(Department of Electrical and Computer Engineering)

Dr. Kin Fun Li, Departmental Member
(Department of Electrical and Computer Engineering)

Supervisory Committee

Dr. Daler Rakhmatov, Supervisor
(Department of Electrical and Computer Engineering)

Dr. Kin Fun Li, Departmental Member
(Department of Electrical and Computer Engineering)

ABSTRACT

Coherent plane-wave compounding (CPWC) ultrasound is an important modality enabling ultrafast biomedical imaging. To perform CWPC image reconstruction for a stratified (horizontally layered) medium, one needs to know how the speed of sound (SOS) varies with the propagation depth. Incorrect sound speed and layer thickness assumptions can cause focusing errors, degraded spatial resolution and significant geometrical distortions resulting in poor image reconstruction. We aim to determine the speed of sound and thickness values for each horizontal layer to accurately locate the recorded reflection events to their true locations within the medium.

Our CPWC image reconstruction process is based on phase-shift migration (PSM) that requires the user to specify the speed of sound and thickness of each layer in advance. Prior to performing phase-shift migration (one layer at a time, starting from the surface), we first estimate the speed of sound values of a given layer using a cosine similarity metric, based on the data obtained by a multi-element transducer array for two different plane-wave emission angles. Then, we use our speed estimate to identify the layer thickness via end-of-layer boundary detection. A low-cost alternative that obtains reconstructed images with fewer phase shifts (i.e., fewer complex multiplications) using a spectral energy threshold is also proposed in this thesis.

Our evaluation results, based on the CPWC imaging simulation of a three-layer medium, show that our sound speed and layer thickness estimates are within 4% of their true values (i.e., those used to generate simulated data). We have also confirmed the accuracy of our speed and layer thickness estimation separately, using two experimental datasets representing two special cases. For speed estimation, we used

a CPWC imaging dataset for a constant-speed (i.e., single-layer) medium, yielding estimates within 1% of their true values. For layer thickness estimation, we used a monostatic (i.e., single-element) synthetic-aperture (SA) imaging dataset of the three-layer medium, also yielding estimates within 1% of their true values. Our evaluation results for the low-cost alternative showed a 93% reduction in complex multiplications for the three-layer CPWC imaging dataset and 76% for the three-layer monostatic SA imaging dataset, producing images nearly similar to those obtained using the original PSM methods.

Contents

Supervisory Committee	ii
Abstract	iii
Table of Contents	v
List of Tables	viii
List of Figures	x
List of Acronymns	xii
Acknowledgements	xiii
Dedication	xiv
1 Introduction	1
1.1 Ultrasound imaging system	1
1.2 Ultrasound concepts	4
1.2.1 Speed and Frequency	4
1.2.2 Interaction of ultrasound with matter	5
1.3 Ultrasound beamforming	6
1.3.1 Synthetic-aperture beamforming	7
1.3.2 Plane-wave beamforming	8
1.4 Ultrasound image quality	10
1.4.1 Spatial resolution	10
1.4.2 Temporal resolution	11
1.4.3 Contrast resolution	11
1.5 Thesis contribution and organization	12

2 Background	13
2.1 Phase-shift migration	13
2.1.1 Overview of the PSM method by Gazdag	13
2.1.2 Phase-shift migration for PW imaging	16
2.1.3 Phase-shift migration for SA imaging	20
2.2 Outstanding Issues	21
2.3 Related Work	22
3 SOS Profiling for CPWC Imaging	26
3.1 Problem formulation	26
3.2 Our approach	27
3.2.1 Sound speed estimation	27
3.2.2 Layer thickness estimation	30
3.2.3 Layer post-processing	32
3.3 Computational cost reduction	32
3.4 Computational complexity	33
4 Evaluation Results	35
4.1 Evaluation results for SOS profiling in CPWC imaging	35
4.1.1 Experimental setup	35
4.1.2 Results and discussion	39
4.2 Evaluation results for layer thickness estimation in SA imaging	50
4.2.1 Dataset description	50
4.2.2 Results and discussion	52
4.3 Evaluation results for sound speed estimation in single-layer CPWC imaging	58
4.3.1 Dataset description	58
4.3.2 Results and discussion	59
4.4 Summary	62
5 Conclusion and Future work	64
5.1 Conclusion	64
5.2 Future work	65
A Imaged target cross-sections after SOS profiling	67
B Overview of Hough transform	75

B.1 Theory	75
B.2 Implementation	76
Bibliography	77

List of Tables

1.1	Ultrasound-related properties of different materials	6
3.1	Computational complexity of SOS profiling in PWPSM	34
4.1	Location (x, z) of point targets (in mm) inside the three-layer medium	36
4.2	Propagation medium specifications	36
4.3	Different cases for SOS profiling in CPWC imaging	39
4.4	Target resolution quality for true SOS profile	40
4.5	Estimated speed and thickness, case 1	42
4.6	Estimated speed and thickness, case 2	43
4.7	Estimated speed and thickness, case 3	44
4.8	Estimated speed and thickness, case 4	45
4.9	Estimated speed and thickness, case 5	46
4.10	Estimated speed and thickness, case 6	47
4.11	Estimated speed and thickness, case 7	48
4.12	Estimated speed and thickness, case 8	49
4.13	CPWC image similarity when using estimated vs. true SOS profile .	50
4.14	True SOS profile for SA imaging dataset	51
4.15	Different cases for thickness estimation in SA imaging.	52
4.16	Thickness estimates, case 1	54
4.17	Thickness estimates, case 2	55
4.18	Thickness estimates, case 3	56
4.19	Thickness estimates, case 4	57
4.20	SA image similarity when using estimated vs. true SOS profile . .	58
4.21	Speed estimates for PW Stolt's migration	61
4.22	Constant-velocity image similarity using estimated vs. 1540 m/s speed	61
A.1	Target resolution quality for estimated SOS profile, case 1	68
A.2	Target resolution quality for estimated SOS profile, case 2	68

A.3	Target resolution quality for estimated SOS profile, case 3	69
A.4	Target resolution quality for estimated SOS profile, case 4	70
A.5	Target resolution quality for estimated SOS profile, case 5	71
A.6	Target resolution quality for estimated SOS profile, case 6	72
A.7	Target resolution quality for estimated SOS profile, case 7	73
A.8	Target resolution quality for estimated SOS profile, case 8	74

List of Figures

1.1	Functional block diagram of an ultrasound imaging system	2
1.2	Synthetic-aperture (SA) imaging	7
1.3	Plane-wave (PW) Imaging	8
1.4	Coherent plane-wave compounding	9
2.1	Application of exploding reflecting model to ultrasound	14
2.2	Depth and travel-time corrections for PW emission $\theta \neq 0$	17
2.3	Multilayered propagation medium	19
3.1	Proposed method for SOS profiling	29
3.2	Downward extrapolation during SOS profiling	30
4.1	Emitted PW pulse	36
4.2	Simulation layout for CPWC imaging setup	37
4.3	Processing steps for CPWC imaging setup	38
4.4	Migration results using true SOS profile	41
4.5	Migration results using estimated SOS profile, case 1	42
4.6	Migration results using estimated SOS profile, case 2	43
4.7	Migration results using estimated SOS profile, case 3	44
4.8	Migration results using estimated SOS profile, case 4	45
4.9	Migration results using estimated SOS profile, case 5	46
4.10	Migration results using estimated SOS profile, case 6	47
4.11	Migration results using estimated SOS profile, case 7	48
4.12	Migration results using estimated SOS profile, case 8	49
4.13	Experimental setup for SA imaging	51
4.14	Migration results using true thickness	53
4.15	Migration results using estimated thickness, case 1	53
4.16	Migration results using estimated thickness, case 2	54
4.17	Migration results using estimated thickness, case 3	55

4.18	Migration results using estimated thickness, case 4	56
4.19	Migrated carotid artery images using true speed	59
4.20	Migrated carotid artery images using estimated speed (stacking-based vectorization)	60
4.21	Migrated carotid artery images using estimated speed (summing-based vectorization)	60
A.1	Lateral cross-section for estimated SOS profile, case 1	67
A.2	Lateral cross-section for estimated SOS profile, case 2	68
A.3	Lateral cross-section for estimated SOS profile, case 3	69
A.4	Lateral cross-section for estimated SOS profile, case 4	70
A.5	Lateral cross-section for estimated SOS profile, case 5	71
A.6	Lateral cross-section for estimated SOS profile, case 6	72
A.7	Lateral cross-section for estimated SOS profile, case 7	73
A.8	Lateral cross-section for estimated SOS profile, case 8	74
B.1	Parametric Hough transform	76

List of Acronyms

CPWC	Coherent Plane Wave Compounding
ERM	Exploding Reflector Model
LCPSM	Low-cost Phase-Shift Migration
LCPWPSM	Low-cost Plane Wave Phase-Shift Migration
LCSAPSM	Low-cost Synthetic Aperture Phase-Shift Migration
PICMUS	Plane-wave Imaging Challenge in Medical UltraSound
PSM	Phase-Shift Migration
PW	Plane Wave
PWPSM	Plane Wave Phase-Shift Migration
RF	Radio Frequency
SOS	Speed of Sound
SA	Synthetic Aperture
SAPSM	Synthetic Aperture Phase-Shift Migration
SNR	Signal-to-Noise Ratio

ACKNOWLEDGEMENTS

First and foremost, I would like to thank my supervisor Dr. Daler Rakhmatov whose patience, valuable guidance and suggestions have immensely helped me throughout my graduate studies. I am also grateful to Dr. Kin Fun Li for his time serving as the member of the supervisory committee and for his valuable suggestions to improve my thesis.

I would also like to thank my family and friends for their love and emotional support.

Finally, I would like to thank the Almighty for the wisdom, strength and countless blessings he has bestowed upon me.

DEDICATION

To my parents, Mark and Lenny.

Chapter 1

Introduction

Ultrasound (US) imaging is a technique for obtaining subsurface images with ultrasound, i.e., high-frequency sound waves above human hearing capability ($> 20\text{kHz}$). It involves interaction of such waves with specific targets inside the insonified medium to produce images revealing structural and functional information about the target. In this context, ultrasound is used in a variety of applications including medical imaging, underwater acoustic imaging, non-destructive testing (NDT) and evaluation, material characterization, and sonochemistry [1, 2]. Such an extensive use of ultrasound is a proof of the unique benefits it offers compared to other imaging technologies. Some of its main advantages include real-time imaging capability, high sensitivity and penetrating depth, safety (radiation-free), portability, non-invasiveness, and low cost.

In this chapter, we provide an overview of the ultrasound imaging system and a brief insight into some fundamental concepts of ultrasound imaging.

1.1 Ultrasound imaging system

A simple functional block diagram of an ultrasound imaging system is shown in Figure 1.1. The transmit beamformer generates excitation pulses which are timed and scaled to insonify desired subsurface areas. These pulses are passed through a digital-to-analog converter (DAC), where digital transmit beamformed signals are converted to low amplitude analog signals. A high-voltage (HV) amplifier amplifies these pulses to a higher level before they reach the transducer elements. A transmit/receive switch is placed between transmit circuitry and receive circuitry to ensure protection of

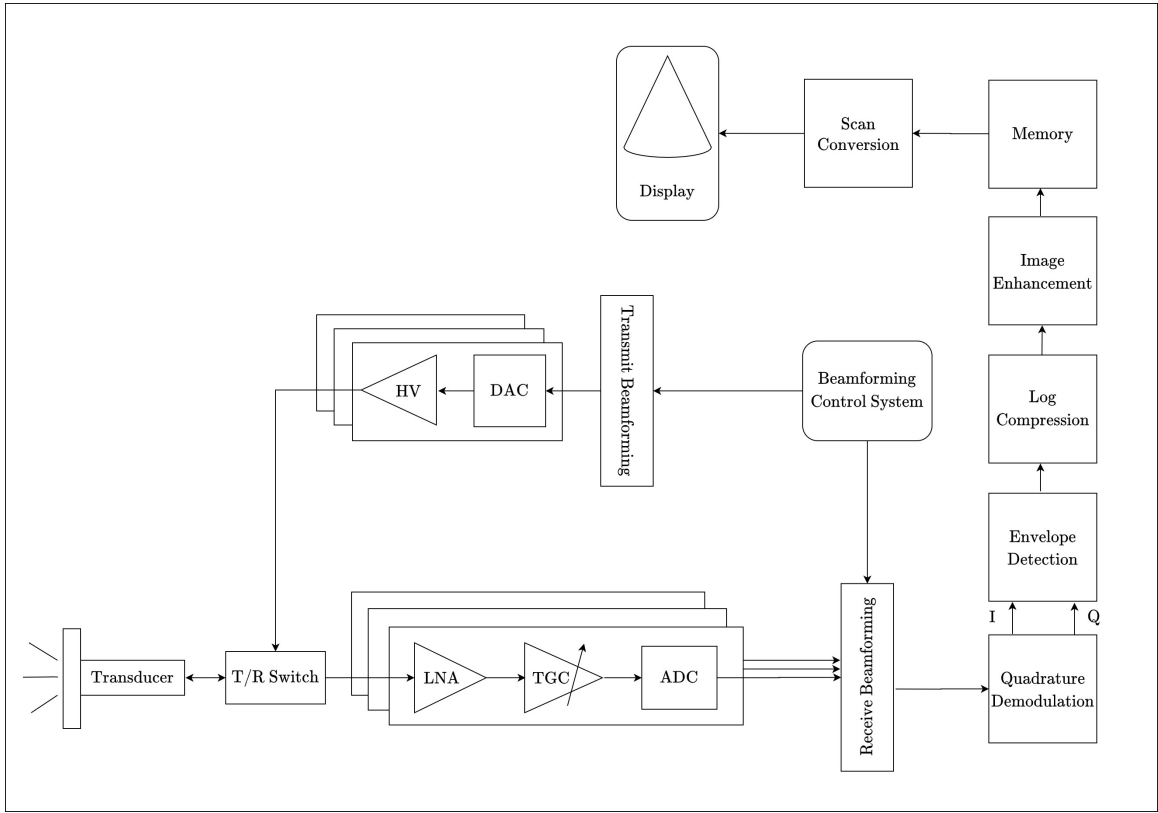


Figure 1.1: Functional block diagram of an ultrasound imaging system.

low-voltage receive circuitry from the high-voltage of transmit circuitry [3].

The transducer is an array of piezoelectric elements which converts electrical signals into acoustic waves that propagate through the medium. Within the medium, these acoustic waves encounter different targets with different acoustic impedances that cause reflections from their boundaries. The resultant backscattered echoes are sensed and converted to electrical signals by the transducer elements [2]. These received echoes are frequency and depth dependent. Because of frequency-dependent attenuation of the echoes, the resultant electrical signals have low voltage.¹ A low-noise amplifier (LNA) improves the signal-to-noise ratio (SNR) of the electrical signals by performing amplification while maintaining a very low noise level so that masking of the signal of lower amplitudes is avoided. The LNA output is then amplified by a time-gain compensation (TGC) amplifier to compensate for the amplitude loss caused

¹For instance, in soft tissues, the acoustic wave attenuates at a rate of 0.5 dB/MHz-cm. Typical ultrasound systems operate in the carrier frequency range of 2 – 15 MHz to minimize the effects of frequency dependent attenuation [4].

due to the attenuation during sound propagation in the medium [5]. The resulting analog signals are finally digitized using an analog-to-digital converter (ADC) and are fed to a receive beamformer.

In the receive beamformer, the received digitized signals are coherently summed together (typically using a delay-and-sum beamforming method) to increase the SNR and spatial resolution. This beamformed signal undergoes quadrature demodulation forming a complex baseband signal. Envelope of the baseband signal is detected by simply taking its absolute value. The obtained envelope signal is logarithmically compressed to reduce its dynamic range for an output display. To improve the image quality, several image enhancement and filtering techniques are applied to the compressed envelope signal. The signals are stored in the memory bank and scan converted (if needed) into a real-time output image with the Cartesian raster coordinates [2, 5].

Depending on the echo principle, there are several imaging modes as outlined below.

- A-mode: In A-mode imaging, A stands for ‘Amplitude’. Here, the transducer sends a single ultrasound pulse into the medium that results in a one-dimensional series of returning echoes reflected from the boundary of various tissues [6].
- B-mode: In B-mode imaging, B stands for ‘Brightness’. Here, the area is simultaneously scanned by an array of piezoelectric elements resulting in a two-dimensional ultrasound image with grayscale intensity indicating the echo amplitude [6, 7].
- C-mode: In C-mode, C stands for ‘Constant depth’. Here, the image plane is perpendicular to the sound wave, and echoes are received only from a certain depth using an A-mode line. A cross-sectional image is created with 2-D scanning of the entire region by the transducer [8].
- M-mode: In M-mode, M stands for ‘Motion’. Here an A-mode line, placed over the structure of interest in a B-mode image, is recorded continuously over time to produce a picture with a motion signal. This enables the movement of structures to be represented in a dynamic wave-like manner [6, 7].
- Doppler mode: This mode is based on the Doppler principle, capturing a change in frequency of a sound wave due to relative motion between the sound

source and the receiver. Doppler mode comprises of continuous-wave Doppler, where ultrasound signal is transmitted and received continuously, pulsed-wave Doppler, where short intermittent bursts of ultrasound are transmitted and their echoes are received afterwards, and color Doppler that produces a color-coded map of Doppler shifts superimposed onto a B-mode ultrasound image [6, 7].

Our work is concerned with B-mode imaging which will be the focus of this thesis.

1.2 Ultrasound concepts

It is important to understand the various concepts involved in the functioning of an ultrasound system. Below, we give an overview of some of them.

1.2.1 Speed and Frequency

Ultrasound speed is the rate at which the ultrasound wave propagates through the medium. Ultrasound waves are mechanical disturbances containing compressions (zones of high pressure) and rarefactions (zones of low pressure) that are transmitted through a medium [9, 10]. Such a periodically fluctuating pressure wave can be conveniently represented as a sinusoidal wave. The speed of sound c is related to frequency f and wavelength λ by the following relation:

$$c = f\lambda . \quad (1.1)$$

The wavelength λ refers to the distance between two consecutive, identical positions on the sinusoidal wave, whereas the frequency f refers to the number of cycles of the pressure wave per unit time. The frequency range commonly applied for medical imaging is about 1-20 MHz, whereas the frequency range normally employed in ultrasonic nondestructive testing and evaluation is 100 kHz to 50 MHz [11]. The material properties that determine the sound speed include, density ρ and stiffness κ . Mathematically, this can be expressed as

$$c = \sqrt{\frac{\kappa}{\rho}} . \quad (1.2)$$

1.2.2 Interaction of ultrasound with matter

When ultrasound waves travel through a material, they are partly transmitted to a greater depth, partly reflected back to the transducer as echoes, partly scattered and partly absorbed [11, 12]. The amount of energy transmitted and reflected at each interface depends on the difference in acoustic impedance of the media on each side of that interface [13]. The acoustic impedance Z of a material is the opposition offered to the displacement of its particles by sound [7, 11]. It is given by

$$Z = \rho c , \quad (1.3)$$

where ρ is the material density. The boundary between materials of different acoustic impedances is known as the acoustic interface. The percentage of the wave energy reflected at an interface is given by its reflection coefficient:

$$R = \left(\frac{Z_1 - Z_2}{Z_1 + Z_2} \right)^2 . \quad (1.4)$$

For example, if $Z_1 = 7.8$ (bone) and $Z_2 = 1.69$ (soft tissue), then $R = 0.41$. This implies that 41% of the sound energy is reflected and 59% is transmitted.

When the ultrasound beam passes through the medium, the direction of the beam changes after hitting the interface of two materials with different sound speeds. This change in direction of sound transmission is called refraction. Refraction may result in incorrect localization of objects in an ultrasound image.²

The energy of the ultrasound beam decreases exponentially as it passes through the medium. This exponential loss of energy is called attenuation. The ultrasound beam loses a constant fraction of energy per unit length of travel determined by the following equation:

$$A(x) = A_0 e^{-\alpha x} , \quad (1.5)$$

where A is the amplitude of the sound wave, A_0 is the initial amplitude of the sound wave, α is the attenuation coefficient, and x is the distance traveled by the sound wave. The two main contributors to attenuation are absorption and scattering. Absorption results in the localized heating due to induced oscillatory motion in the material produced by the ultrasound beam. Scattering occurs if the ultrasound beam

²For instance, since the speed of sound is low in soft tissue (approximately 1540 m/s) and higher in bone (approximately 4080 m/s), refraction artifacts are prominent at bone-tissue interfaces [12].

encounters reflectors having dimensions smaller than the wavelength or due to a rough, irregular interface. This results in echoes getting reflected through a wide range of angles reducing their intensity [12, 13]. Other factors affecting attenuation include the medium properties, distance traveled, and the beam frequency [9]. High-frequency sound waves attenuate faster than low-frequency sound waves. Table 1.1 shows typical values of sound velocity, acoustic impedance and attenuation coefficient for various materials.

Material	Speed of sound, m/s	Acoustic impedance, MRayl	Attenuation coeff., dB/cm at 1 MHz
Air	330	0.0004	1.38
Water	1430	1.43	0.0025
Soft tissue	1540	1.69	0.5-1.0
Liver	1570	1.65	1.1
Fat	1450	1.38	0.6
Bone	4080	7.8	10.0
Aluminium	6420	17	0.021

Table 1.1: Ultrasound-related properties of different materials [13].

1.3 Ultrasound beamforming

Beamforming is a signal processing technique in ultrasound systems to manage the ultrasound beam generation, steering and focusing [14]. For focusing, appropriate delays are applied to the individual elements to achieve maximum constructive interference at the focal point. The delay applied varies according to the depth of the focal point. While a transmit beam can only be focused at a single depth, dynamic receive focusing can be used at the receive beamformer to focus the receive beam in a depth-dependent manner, since the signal from larger depths arrives later than the signal from closer distances [15, 16]. Beamforming optimization is important to maximize the signal-to-noise ratio, contrast, and resolution of the final image, while limiting as much as possible off-axis interferences to reject clutter and noise [17]. Below, we discuss synthetic-aperture beamforming and plane-wave beamforming.

1.3.1 Synthetic-aperture beamforming

Synthetic-aperture (SA) imaging involves the transmission of the wave into a region of interest, recording backscattered echoes, and repeating this for several positions. The

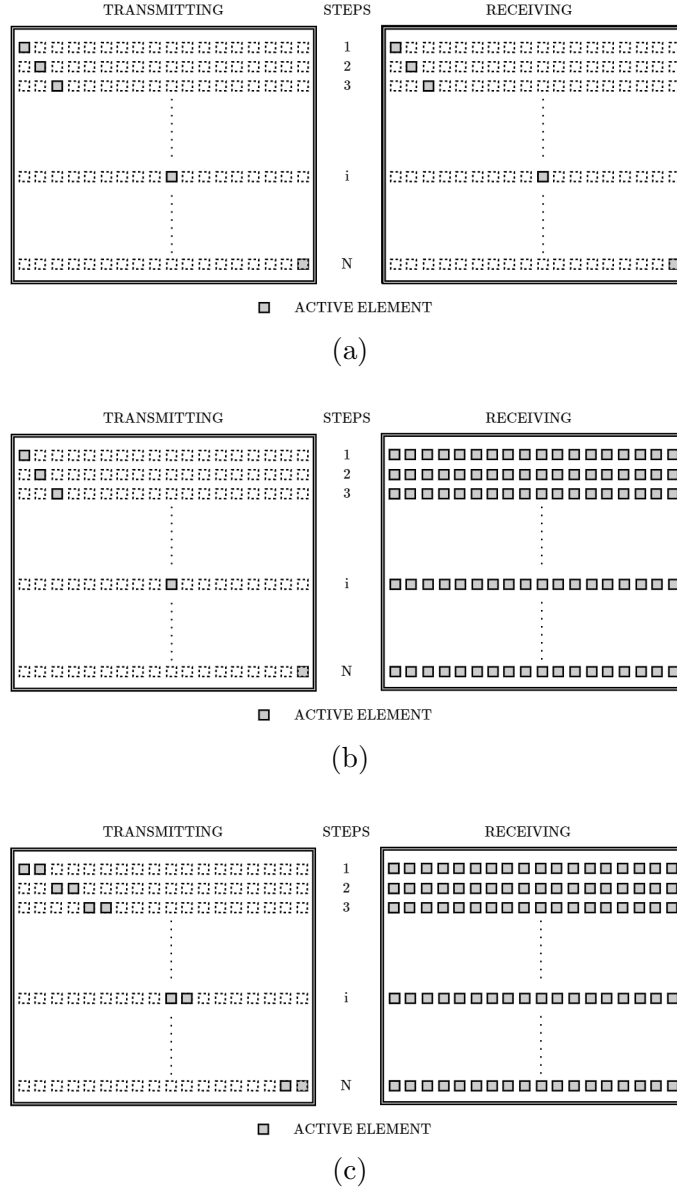


Figure 1.2: Synthetic-aperture (SA) imaging. (a) Monostatic SA imaging, (b) Single-transmit SA imaging, (c) Multi-transmit SA imaging.

recorded data is combined to create a larger synthetic aperture, resulting in a high-resolution image of reflectivity in the scanned region [18]. In monostatic SA imaging, one element is used to transmit a pulse, and the same element will receive the echo

signal. These systems usually have low complexity, cost, and spatial requirements. In the single-transmit SA imaging, one array element transmits a pulse, and all elements receive the echo signals. In these systems, full dynamic focusing can be applied during transmission and reception, giving the highest quality image. In the multi-transmit SA imaging, a small number of array elements are used to transmit a pulse, but all array elements receive the echo signal. This results in increased lateral resolution and system frame rate and a higher penetration depth [19].

1.3.2 Plane-wave beamforming

Instead of transmitting a focused beam, that scans the entire region of interest line-by-line, plane-wave (PW) imaging uses plane waves to insonify a large field of view in a single transmission and then forms an image from resultant backscattered echoes. Such a method effectively increases frame rate more than 100 times relative to the focused beam method [17]. The basic concept here is to reduce the number of trans-

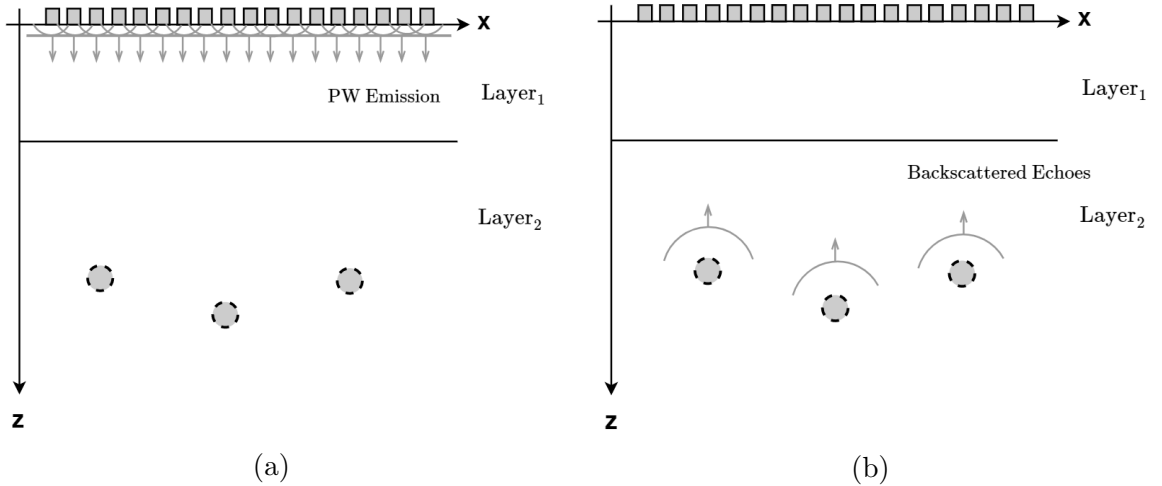


Figure 1.3: Plane-wave (PW) Imaging. (a) PW Emission, (b) Receiving backscattered echoes.

missions to increase the frame rate [20]. As shown in Figure 1.3(a), all the available transducer elements are simultaneously excited to transmit a PW pulse. The resultant backscattered echoes are collected by all the active transducer elements, as shown in Figure 1.3(b). This eliminates the need for scan lines due to an increased scan area coverage [21].

Due to the lack of focusing step during transmission, single-PW imaging suffers from reduced contrast, SNR, and resolution. To resolve this, one can use coherent

plane-wave compounding (CPWC) illustrated in Figure 1.4, where several tilted plane waves are sequentially transmitted, and then beamformed frames obtained from each insonification are summed (before envelope detection) to form a final compounded frame. In this way, the gain in frame rate is reduced by a factor equal to the number

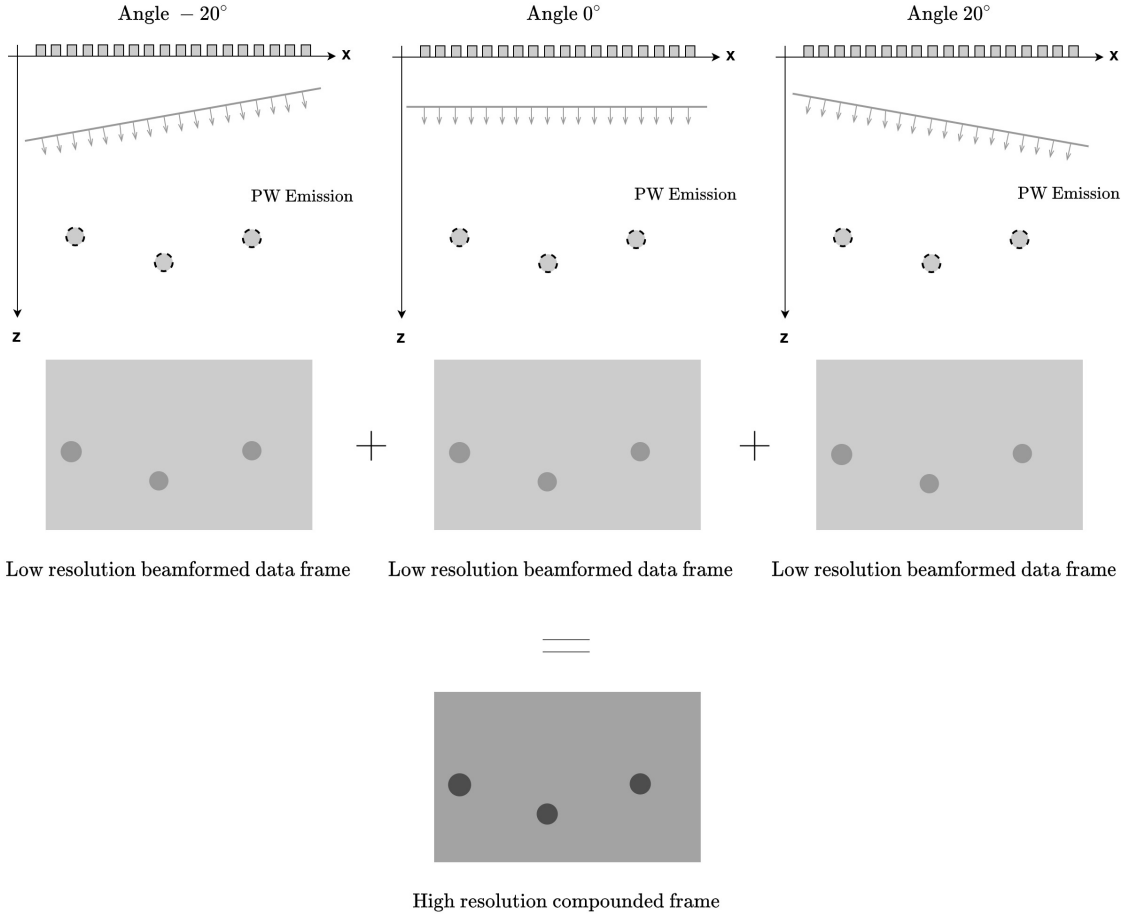


Figure 1.4: Coherent plane-wave compounding.

of angles used [20]. Compared to single-PW imaging, CPWC trades off higher frame rate for higher image resolution. Such an acquisition still enables measurements of fast-paced dynamics with frame rates in the order of hundreds or even thousands of frames per second [15, 17, 22]. The resultant image is characterized by significantly improved contrast, SNR, and resolution since CPWC effectively generates a posteriori synthetic focusing in the transmission [23].

1.4 Ultrasound image quality

Ultrasound image formation refers to the entire process of image reconstruction, starting from the transmission strategy to the reception of signals, beamforming, and image processing [14]. The overall quality of the ultrasound image is the result of many factors.

Resolution in ultrasound imaging can be defined as the ability of the ultrasound system to distinguish backscattered echoes in terms of space, time, or strength. A good resolution is essential to produce high-quality images [9, 24]. Components of resolution include spatial resolution, temporal resolution, and contrast resolution [10].

1.4.1 Spatial resolution

Spatial resolution is the ability of the ultrasound system to detect and display structures that are close together. It affects the imaging system's capability to capture structural details. Since an ultrasound imaging system depicts a 2D section (along its depth and across its width), there are two types of spatial resolution: axial and lateral.

Axial resolution is the ability of the ultrasound system to detect and display targets along the path of the ultrasound beam as separate entities [9, 12]. Mathematically, axial resolution is equal to half the spatial pulse length (SPL), defined as the distance that pulse occupies in space from the start to the end of the said pulse. It is the product of the number of cycles in a pulse M and the wavelength λ [24]. Therefore, we can write the axial resolution as

$$\Delta z = \frac{\text{SPL}}{2} = \frac{M\lambda}{2} = \frac{Mc}{2f}. \quad (1.6)$$

From (1.6), it is evident that higher frequency waves lead to better axial resolution; however, it comes at a cost of decreased depth of penetration due to attenuation.

Lateral resolution is the ability of the ultrasound system to detect and display targets that are positioned perpendicular to the path of the ultrasound beam as separate entities. It is affected by the beam width, beam frequency, and scan line density. Higher beam frequency results in a better lateral resolution, since the beam can be made narrower at higher frequencies, although one has to be careful of the beam attenuation at these frequencies. Sampling the target at close intervals results in a higher scan line density, which improves lateral resolution. Lateral resolution is

equal to the beamwidth in the scan plane [10, 24]. The 3-dB beamwidth, also known as full-width at half-maximum, is determined by the width D of the aperture, the imaging depth z of interest, and the wavelength λ of the transmitted pulse [25]. It is given as

$$w_{3dB} = \frac{\lambda z}{D} = \lambda F\# , \quad (1.7)$$

where $F\# = z/D$ represents the F-number, which is used to maintain constant resolution in the entire image and control directivity in the near field by preventing elements from the edges contributing to the image. A lower F-number, yields a narrower beam, i.e., improved lateral resolution and shorter depth of field. A higher F-number yields a wider beam with a longer depth of field.

1.4.2 Temporal resolution

Temporal resolution is defined as the ability of the ultrasound system to distinguish between instantaneous events associated with the rapidly moving structures. A higher frame rate results in a higher temporal resolution. The frame rate can be improved by reducing penetration depth, reducing scan line density, and reducing the number of focal points [24]. Frame rate is given by

$$\text{Frame Rate} = \frac{\text{PRF}}{N_f N_s} = \frac{c}{2dN_f N_s} , \quad (1.8)$$

where $\text{PRF} = c/2d$ is the pulse repetition frequency, d is the penetration depth, N_f is the number of foci, and N_s is the number of scan lines.

1.4.3 Contrast resolution

Contrast resolution is defined as the ability of the ultrasound system to distinguish between amplitudes of the adjacent structures. The imaging system electronics and the contrast properties of display and the recording devices largely affect contrast resolution. Contrast resolution may be altered at various stages of the image processing flow by compression of the range of reflected ultrasound amplitudes, the number of bits per pixel, and the use of contrast agents [10, 15].

1.5 Thesis contribution and organization

The subject of this thesis falls into the area of CPWC ultrasound imaging of a stratified (i.e., horizontally layered) medium. Given the sound speed and thickness of each horizontal layer, one can obtain compounded B-mode images using the recently proposed PW phase-shift migration (PSM) method, which we shall utilize in this work. During PSM, assumed speed of sound and thickness values differing from their true values can cause spatial shifts and distortion in the appearance of various identifiable structures. Hence, it is desirable to have a technique that can accurately estimate an SOS profile (i.e., the sound speed and thickness of each layer) in a stratified medium prior to image reconstruction. Using this as a motivation for our work, we propose an iterative approach to SOS profiling.

The rest of this thesis is organized as follows. A summary of PSM and its application to PW and SA imaging are presented in Chapter 2. Subsequently, we also highlight main PSM drawbacks and briefly review the existing solutions to SOS profiling problem in US imaging.

In Chapter 3, we present an iterative PSM-based approach to SOS profiling specifically tailored to CPWC imaging of a stratified medium. A brief discussion on the associated computational costs is presented, followed by the description of a low-cost version of our proposed SOS profiling method. We also present the computational complexity analysis of our proposed PSM-based SOS profiling.

In Chapter 4, we provide evaluation results involving three different datasets. First, we use the simulated CPWC data for the three-layer medium (tissue-bone-tissue) to assess the accuracy of our estimates of each layer's sound speed and thickness. Second, we use the experimental monostatic SA data for the three-layer medium (water-glass-metal) to separately assess the accuracy of our estimates of each layer's thickness. Third, we use the experimental CPWC data for a single-layer medium (tissue) to separately assess the accuracy of our sound speed estimates. For the two multi-layer datasets we also demonstrate how our low-cost version performs in comparison to our original PSM-based SOS profiling method.

Finally, in Chapter 5, we draw conclusions of our study and outline possible directions for future work.

Chapter 2

Background

In the previous chapter, we discussed the ultrasound imaging system, the beam-forming process, and the various parameters that affect the quality of an ultrasound image. In this chapter, we discuss the PSM method and its application to image reconstruction in PW and SA imaging. We also briefly discuss the issue of erroneous mismatch between true and assumed layer boundaries and sound speeds during image reconstruction and provide an overview of existing methods aimed at solving this problem.

2.1 Phase-shift migration

Migration is a process that removes distortions from reflection records by relocating point scatterers in either space or time to their true location (as opposed to their apparent locations) to reconstruct an accurate image of the subsurface [26]. When the downward wave reaches a single point scatterer, the latter becomes a secondary source emitting upward spherical waves. In general, each point scatterer within the insonified medium generates a diffraction hyperbola. In order to produce an image of the scatterers, these diffraction hyperbolas need to be focused back to their original sources [25, 27].

2.1.1 Overview of the PSM method by Gazdag

The PSM method introduced by Gazdag [28] is useful for migration of records in vertically inhomogeneous media. Unlike methods that assume the sound speed to be

constant in a propagation medium [27, 29], phase-shift migration accounts for vertical depth-dependent velocity variations in a horizontally layered medium [30].

The zero-offset PSM works under the exploding reflector model (ERM) assumptions, where a two-way pulse propagation scenario is reduced to a one-way scenario as shown in figure 2.1 [18]. Here, the scatterers are considered to be sources of acoustic energy. Figure 2.1(a) represents the B-scan measurement of a two-layer medium where a transducer scans along the x -axis performing pulse-echo measurement for each x -position. Consider a receiver located at $(x_1, 0)$ associated with a transmitter at the same location. Let a scatterer be located in the second layer at (x_2, z) and produce a reflected wave. Since both the layers have different wave velocities, the transmitted and reflected waves are refracted at the interface between those layers. When the transmitter's point-source emissions reach the reflector, its “explosion” essentially models the generation of backscattered echoes. Figure 2.1(b) shows the ERM application. Here, the scatterer is assumed to spontaneously radiate a wave that travels towards the transducer array. By letting $t = 0$ mark the “explosion” time, transmitter-to-reflector (downward) propagation delay is neglected. Instead, this delay is accounted for by considering only the one-way propagation at half speed (from the reflector to the array), which is layer-dependent [30].

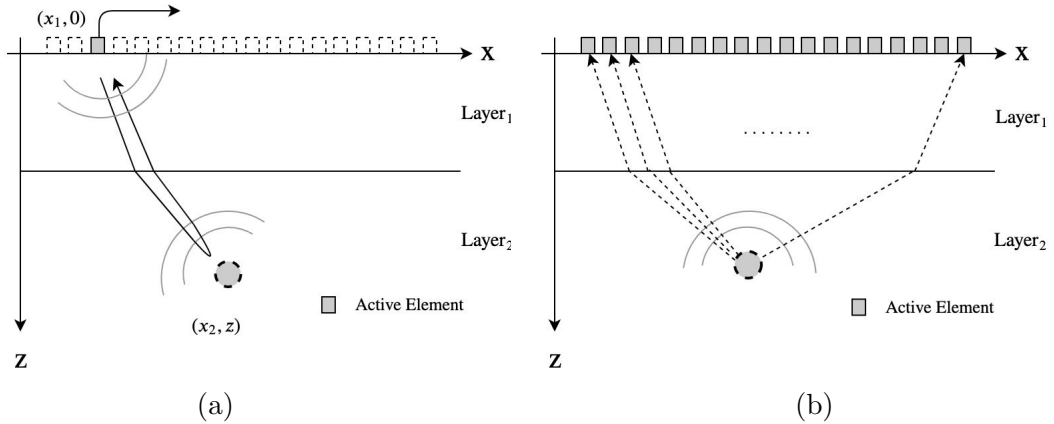


Figure 2.1: Application of exploding reflecting model to ultrasound. (a) Pulse-echo measurements, (b) Exploding reflector model.

Let $P(x, z, t)$ represent a wavefield generated by a set of exploding reflectors that

satisfies the following wave equation:

$$\left[\frac{\partial^2}{\partial x^2} + \frac{\partial^2}{\partial z^2} \right] P(x, z, t) - \frac{1}{\hat{v}_z^2} \frac{\partial^2}{\partial t^2} P(x, z, t) = 0 . \quad (2.1)$$

Here, the x -axis represents the surface line of the array of transducer elements, z -axis represents the imaging depth, t -axis represents the time, and $\hat{v}_z = c_z/2$ represents the effective upward propagation speed at depth z under ERM assumptions.

We want to obtain the wavefield at the time of explosion $P(x, z, t = 0)$ from the knowledge of the recorded wavefield at the surface $P(x, z = 0, t)$. The wavefield $P(x, z, t)$ can be also written as

$$P(x, z, t) = \iint \Psi(k_x, z, f) e^{j2\pi(k_x x + ft)} dk_x df , \quad (2.2)$$

where $\Psi(k_x, z, f)$ is the two-dimensional Fourier transform of $P(x, z, t)$, k_x and f represent the corresponding spatial and temporal frequencies. Then, (2.1) can be written as follows:

$$\left[\frac{\partial^2}{\partial z^2} + 4\pi^2 k_z^2 \right] \Psi(k_x, z, f) = 0 , \quad (2.3)$$

where

$$k_z^2 = \left(\frac{f}{\hat{v}_z} \right)^2 - k_x^2 . \quad (2.4)$$

Here, k_z denotes the spatial frequencies along the z -axis. Assuming that the velocity \hat{v}_z does not change within a propagation medium layer extending from z to $z + \Delta z$, the solution to (2.3) can be expressed as

$$\Psi(k_x, z + \Delta z, f) = \Psi(k_x, z, f) e^{j2\pi k_z \Delta z} , \quad (2.5)$$

where Δz is the discretization step along the z -axis and

$$k_z = \left(\frac{f}{\hat{v}_z} \right) \sqrt{1 - \frac{\hat{v}_z^2 k_x^2}{f^2}} , \quad f^2 > \hat{v}_z^2 k_x^2 . \quad (2.6)$$

The restriction $f^2 > \hat{v}_z^2 k_x^2$ excludes the evanescent wavefield region and requires $f \neq 0$. Note that $\Delta z > 0$ is positive and the sign of k_z coincides with the sign of f which means (2.5) describes a downward wavefield extrapolation process. In other words, we can compute the desired wavefield spectrum $\Psi(k_x, z + \Delta z, f)$ by extrapolating the recorded wavefield spectrum $\Psi(k_x, z = 0, f)$. This is achieved by applying appropriate

phase shifts iteratively using the extrapolation operator $e^{j2\pi k_z \Delta z}$. Then, the explosion wavefield at $z + \Delta z$ is given by

$$P(x, z + \Delta z, t = 0) = \iint [\Psi(k_x, z, f) e^{j2\pi k_z \Delta z}] e^{j2\pi k_x x} dk_x df. \quad (2.7)$$

Computing $P(x, z + \Delta z, t = 0)$ involves three steps:

1. Determine k_z according to (2.6).
2. Multiply $\Psi(k_x, z, f)$ by the extrapolation operator $e^{j2\pi k_z \Delta z}$.
3. Apply inverse Fourier transform with respect to k_x and integrate over all temporal frequencies f . Alternatively, one can integrate $\Psi(k_x, z, f) e^{j2\pi k_z \Delta z}$ over the f -axis first before applying the inverse Fourier transform along the k_x -axis.

For the special case where $\hat{v}_z = \hat{v} = c/2$ throughout the entire propagation medium, (2.7) can be simplified as

$$P(x, z, t = 0)|_{[\hat{v}_z = \hat{v} = c/2]} = \iint_{f^2 > \hat{v}_z^2 k_x^2} \Psi(k_x, z = 0, f) e^{j2\pi \left(k_x x + z \left(\frac{f}{\hat{v}_z} \right) \sqrt{1 - \frac{\hat{v}_z^2 k_x^2}{f^2}} \right)} dk_x df. \quad (2.8)$$

2.1.2 Phase-shift migration for PW imaging

Gazdag's method for phase shift migration as described in section 2.1.1 cannot be directly applied to PW imaging. The PW phase-shift migration (PWPSM) method, as proposed in [30], is described below.

In case of PW emission angle $\theta = 0$, the ERM upward velocity \hat{v}_z is replaced by the original two-way depth-dependent propagation velocity c_z in (2.8) and then (to compensate for resultant overmigration of the reflector locations along the z -axis) $\Psi(k_x, z + \Delta z, f)$ in (2.5) is multiplied by $e^{\frac{j2\pi \Delta z f}{c_z}}$. This causes the explosion time of any reflector located at depth $z + \Delta z$ to be delayed by $\frac{\Delta z}{c_z}$. We can write the modified version as

$$\Psi(k_x, z + \Delta z, f) = \Psi(k_x, z, f) e^{j2\pi \hat{k}_z \Delta z}, \quad (2.9)$$

where

$$\hat{k}_z = \frac{f}{c_z} + k_z = \left(\frac{f}{c_z} \right) \left[1 + \sqrt{1 - \frac{c_z^2 k_x^2}{f^2}} \right]. \quad (2.10)$$

Consequently, (2.7) becomes

$$P(x, z + \Delta z, t = 0) = \iint_{f^2 > \hat{v}_z^2 k_x^2} \Psi(k_x, z = 0, f) e^{j2\pi(k_x x + \hat{k}_z z)} dk_x df. \quad (2.11)$$

In case of PW emission angle $\theta \neq 0$, we need to perform an appropriate transformation $z + \Delta z \rightarrow \hat{z} + \Delta \hat{z}$ associated with a propagation medium layer extending from z to Δz where a refracted plane wave travels with a velocity c_z at an angle θ_z . This is illustrated in Figure 2.2.

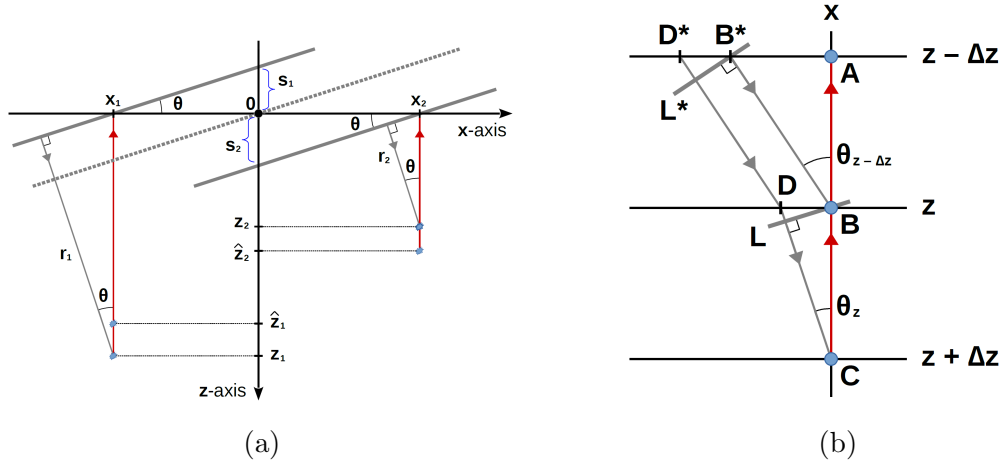


Figure 2.2: Depth and travel-time corrections for PW emission $\theta \neq 0$. (a) Exploding reflector depth corrections for constant velocity PW migration, (b) Travel-time considerations for depth-dependent velocity PW migration [25, 30].

Figure 2.2(a) shows the depth corrections applied to constant-velocity PW migration. Here, if the PW emission angle $\theta \neq 0$, the apparent reflector locations (x_1, z_1) and (x_2, z_2) must be corrected to (x_1, \hat{z}_1) and (x_2, \hat{z}_2) . This is done using the following time travel relationships:

$$\frac{2\hat{z}_1}{c} = \frac{r_1}{c} + \frac{z_1 - |s_1|}{c}, \quad \frac{2\hat{z}_2}{c} = \frac{r_2}{c} + \frac{z_2 + s_2}{c}, \quad (2.12)$$

where $r_1 = z_1 \cos(\theta)$, $r_2 = z_2 \cos(\theta)$, $s_1 = x_1 \tan(\theta)$, $s_2 = x_2 \tan(\theta)$. The z -axis shifts $|s_1|$ and s_2 account for travel distance differences between actual plane-wave emission (centered at $x = 0$) and the zero-offset wavefronts associated with the transmitter locations $(x_1, 0)$ and $(x_2, 0)$, respectively. For $\theta > 0$, z_1 is corrected upwards to \hat{z}_1 (negative x_2) while z_2 is corrected downwards to \hat{z}_2 (positive x_1). For $\theta < 0$, the

correction directions are reversed [25, 30]. Thus, we have

$$\hat{z}_1 = z_1 \left[\frac{1 + \cos(\theta)}{2} \right] + |x_1| \left[\frac{\tan(\theta)}{2} \right], \quad \hat{z}_2 = z_2 \left[\frac{1 + \cos(\theta)}{2} \right] + x_2 \left[\frac{\tan(\theta)}{2} \right]. \quad (2.13)$$

In general, we can write (2.13) as

$$\hat{z} = z^* + x \left[\frac{\tan(\theta)}{2} \right], \quad z^* = z \left[\frac{1 + \cos(\theta)}{2} \right]. \quad (2.14)$$

As for the transformation $z + \Delta z \rightarrow \hat{z} + \Delta \hat{z}$ in the case of depth-dependent velocity PW migration following is done (see Figure 2.2(b)). The two-way time travel $2\Delta \hat{z}/c_z$ along zero-offset segment BC is equated to the travel time $(DC + CB)/z$ along path DCB , including an arrival time correction $-\Delta t_z$ for nonzero-offset position D . The latter is reached from point D^* through the previous layer extending from $z - \Delta z$ to Δz where a refracted plane travels at an angle $\theta_{z-\Delta z}$ with velocity $c_{z-\Delta z}$. Therefore,

$$\frac{2\Delta \hat{z}}{c_z} = \frac{\Delta z}{c_z} \left[1 + \frac{1}{\cos(\theta_z)} \right] - \Delta t_z. \quad (2.15)$$

The zero-offset position B can be reached from the wavefront line L^* , as shown in Figure 2.2(b). The nonzero-offset position D is accounted for by subtracting travel time Δt_z from D^* to L^* . Given that

$$\Delta t_z = D^* B^* = p \Delta z |\tan(\theta_z)|, \quad (2.16)$$

we obtain

$$\Delta \hat{z} = \frac{\Delta z}{2} \left[1 + \frac{1}{\cos(\theta_z)} - pc_z |\tan(\theta_z)| \right], \quad (2.17)$$

where $p = |\sin(\theta_{z-\Delta z})|/c_{z-\Delta z} = |\sin(\theta_z)|/c_z = \dots = |\sin(\theta)|/c$ is the ray parameter p , which is same for all the layers (Snell's law). Here θ and c are the angle and velocity of PW emitted at the surface. Therefore,

$$\Delta \hat{z} = \frac{\Delta z}{2} \left[1 + \sqrt{1 - (c_z/c)^2 \sin^2(\theta)} \right] = \Delta z \left[\frac{1 + \cos(\theta_z)}{2} \right]. \quad (2.18)$$

Note that (2.18) can be also derived from time travel relationship $2\Delta \hat{z}/c_z = (LC + CB)/c_z$ along path LCB , where L denotes the zero-offset wavefront line as shown in Figure 2.2(b). Using $\Delta \hat{z}$ instead of Δz effectively results in a transformation $z + \Delta z \rightarrow z^* + \Delta \hat{z}$, where z^* is obtained layer by layer using $\Delta z^* = \Delta \hat{z} = \Delta z(1 + \cos(\theta_z))/2$

from (2.14). Hence for PW emissions with $\theta \neq 0$ we have

$$P_\theta(x, z^* + \Delta\hat{z}, t = 0) = \iint_{f^2 > c_z^2 k_x^2} \Psi_\theta(k_x, z^* + \Delta\hat{z}, f) e^{j2\pi k_x x} dk_x df, \quad (2.19)$$

where

$$\Psi_\theta(k_x, z^* + \Delta\hat{z}, f) = \Psi_\theta(k_x, z^*, f) e^{j2\pi \hat{k}_z \Delta\hat{z}}, \quad (2.20)$$

with initial $\Psi_\theta(k_x, z^*, f) = \Psi_\theta(k_x, 0, f)$ at $z^* = 0$. The remaining difference between $z^* + \Delta\hat{z}$ and $\hat{z} + \Delta\hat{z}$ is the term $x \tan(\theta_z)/2$ (from 2.14) which accounts for positional differences between the actual PW emission (centered at $x = 0$) and the assumed zero-offset wavefront (crossing a given $x \neq 0$). Once we have computed $P_\theta(x, z^*, t = 0)$ for all z^* values of interest, final $P_\theta(x, \hat{z}, t = 0) = P_\theta(x, z^* + x \tan(\theta_z)/2, t = 0)$ can be obtained for each layer by interpolating along the z^* -axis, where $\tan(\theta_z) = 1/\sqrt{1/\sin^2(\theta_z) - 1}$ and $\sin(\theta_z) = (c_z/c) \sin(\theta)$. The above method can be applied to a multilayered media with L layers, as shown in Figure 2.3.

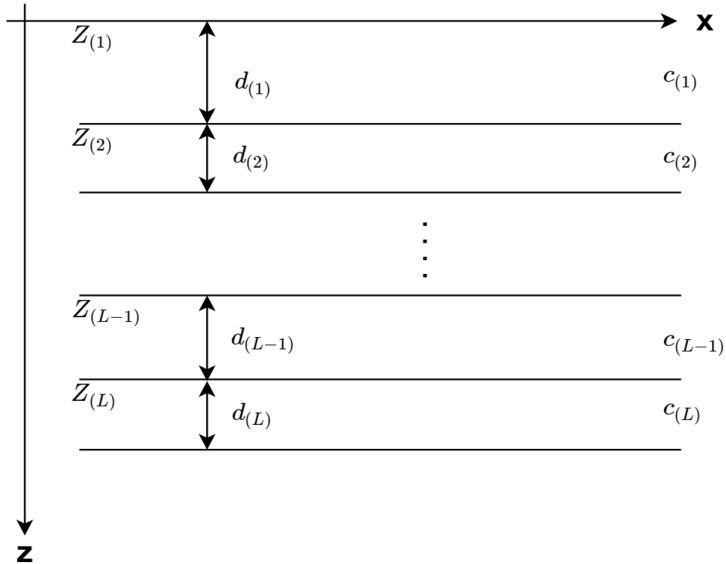


Figure 2.3: Multilayered propagation medium.

Let the layers be indexed by $l = 1, 2, \dots, L$ and let $d_{(l)}$ and $c_{(l)}$ denote the thickness and sound speed of layer l respectively. The top of the uppermost layer is denoted by $Z_{(1)} = 0$ and the interface between successive layers is denoted by $Z_{(l)}$. In general, the top of any layer l is given by $Z_{(l)} = Z_{(1)} + \sum_{i=1}^{l-1} d_{(i)}$, $l = 2, 3, \dots, L$. For such a layered propagation medium, the PWPSM method involves the following steps, applied to

each layer l .

Step 1: *Compute the wavefield at the top of the layer interface.*

- If $l = 1$ (top of the uppermost layer interface), compute $\Psi_\theta(k_x, 0, f)$ by applying the two dimensional Fourier transform to the recorded data $P_\theta(x, z = 0, t)$. Set $z^* \leftarrow 0$ and $\Psi_\theta(k_x, z^*, f) \leftarrow \Psi_\theta(k_x, 0, f)$.
- If $l \neq 1$, compute $\Psi_\theta(k_x, Z_{(l)}, f)$ by updating the spectrum at the top of the previous layer $\Psi_\theta(k_x, Z_{(l-1)}, f)$. This is done by first determining \hat{k}_z according to (2.10) and then multiplying $\Psi_\theta(k_x, Z_{(l-1)}, f)$ by extrapolation operator $e^{j2\pi\hat{k}_z d_{(l-1)}}$. Update $z^* \leftarrow Z_{(l)}$ and $\Psi_\theta(k_x, z^*, f) \leftarrow \Psi_\theta(k_x, Z_{(l)}, f)$.

Once, the spectrum at top of the interface is calculated, set $\Psi_\theta(k_x, z^*, f) \leftarrow 0$ whenever $f^2 > c_z^2 k_x^2$. This is to exclude the evanescent wavefield region.

Step 2: *Obtain a migrated image of the current layer.*

1. Determine $\Delta\hat{z}$ using (2.18) and compute $\Psi_\theta(k_x, z^* + \Delta\hat{z}, f)$ using (2.20).
2. Sum $\Psi_\theta(k_x, z^* + \Delta\hat{z}, f)$ obtained for each shift $\Delta\hat{z}$ along the f -axis, and then apply the inverse Fourier transform to the resultant sum along the k_x -axis to produce an image line $P_\theta(x, z^* + \Delta\hat{z}, t = 0)$. If the desired depth $Z_{(l+1)}$ is not reached, set $z^* \leftarrow z^* + \Delta\hat{z}$ and repeat until $z^* = Z_{(l+1)}$.

Step 3: *Perform angle correction.*

For each layer l , obtain final $P_\theta(x, \hat{z}, t = 0)$ from $P_\theta(x, z^*, t = 0)$ via interpolation along the z^* -axis, according to the formula $\hat{z} = z^* + x \tan(\theta_z)/2$.

2.1.3 Phase-shift migration for SA imaging

The PSM method for SA imaging involves the following steps for each layer l . These steps arise directly from the original method proposed by Gazdag [28].

Step 1: *Compute the wavefield at the top of the layer interface.*

- If $l = 1$ (top of the uppermost layer interface), compute $\Psi(k_x, 0, f)$ by applying two dimensional Fourier transform to the recorded data $P(x, z = 0, t)$. Set $z^* \leftarrow 0$ and $\Psi(k_x, z^*, f) \leftarrow \Psi(k_x, 0, f)$.

- If $l \neq 1$, compute $\Psi(k_x, Z_{(l)}, f)$ by updating the spectrum at the top of the previous layer $\Psi(k_x, Z_{(l-1)}, f)$. This is done by first determining k_z according to (2.6) and then multiplying $\Psi(k_x, Z_{(l-1)}, f)$ by extrapolation operator $e^{j2\pi k_z d_{(l-1)}}$. Update $z^* \leftarrow Z_{(l)}$ and $\Psi(k_x, z^*, f) \leftarrow \Psi(k_x, Z_{(l)}, f)$.

Once, the spectrum at top of the interface is calculated, set $\Psi_\theta(k_x, z^*, f) \leftarrow 0$ whenever $f^2 > c_z^2 k_x^2$. This is to exclude the evanescent wavefield region.

Step 2: *Obtain a migrated image of the current layer.*

1. Compute $\Psi(k_x, z^* + \Delta z, f)$ using (2.5).
2. Sum $\Psi(k_x, z^* + \Delta z, f)$ obtained for each shift Δz along the f -axis, and then apply the inverse Fourier transform to the resultant sum along the k_x -axis to produce an image line $P(x, z^* + \Delta z, t = 0)$. If the desired depth $Z_{(l+1)}$ is not reached, set $z^* \leftarrow z^* + \Delta z$ and repeat until $z^* = Z_{(l+1)}$.

2.2 Outstanding Issues

The PSM methods described in the previous section are sensitive to layer boundary and sound speed mismatches [25], which can result in a variety of artifacts leading to poor image reconstruction quality [31]. In an inhomogeneous media, the speed of sound varies across different layers. Incorrect SOS assumptions may lead to broader ultrasound beams, inaccuracies in calculations, poor contrast, and degraded resolution as a result of increased acoustic clutter [32–35]. Chen and Zagzebski [36] reported from their simulations that an incorrect sound speed assumption can not only cause misregistration of point targets, but also cause dynamic receive focus to miss the target.

Albulayli [25] investigated the sensitivity of the PWPSM method to layer boundary and sound speed mismatches. A simulation involving a three-layer medium (tissue–bone–tissue) was used. The ball-shaped targets were present in the third layer. The bone and tissue layers had the sound speed of 3198 and 1540 m/s, respectively with the bone layer spanning the depth range from 5 to 12 mm.

When migration was carried out with using the sound speed in the bone layer 20% greater than its true value, the image was overmigrated, i.e., the targets took convex shape and were misplaced downwards. When migration was carried out using the sound speed in the bone layer 20% lower than its true value, the image was undermigrated, i.e., the targets took concave shape and were misplaced upwards.

In the case of mismatched layer boundaries, when migration was carried out using the bone layer thickness 29% greater than its true value, the image was overmigrated with some artifacts appearing in the layer boundaries. The overmigration was a result of the extrapolation process extending over the true thickness of the bone layer and entering into the following low-velocity tissue layer. When migration was carried out using the bone layer thickness 29% lower than its true value, the image was undermigrated, and the layer boundaries were misplaced. The targets were less focused due to the completion of the extrapolation process before the end of the bone layer was reached.

The above discussion illustrates why accurate SOS profiling is an important aspect of the migration-based image reconstruction process. In this thesis, the SOS profiling problem essentially means estimating the sound speed and thickness values of each layer in a stratified medium, followed by PSM using the estimated values in question.

2.3 Related Work

PSM requires the SOS profile (i.e., depth-dependent values of the sound speed) as an input, to relate time t of a recorded reflection event to its distance z from the surface. Since in practice we do not know the exact values of each layer's thickness and sound speed, we rely on using their estimated values during migration [26]. Over the years, several techniques have been proposed and developed to estimate the speed of sound in ultrasound imaging.

Robinson *et al.* [37] classified speed estimation methods into transmission-based and reflection-based. Transmission-based methods measure the time of flight and include pulse transit time measurements, the 'sing-around' technique, the penetrating hydrophone, and velocity difference methods. The transmission methods mentioned in [38–40] are based on reference pulses generated by reflected surfaces behind the sample under inspection. These methods rely on a wide-angle acoustic access and are affected by strong refracting structures, which restrict them from being used for diagnostic purposes. On the other hand, reflection-based methods estimate sound speeds using pulse-echo data obtained from one or several ultrasound transducers. They include image aberration based methods, intersecting beam transit-time methods, and axial techniques. However, most of them require multiple ultrasound apertures, which increases system complexity and limits their applicability.

Several methods calculated the wave speed estimates using the sound speed in

a fluid containing scatterers, without prior knowledge of the propagation distance [41–44]. In these methods, speed estimates were calculated after measuring the time delay between the scattered signals and the receiver transducer positioned at different locations. Kondo *et al.* [41] implemented a crossed-beam method that involved finding local sound speed estimates using the propagation time differences between two or more crossed transmit and receive beams achieving the precision of 3% – 4% in homogenous and in-vivo media. Hachiya *et al.* [45] determined sound speeds via frequency-domain calculations of travel time through the tissue and the travel time difference due to the presence of inhomogeneities inside the medium. Anderson and Trahey [43] provided a best-fit technique similar to the one used in seismology for the sound speed estimation with a single scan of pulse-echo ultrasound transducer using geometric delay patterns of echoes returning to an array of transducer elements from a target or a region of interest with an estimation accuracy up to 0.1%. However, the performance of this estimation method depended on several factors, including signal-to-noise ratio, transducer array geometry, transducer positioning precision, and phase errors due to medium inhomogeneities. A similar method by Pereira *et al.* [44] estimated sound speeds by measuring cross-correlation of the time-delay profile, along the beam axis, between the scattered signals recorded at two locations. Here, the minimization of the RMS error between theoretical and experimental time-delay profiles was used to obtain the speed estimates. However, this technique was tested with homogeneous media where the speed of sound was assumed to be constant. Hatakeyama *et al.* [46] presented an in-vivo velocity estimation method using a focused ultrasonic pulse wave focused at a point on the inner surface of a skull bone by assigning an appropriate time delay to each of the transducers. The reflected pulses detected by the said transducers were summed, and their time delays were optimized to get the maximum envelope amplitude of the signal. More recently, Byram *et al.* [47] proposed to calculate the time of flight between two spatially registered points in order to estimate local sound speed values. Jakovljevic *et al.* [48] described a similar approach, where local speed estimates were obtained by first calculating the average speed of sound using the technique from [43] and then optimizing it using the gradient descent algorithm. This method performs well in noisy homogenous media producing less visible artifacts; however, it faces several limitations in inhomogeneous media due to wave propagation complexities. Sanabria *et al.* [49] estimated local sound speeds using ultrasound computed tomography (USCT) technique by optimizing transmit-receive echo data to obtain a robust time of flight measurement of ultrasound wavefronts.

Reflection-based image aberration methods mentioned in [37, 50–52] used two transducers to compare spatial shifts of two ultrasound images to estimate sound speeds in a homogeneous medium. Similarly, Krucker *et al.* [53] estimated the average sound speed based on automatic registration of overlapping nonzero-angle images over a zero-angle image using ray acoustics. They used one-dimensional optimization to vary the speed and map the nonzero-angle data onto the zero-angle data until maximum correlation was achieved. Qu *et al.* [54] proposed a method using speckle analysis to estimate average sound speed. The method involved using the same pre-beamformed data but different assumed speeds. The desired sound speed was obtained by identifying an image with the best focus quality.

Some of the speed estimation methods used deconvolution for solving the inverse-scattering problem applied to backscattered ultrasound signals [55, 56]. Shin *et al.* [57, 58] estimated velocities in homogeneous and inhomogeneous media using different point spread functions to perform deconvolution on a known layer boundary position of the images simulated using different sound speeds. However, the random nature of the biological tissues and attenuation of the incident pulse may limit the applicability of these methods in practice [59].

Several region-of-interest(ROI)-based mean sound speed estimation methods have also been proposed in recent years [34, 60, 61]. Here, optimal mean sound speed is the one that can produce the best focusing performance in the ROI rather than the actual sound speed in ROI-specific tissue type. Cho *et al.* [60] showed high-quality B-mode images of porcine tissues with fat using a fast sound speed estimation method by adjusting echo signals on a few scan lines. In this case, an optimal sound speed was found by identifying the speed that provides the best match between the theoretical delays and echo signal delays at the transducer. Napolitano *et al.* [34] used lateral frequency analysis on a B-mode image to find an optimal sound speed. Here, the echo signal energies in a known spatial frequency band were maximized during receive beamforming. This method requires all the channel data over the entire imaging region. De Sousa *et al.* [62] used the distance between transducers elements and delay between echoes from interfaces between different layers to measure the sound speeds and thicknesses in multi-layered media. They reported estimated sound speed errors ranging from 1.8 to 6.6%. Park *et al.* [63] and Lee *et al.* [64] presented computationally efficient methods to estimate the mean sound speed as well as enhance spatial and contrast resolution. Here, the focusing quality was measured by computing the minimum average sum of the absolute difference (MASAD) of raw

radio-frequency (RF) data during receive beamforming in the ROI. The mean sound speed value was then determined by the inexpensive average sum of absolute difference of each pre-beamformed RF data.

In this thesis, we present a two-stage layer-by-layer SOS profiling approach targeting CPWC imaging of stratified media. For each layer, the first stage produces a sound speed estimate, and the second stage produces a thickness estimate (using the estimated speed of sound value). Our method uses only the multi-angle raw RF data to be migrated, i.e., it does not require additional transducers or measurements. Essentially, we apply PSM to two (zero-angle and nonzero-angle) data frames with an iterative sweep of possible velocity values and pick the one that yields the closest similarity between the resulting migrated frames. This is done one layer at a time, starting from the surface. Once we find the sound speed for a given layer, we estimate the thickness of that layer using the zero-angle data. Finally, we use the estimated SOS profile to perform final PSM-based image reconstruction. This approach enables self-calibrated migration of multi-angle raw RF data during CWPC imaging of a stratified medium. Similar to the image aberration based approaches [37, 53, 54], our method aims at exploiting the geometrical distortions in the image to identify most suitable choices for speed and thickness values. The details of our method are provided in the next chapter.

Chapter 3

SOS Profiling for CPWC Imaging

In the previous chapter, we discussed PSM and its application to PW and SA imaging. We also discussed how layer boundary and sound speed mismatches could affect image reconstruction. This chapter explains our proposed method for SOS profiling, i.e., estimating the sound speed and thickness for individual layers prior to the PSM-based image reconstruction. In the later part of this chapter, we also show how one can reduce the computational cost of phase shift migration.

3.1 Problem formulation

Recalling Figure 2.3 in Chapter 2, let $\mathbf{c}_{(l)}$ represent a set of distinct sound speed values under consideration (for a given layer l), ranging from $c_{(l)}^{\min}$ to $c_{(l)}^{\max}$ with an incremental step size of $\Delta c_{(l)}$, i.e., we have $\mathbf{c}_{(l)} = \{c_{(l)}^{\min}, c_{(l)}^{\min} + \Delta c_{(l)}, c_{(l)}^{\min} + 2\Delta c_{(l)}, \dots, c_{(l)}^{\max}\}$. Similarly, let $\mathbf{d}_{(l)}$ represent a set of distinct thickness values under consideration (for a given layer l), ranging from $d_{(l)}^{\min}$ to $d_{(l)}^{\max}$ with an incremental step size of $\Delta d_{(l)}$, i.e., we have $\mathbf{d}_{(l)} = \{d_{(l)}^{\min}, d_{(l)}^{\min} + \Delta d_{(l)}, d_{(l)}^{\min} + 2\Delta d_{(l)}, \dots, d_{(l)}^{\max}\}$. Let $\boldsymbol{\theta} = \{\theta_w, w = 1, 2, \dots, W\}$ be a set of W plane wave angles used during CPWC imaging of our horizontally-layered medium. For SOS profiling, we need two angles, $\{\theta_a, \theta_b | \theta_a = 0^\circ, \theta_b \in \boldsymbol{\theta}, \theta_a \neq \theta_b\}$, i.e., we use the zero-angle frame (corresponding to θ_a) and one of nonzero-angle frames (corresponding to θ_b). Our objective is to find estimates $c_{(l)}^*$ and $d_{(l)}^*$ of the sound speed and thickness of each layer l . We accomplish this in two steps: first, we find $c_{(l)}^*$, and then we find $d_{(l)}^*$ based on $c_{(l)}^*$.

Our formulation of the layer-by-layer sound speed estimation problem is stated below.

Inputs: $\Psi_{\theta_a}(k_x, Z_{(l)}, f)$, $\Psi_{\theta_b}(k_x, Z_{(l)}, f)$, $\mathbf{c}_{(l)}$, $d_{(l)}^{\max}$.

Output: $c_{(l)}^* \in \mathbf{c}_{(l)}$.

$$\textbf{Objective: } \text{Max } \rho(\mathbf{s}_{\theta_a}(c_{(l)}^*), \mathbf{s}_{\theta_b}(c_{(l)}^*)) = \frac{\mathbf{s}_{\theta_a}(c_{(l)}^*) \cdot \mathbf{s}_{\theta_b}(c_{(l)}^*)}{\|\mathbf{s}_{\theta_a}(c_{(l)}^*)\|_2 \cdot \|\mathbf{s}_{\theta_b}(c_{(l)}^*)\|_2}.$$

Here, $\rho(\mathbf{s}_{\theta_a}(c_{(l)}^*), \mathbf{s}_{\theta_b}(c_{(l)}^*))$ represents the *cosine similarity*¹ between two vectors $\mathbf{s}_{\theta_a}(c_{(l)}^*)$ and $\mathbf{s}_{\theta_b}(c_{(l)}^*)$. These data vectors $\{\mathbf{s}_{\theta_k}, k \in \{a, b\}\}$ are obtained from 2D migrated layer images $P_{\theta_k}(x, \hat{z}, t = 0)$ by performing a certain vectorization operation, denoted by $\mathbf{V}\{\cdot\}$ in the sequel. Data matrices $P_{\theta_k}(x, \hat{z}, t = 0)$ are a result of PSM applied to $\Psi_{\theta_k}(k_x, Z_{(l)}, f)$ (see section 2.1.2), assuming the speed of sound $c_{(l)}^*$ for the layer l in question, with \hat{z} ranging from $Z_{(l)}$ to $Z_{(l)} + d_{(l)}^{\max}$.

For thickness estimation, our objective is to apply a certain boundary detection operation $\mathbf{B}\{\cdot\}$ on a zero-angle migrated layer image $P_{\theta_a}(x, \hat{z}, t = 0)$ (obtained using sound speed estimate $c_{(l)}^*$) in the range $Z_{(l)} + d_{(l)}^{\min}$ to $Z_{(l)} + d_{(l)}^{\max}$. The purpose of $\mathbf{B}\{\cdot\}$ is to detect a horizontal end-of-layer boundary that results in our thickness estimate $d_{(l)}^*$.

3.2 Our approach

Figure 3.1 shows our approach for the SOS profiling problem. We begin with wavefields $P_{\theta_a}(x, z = 0, t)$ and $P_{\theta_b}(x, z = 0, t)$ recorded for angles θ_a and θ_b at the surface (i.e., the top interface $Z_{(1)} = 0$ of the first layer). These recorded wavefields are Fourier transformed along the x -axis and t -axis to get their initial spectra $\Psi_{\theta_a}(k_x, 0, f)$ and $\Psi_{\theta_b}(k_x, 0, f)$. Then, we proceed downward layer-by-layer into the medium, updating $\Psi_{\theta_a}(k_x, Z_{(l)}, f)$ and $\Psi_{\theta_b}(k_x, Z_{(l)}, f)$ for each layer l , which are used as an input for obtaining our sound speed and thickness estimates for that layer.

3.2.1 Sound speed estimation

For sound speed estimation, we perform the following steps for each distinct sound speed value $c_{(l)}^i$ in $\mathbf{c}_{(l)}$:

¹The cosine similarity value ranges from -1 (two vectors have the opposite orientations) to $+1$ (two vectors have the same orientation).

1. Apply PSM to $\Psi_{\theta_a}(k_x, Z_{(l)}, f)$ and $\Psi_{\theta_b}(k_x, Z_{(l)}, f)$ to extrapolate from $Z_{(l)}$ to $Z_{(l)} + d_{(l)}^{\max}$, which yields 2D migrated layer images $P_{\theta_a}(x, \hat{z}, t)$ and $P_{\theta_b}(x, \hat{z}, t)$ at explosion time $t = 0$. This step is depicted in Figure 3.2.
2. Apply a vectorization operation $\mathbf{V}\{\cdot\}$ to convert 2D migrated layer images $P_{\theta_a}(x, \hat{z}, t = 0)$ and $P_{\theta_b}(x, \hat{z}, t = 0)$ to vectors $\mathbf{s}_{\theta_a}(c_{(l)}^i)$ and $\mathbf{s}_{\theta_b}(c_{(l)}^i)$. We use two ways to vectorize the migrated data.
 - (a) Summing: The 2D migrated layer image in (z, x) domain is summed across the x -axis to form a z -axis vector.
 - (b) Stacking: The 2D migrated layer image in (z, x) domain is flattened to a vector by concatenating its columns.
3. Compute cosine similarity $\rho(\mathbf{s}_{\theta_a}(c_{(l)}^i), \mathbf{s}_{\theta_b}(c_{(l)}^i))$ to measure the similarity in the orientation of two vectors $\mathbf{s}_{\theta_a}(c_{(l)}^i)$ and $\mathbf{s}_{\theta_b}(c_{(l)}^i)$.

The above operations are performed for each sound speed value $c_{(l)}^i$ in $\mathbf{c}_{(l)}$, which yields a vector of cosine similarities $\mathbf{r}_{(l)}$ as shown below.

$$\mathbf{r}_{(l)} = \begin{bmatrix} \rho_{c_{(l)}^{\min}} \\ \vdots \\ \rho_i \\ \vdots \\ \rho_{c_{(l)}^{\max}} \end{bmatrix}, \quad (3.1)$$

where $\rho_i = \rho(\mathbf{s}_{\theta_a}(c_{(l)}^i), \mathbf{s}_{\theta_b}(c_{(l)}^i))$. The index corresponding to the maximum value of $\mathbf{r}_{(l)}$ can be found as:

$$i^* = \arg \max_i \mathbf{r}_{(l)}. \quad (3.2)$$

This index i^* is used to locate our estimate of sound speed $c_{(l)}^*$ for layer l within vector $\mathbf{c}_{(l)}$.

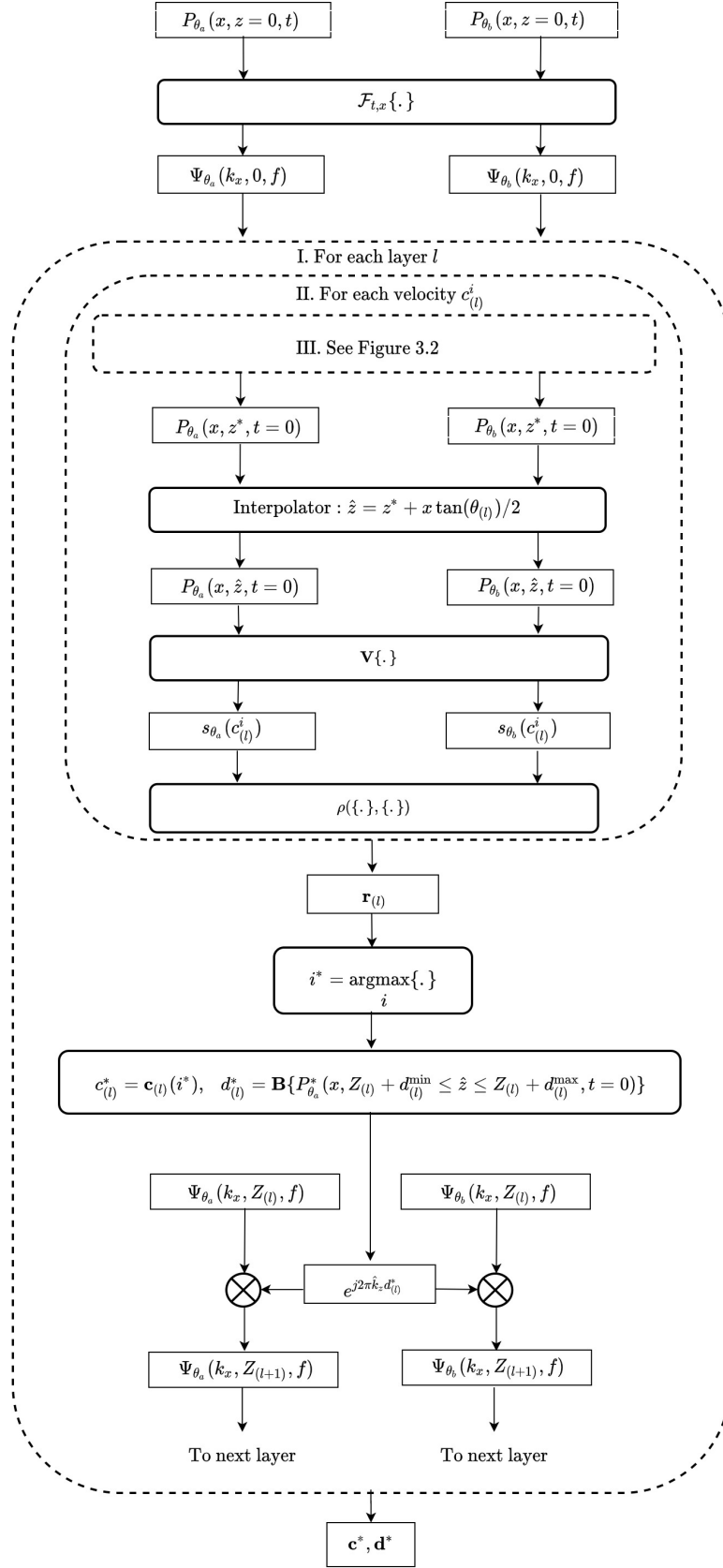


Figure 3.1: Proposed method for SOS profiling.

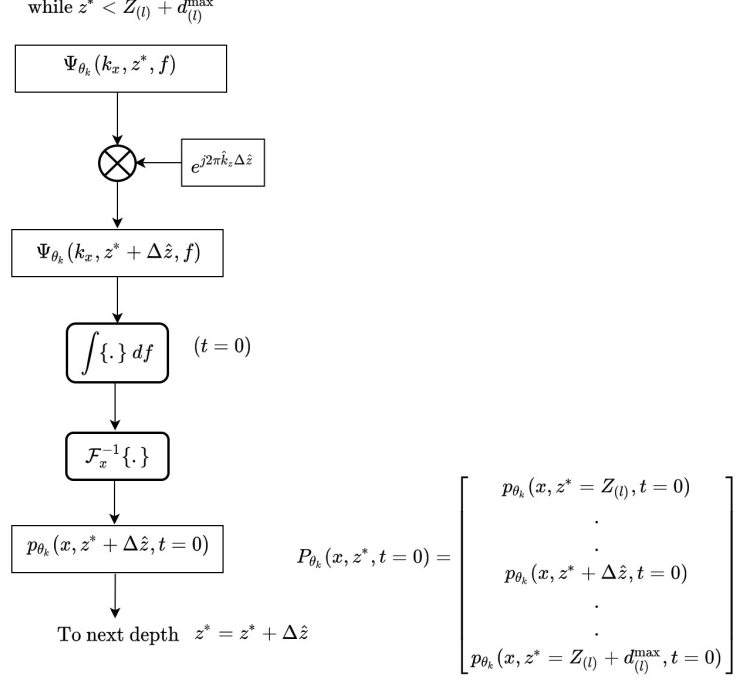


Figure 3.2: Downward extrapolation during SOS profiling.

3.2.2 Layer thickness estimation

To find layer thickness estimate $d_{(l)}^*$ of layer l , we use boundary detection based on our sound speed estimate $c_{(l)}^*$. We consider two ways for end-of-layer boundary detection: line detection and peak detection.

In order to estimate layer thickness using line detection, we restrict zero-angle 2D migrated layer image $P_{\theta_a}^*(x, \hat{z}, t = 0)$, obtained assuming sound speed estimate $c_{(l)}^*$, to the depth range $[Z_{(l)} + d_{(l)}^{\min}, Z_{(l)} + d_{(l)}^{\max}]$. The resulting image section is max-normalized, smoothed using a moving-average filter, and then subjected to Otsu's binary thresholding for segmentation. Following binary thresholding, we perform morphological image processing ² to remove horizontal discontinuities in the segmented lines and strip away pixel layers to reduce their widths. This is done to avoid the presence of multiple lines in the same neighborhood. Finally, we employ the Hough transform [65, 66] to detect a horizontal line stretching across the entire x -axis, which corresponds to the end-of-layer boundary. A brief explanation of the Hough transform is provided in Appendix B. The z -axis location corresponding to

²We use morphological erosion to remove islands and small objects and morphological thinning to remove foreground pixels from the segmented lines in the image.

the horizontal line detected by the Hough transform gives us the estimate of thickness $d_{(l)}^*$.

Line detection is computationally expensive but provides a robust approach to detect layer boundaries. An alternative computationally inexpensive method involves using peak detection to estimate layer thickness. In order to estimate layer thickness using peak detection, we first sum zero-angle 2D migrated layer image $P_{\theta_a}^*(x, \hat{z}, t = 0)$ along the x -axis to get vector $s_{\theta_a}(\hat{z})$, where \hat{z} is restricted to the depth range $[Z_{(l)} + d_{(l)}^{\min}, Z_{(l)} + d_{(l)}^{\max}]$. Then our thickness estimate $d_{(l)}^*$ is given by the position of peak value in this vector, i.e.,

$$d_{(l)}^* = z_{peak} = \arg \max_t s_{\theta_a}(d_{(l)}^{\min} : d_{(l)}^{\max}) . \quad (3.3)$$

Instead of $P_{\theta_a}^*(x, Z_{(l)} + d_{(l)}^{\min} \leq \hat{z} \leq Z_{(l)} + d_{(l)}^{\max}, t = 0)$, one can also use zero-angle raw RF data $P_{\theta_a}(x, z = 0, t)$ in (t, x) domain to estimate the layer thickness. For line detection, we restrict $P_{\theta_a}(x, z = 0, t)$ to the t -axis section $[T_{(l)} + t_{(l)}^{\min}, T_{(l)} + t_{(l)}^{\max}]$ (derived from $d_{(l)}^{\min}$ and $d_{(l)}^{\max}$), where $T_{(l)}$ denotes the t -axis location corresponding to depth $Z_{(l)}$. We have

$$t_{(l)}^{\min} = \left\lfloor \frac{2d_{(l)}^{\min}}{c_{(l)}^* f_s} \right\rfloor, \quad t_{(l)}^{\max} = \left\lceil \frac{2d_{(l)}^{\max}}{c_{(l)}^* f_s} \right\rceil , \quad (3.4)$$

where f_s represents the sampling frequency of the raw RF signals. Similar to the 2D migrated layer image, our raw RF image data undergoes max-normalization, filtering, binary thresholding, and morphological processing, which is then followed by the Hough transform to detect a horizontal line corresponding to the end-of-layer boundary. The t -axis location $t_{(l)}^*$ of the horizontal line detected by the Hough transform gives us the estimate of thickness $d_{(l)}^*$ using the following relation:

$$d_{(l)}^* = d_{(l)}^{\min} + \frac{c_{(l)}^*(t_{(l)}^* - t_{(l)}^{\min})}{2} . \quad (3.5)$$

For peak detection, we sum the zero-angle raw RF data $P_{\theta_a}(x, z = 0, t)$ along the x -axis to get $s_{\theta_a}(t)$, where t is restricted to the range $[T_{(l)} + t_{(l)}^{\min}, T_{(l)} + t_{(l)}^{\max}]$. We find the t -axis value $t_{(l)}^*$ corresponding to the presumed end-of-layer boundary as follows:

$$t_{(l)}^* = \arg \max_t s_{\theta_a}(t_{(l)}^{\min} : t_{(l)}^{\max}) . \quad (3.6)$$

The thickness estimate $d_{(l)}^*$ can now be obtained by using (3.5).

3.2.3 Layer post-processing

The estimated sound speed $c_{(l)}^*$ and thickness $d_{(l)}^*$ of layer l can now be used to determine the top of the interface of the next layer, $Z_{(l+1)} = Z_{(l)} + d_{(l)}^*$ and the wavefield at $Z_{(l+1)}$, $\Psi_{\theta_k}(k_x, Z_{(l+1)}, f)$. The latter can be obtained by multiplying the wavefield $\Psi_{\theta_k}(k_x, Z_{(l)}, f)$ by the extrapolation operator $e^{j2\pi\hat{k}_z d_{(l)}^*}$. After updating $z^* \leftarrow Z_{(l+1)}$ and $\Psi_{\theta_k}(k_x, z^*, f) \leftarrow \Psi_{\theta_k}(k_x, Z_{(l+1)}, f)$, we proceed to the next layer. Once we get estimated sound speed and thickness values for all the layers $\{\mathbf{c}^*, \mathbf{d}^*\}$, we apply the PWPSM method to reconstruct the entire CPWC image.

3.3 Computational cost reduction

During PWPSM, for each angle θ_k and within each layer l , the wavefield spectrum $\Psi_{\theta_k}(k_x, Z_{(l)}, f)$ is repeatedly multiplied with extrapolation operator $e^{j2\pi\hat{k}_z \Delta z}$. If Ψ_{θ_k} is of size $P \times Q$, then each depth extrapolation step Δz within layer l entails $P \times Q$ complex multiplications. This makes PWPSM computationally expensive. The computational cost becomes worse during SOS profiling, since we perform extrapolation over all possible sound speed values in $\mathbf{c}_{(l)}$. In the rest of this section, we describe a simple scheme for implementing low-cost plane wave phase-shift migration (LCPW-PSM) with reduced number of complex multiplications.

For the sake of simplicity, let us use Ψ_{θ_k} to represent the spectrum $\Psi_{\theta_k}(k_x, 0, f)$. It turns out that a large number of values in this spectrum have small magnitudes, i.e., they do not significantly contribute to the overall energy. Our cost reduction scheme essentially involves not applying phase shifts to such negligible-energy elements in the spectrum. The procedure specified below can be applied to phase-shift migration during SOS profiling as specified in Figure 3.2.

Let $[|\Psi_{p,q}|^2]_{\theta_k}$ denote a P -by- Q matrix of squared magnitudes of elements of Ψ_{θ_k} . Let $[\psi_r]_{S \times 1}$ denote a sorted vector of all $S = P \times Q$ elements of $[|\Psi_{p,q}|^2]_{\theta_k}$, arranged in decreasing order of their values. The cumulative sum vector $[\sigma_s]_{S \times 1}$ of the sorted vector $[\psi_r]_{S \times 1}$ is given as

$$\sigma_s = \sum_{r=1}^s \psi_r . \quad (3.7)$$

Therefore, the total energy E of the spectrum is equal to the last element of the

cumulative sum vector , i.e.,

$$E = \sigma_S = \sum_{p,q} |\Psi_{p,q}|^2 . \quad (3.8)$$

We define the energy threshold T_e based on the fraction of energy η that we want to retain in the spectrum,

$$T_e = \eta E . \quad (3.9)$$

Next, we find the first element in the cumulative sum vector $[\sigma_s]_{S \times 1}$, denoted by $\bar{\sigma}$, such that $\bar{\sigma} > T_e$. Essentially, the sorted subvector $[\sigma_1, \sigma_2, \dots, \bar{\sigma}]$ identifies the corresponding subset of the largest-squared-magnitude elements of Ψ_{θ_k} whose cumulative sum (i.e., their collective energy) meets our energy retention threshold T_e .

Effectively, we get a binary threshold matrix \mathbf{T} to accompany Ψ_{θ_k} ,

$$\mathbf{T}(p, q) = \begin{cases} 0, & \text{if } |\Psi_{p,q}|^2 < \sqrt{\bar{\sigma}} \\ 1, & \text{otherwise.} \end{cases} . \quad (3.10)$$

Whenever $\mathbf{T}(p, q) = 0$, the index pair (p, q) will locate the element in Ψ_{θ_k} for which we skip a complex multiplication by the corresponding element in the phase shift matrix $e^{j2\pi k_z \Delta z}$. It is important to note that our decision matrix \mathbf{T} needs to be determined only once for every PW angle θ_k , using only the Fourier-transformed surface data $\Psi_{\theta_k}(k_x, 0, t)$. In other words, \mathbf{T} does not change during PSM, since it is derived based solely on magnitudes (not affected by phase shifts).

3.4 Computational complexity

The computational complexity of an algorithm can be measured by studying the growth rate of the operations as a function of the input data size. Table 3.1 shows the computational complexity associated with main steps performed during PWPSM.

Let the raw data be of size $N_t \times N_x$, corresponding to N_t time samples and N_x transducer element positions. After the Fourier transform, the data size is $N_f \times N_{k_x}$ where N_f is proportional to N_t and N_{k_x} is proportional to N_x . The number of z -lines denoted by N_z is also proportional to N_t . Since our concern is the asymptotic complexity, we drop all the proportionality constants and set $N_x = N_{k_x}$ and $N_t = N_z = N_f$. The initial Fourier transform from (x, t) to (k_x, f) takes $O(N_x N_t \log(N_x N_t))$ time. It is subsequently followed by the extrapolation operation where the wavefield spectrum is mul-

tiplied by the phase-shift exponentials. This phase-shift multiplication is performed N_t times, once for every z -line, hence the complexity is $O(N_x N_t^2)$. The next step, which is summation over f followed by the 1D inverse Fourier transform along the k_x -axis, is also performed N_t times, which yields the complexity of $O(N_t N_x \log N_x)$. Hence, the overall complexity of our downward extrapolation operation is $O(N_x N_t^2)$. Next, linear interpolation to correct the migrated data for each layer contributes the complexity of $O(N_x N_t)$. The end-of-layer phase shifts, performed before moving to the next layer, take $O(N_x N_t L)$ time. For speed estimation, cosine similarity between two migrated data vectors is calculated for each of N_c velocity choices in a layer, which takes $O(N_x N_t N_c)$ time. During thickness estimation, our peak-based boundary detection has the complexity of $O(N_x N_t)$. Overall, the computational complexity (per PW angle) can be expressed as $O(N_x N_t^2 N_c)$, dominated by the SOS profiling step that performs PSM N_c times, with each migration taking extrapolation-dominated $O(N_x N_t^2)$ time.

Operation	Complexity
2D Fourier transform	$O(N_x N_t \log(N_x N_t))$
Phase shifting	$O(N_x N_t^2)$
1D inverse Fourier transform	$O(N_x N_t \log(N_x))$
Linear interpolation	$O(N_x N_t)$
End-of-layer phase shift	$O(N_x N_t L)$
Cosine similarity	$O(N_x N_t N_c)$
Peak-based boundary detection	$O(N_x N_t)$

Table 3.1: Computational complexity of SOS profiling in PWPSM.

The number of operations described above can be significantly reduced if we use LCPWPSM described in section 3.3. Let N_1 denote the number of 1's in our decision matrix \mathbf{T} . Then, instead of $O(N_x N_t)$ complex multiplications, we need to perform only $O(N_1)$ of them. Therefore, the complexity of the extrapolation step becomes $O(N_1 N_t)$, and the complexity of the end-of-layer phase shifts becomes $O(N_1 L)$.

Chapter 4

Evaluation Results

This chapter provides our evaluation results for SOS profiling. The crux of this evaluation involves using K-WAVE simulated dataset of CPWC imaging of a three-layer medium, mimicking tissue-bone-tissue ultrasound propagation. As supplementary evaluation cases, we also estimate: 1) layer thickness values using an experimental SA imaging dataset obtained by 2-D synthetic-aperture focusing of a water-glass-metal medium, and 2) the sound speed value in a single-layer medium using longitudinal and cross-sectional carotid artery data provided by PICMUS.

4.1 Evaluation results for SOS profiling in CPWC imaging

4.1.1 Experimental setup

Similar to the setup in [25, 30], we use K-WAVE MATLAB toolbox [67] to simulate the following data acquisition. A 128-element linear transducer with 0.308-mm pitch emits a 2-MHz plane-wave Gaussian pulse ($\lambda = 0.770$ mm, 4.5 cycles). Plots of the resulting input signal and its amplitude spectrum are shown in Figure 4.1. This pulse propagates through a three-layer medium towards ball-shaped “point” targets (0.616-mm diameter) located at the (x, z) co-ordinates listed in Table 4.1. A schematic of our simulation layout [68] in Figure 4.2 shows these imaging targets and the transducer on a three-dimensional grid. The propagation medium properties [69] shown in Table 4.2 mimic an approximate tissue-bone-tissue layer arrangement. The simulation is carried out using nine PW emissions ($\theta = 0^\circ, \pm 4^\circ, \pm 8^\circ, \pm 12^\circ, \pm 16^\circ$) to enable coherent

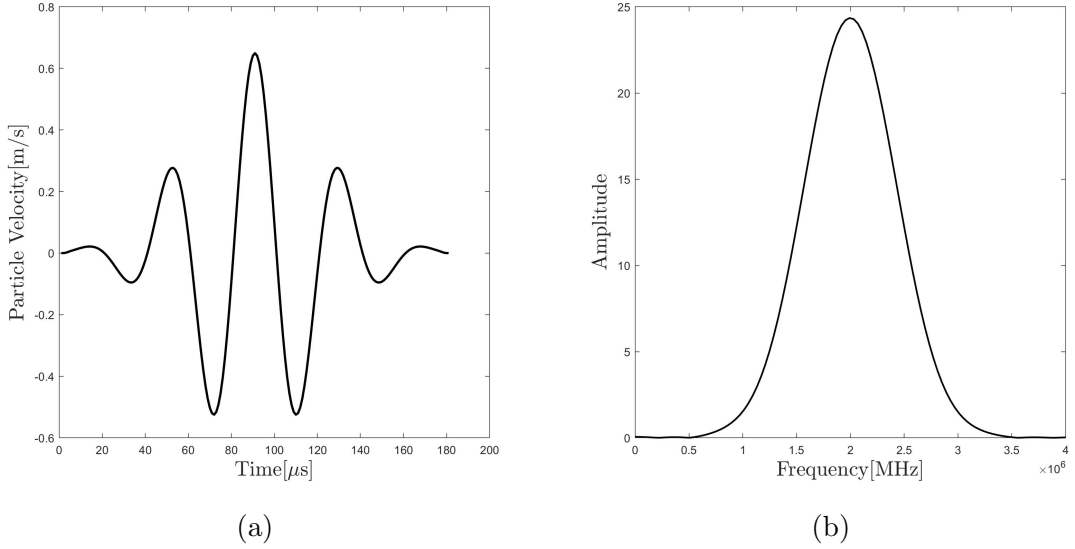


Figure 4.1: Emitted PW pulse. (a) Time domain, (b) Frequency domain.

Upper targets	(-13,22)	(0,22)	(13,22)
Middle targets	(-13,35)	(0,35)	(13,35)
Lower targets	(-13,48)	(0,48)	(13,48)

Table 4.1: Location (x, z) of point targets (in mm) inside the three-layer medium.

compounding.

Medium Layer	Speed, $c_z, \text{m/s}$	Density, kg/m^2	Abs.Coeff., dB/cm-MHz	Depth Span, mm
I	1540	1000	0.75	$0 \leq z < 5$
II	3198	1990	3.54	$5 \leq z < 12$
III	1540	1000	0.75	$12 \leq z < 63$

Table 4.2: Propagation medium specifications.

During simulations, we set spatial grid spacing to $\lambda/5 = 0.154$ mm and the temporal sampling frequency to 80 MHz. The simulations result in raw RF data of size 128×6592 for each angle in (x, t) domain. The flow chart in Figure 4.3 shows the processing steps during image formation. To account for the loss in signal energy during the propagation due to acoustic attenuation, the raw data is amplified using a time-gain compensation coefficient of 0.4 dB/cm-MHz. The data is then filtered using a Gaussian filter centered about the transmit frequency to reduce the effect of noise outside the transmit frequency range [70]. During receive beamforming, sound speed

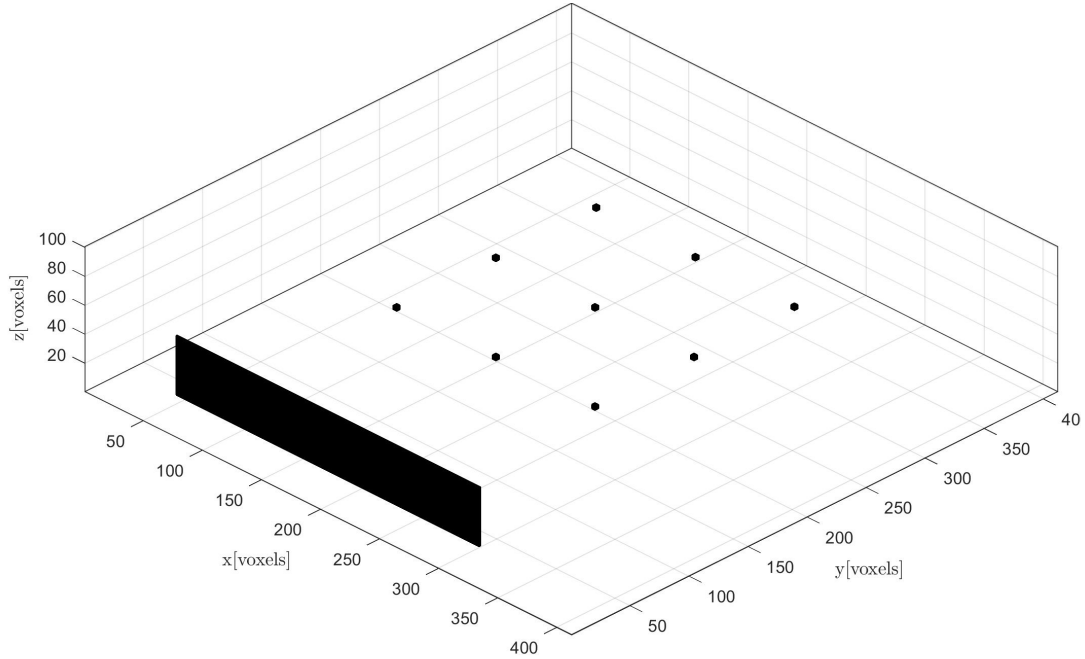


Figure 4.2: Simulation layout for CPWC imaging setup.

and thickness are estimated first for each layer using our SOS profiling approach (see section 3.2), followed by layer-by-layer phase-shift migration (see section 2.1.2). During migration, we set our step size to $\Delta z = \lambda/10$ and the Fourier domain grid size to $2^8 \times 2^{13}$. The individual migrated data frames corresponding to each θ value under consideration are then summed, followed by linear interpolation to increase the number of grid points on the x -axis. Further, we perform envelope detection to remove the high frequency variations and log compression by a compression ratio of 3 to reduce the dynamic range. The final step involves normalizing the data to the maximum within each layer, so that the envelope's data range is limited to $[0, 1]$. The resultant layer sub-images are stacked to form the entire image.

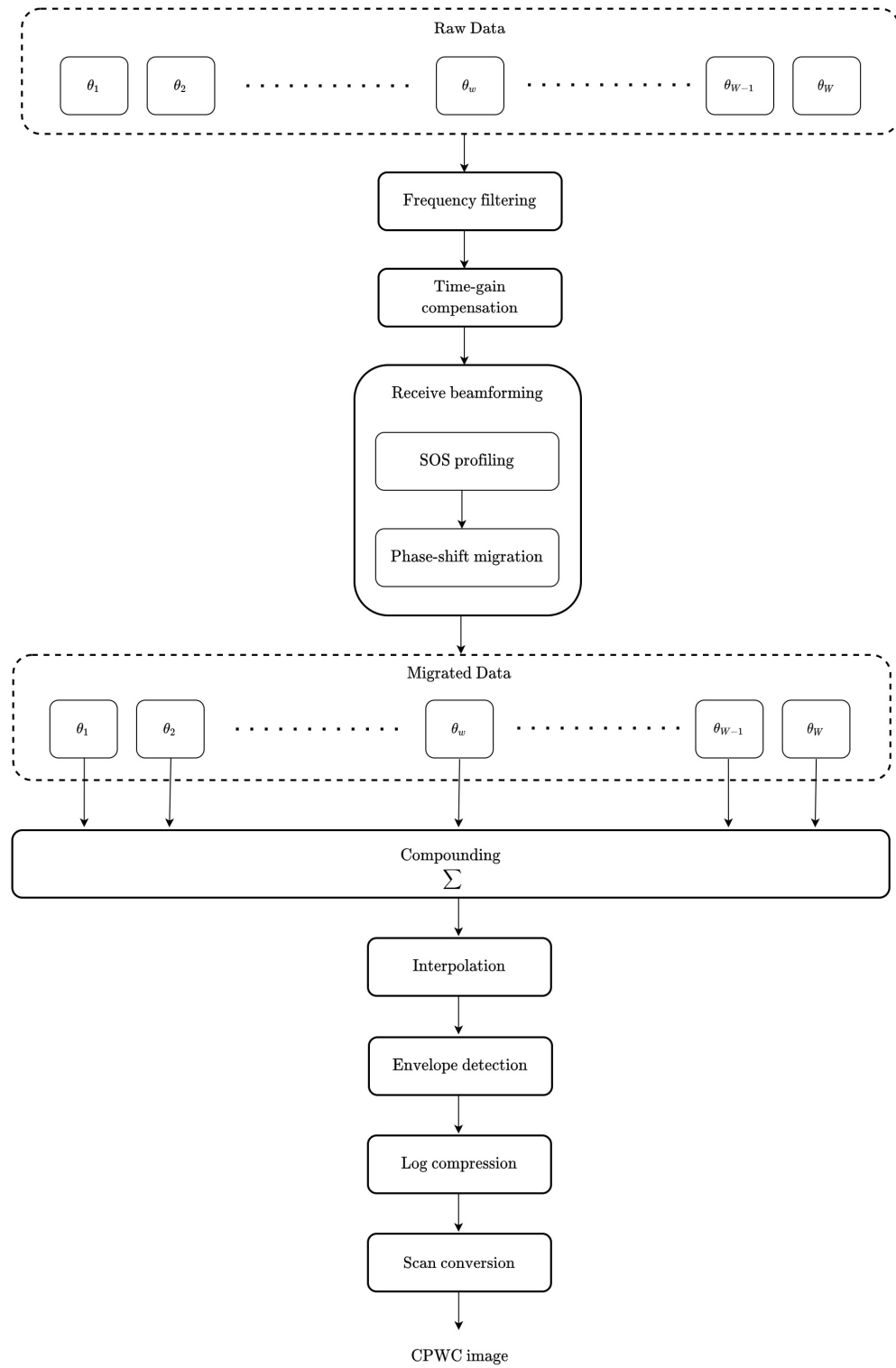


Figure 4.3: Processing steps for CPWC imaging setup.

4.1.2 Results and discussion

To evaluate our SOS profiling technique for CPWC imaging, we examine the performance of both PWPSM and LCPWPSM. We choose $\theta_a = 0^\circ$ and $\theta_b = 12^\circ$ and consider eight different cases, depending on the vectorization operation $\mathbf{V}\{\cdot\}$ used for sound speed estimation and the boundary detection operation $\mathbf{B}\{\cdot\}$ used for thickness estimation. Table 4.3 shows the cases and type of operations under consideration.

Case	Vectorization method	Boundary detection method
1	Stacking	Line detection in migrated data
2	Summing	Line detection in migrated data
3	Stacking	Peak detection in migrated data
4	Summing	Peak detection in migrated data
5	Stacking	Line detection in raw data
6	Summing	Line detection in raw data
7	Stacking	Peak detection in raw data
8	Summing	Peak detection in raw data

Table 4.3: Different cases for SOS profiling in CPWC imaging.

Figure 4.4 shows the migrated images and cross sectional targets obtained for PWPSM (original) and LCPWPSM (low-cost) using true values of sound speed and thickness as specified in Table 4.2. For the low-cost version, 99.99% of the energy was retained in the wavefield spectrum, yielding approximately 93% savings in multiplications.

Table 4.4 lists the lateral FWHM values for the upper, middle, and lower target groups of three points each, labeled L (leftmost), C (central) and R (rightmost). Comparing Figures 4.4(d) and 4.4(c), it can be observed that LCPWPSM has not caused any significant changes in the target resolution quality. The migrated image using LCPWPSM shows no visible changes in the position and the size of the targets or layer boundaries, except for a small vertical line artifact in the middle of the first layer. Figures 4.5 - 4.12 and Tables 4.5 - 4.12 show the migrated images and the estimates of sound speed and thickness for the eight cases listed in Table 4.3. For brevity, we do not show the corresponding target lateral cross-section images and FWHM data in this section; instead, they are collected in the Appendix A.

Our error in speed and thickness estimates are within 3.8% and 3.6%, respectively. For cases that used stacking-based vectorization, the average error in speed and thickness estimates were 1.41% and 1.66%, respectively. For cases that used summing-

based vectorization, the average error in speed and thickness estimates were 0.91% and 1.28%, respectively. For cases that used line-based boundary detection method, the average error in speed and thickness estimates were 1.03% and 1.41%, respectively. For cases that used peak-based boundary detection method, the average error in speed and thickness estimates were 1.29% and 1.48%, respectively. For cases that used raw data for boundary detection, the average error in speed and thickness estimates were 1.52% and 0.87%, respectively. For cases that used migrated data for boundary detection, the average error in speed and thickness estimates were 1.43% and 1.06%, respectively.

Target group	z mm	FWHM,mm		
		L	C	R
Upper	21.637	1.367	1.181	1.365
Middle	34.573	1.605	1.329	1.609
Lower	47.663	1.910	1.643	1.923

(a)

Target group	z mm	FWHM,mm		
		L	C	R
Upper	21.637	1.369	1.184	1.372
Middle	34.650	1.602	1.320	1.606
Lower	47.663	1.908	1.642	1.922

(b)

Table 4.4: Target resolution quality for true SOS profile. (a) Original (PWPSM), (b) Low-cost (LCPWPSM).

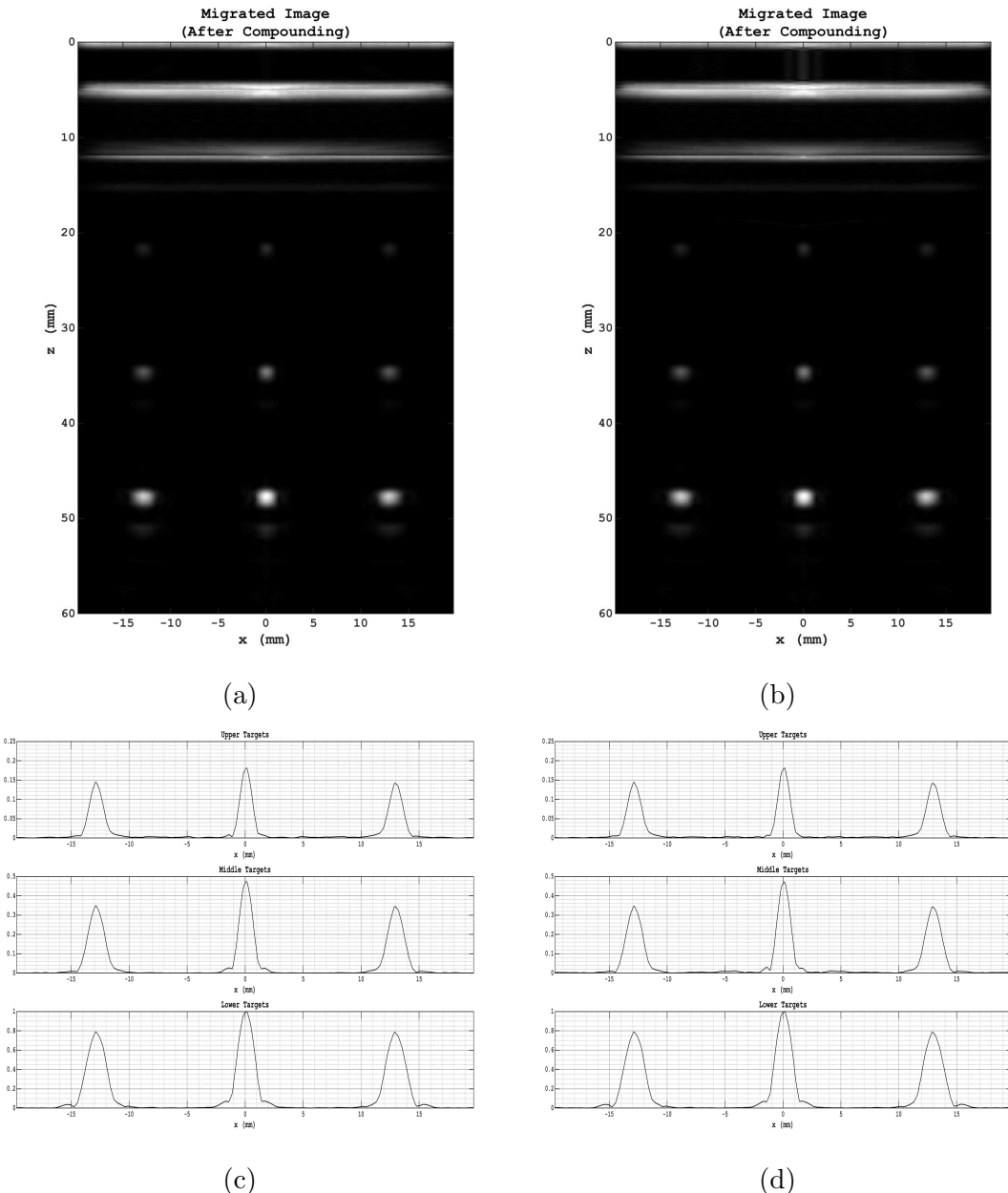


Figure 4.4: Migration results using true SOS profile. Migrated images: (a) Original (PWPSM), (b) Low-cost (LCPWPSM); Lateral cross-section of targets: (c) Original (PWPSM), (d) Low-cost (LCPWPSM).

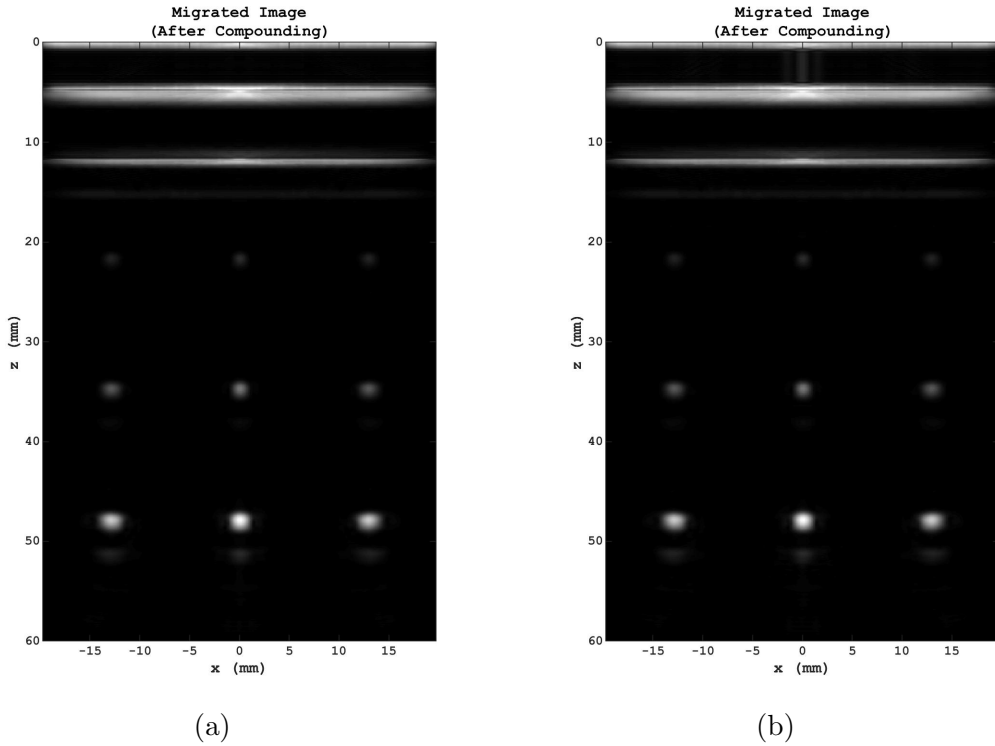


Figure 4.5: Migration results using estimated SOS profile, case 1. (a) Original (PW-PSM), (b) Low-cost (LCPWPSM).

Layer	Original				Low-cost			
	Speed		Thickness		Speed		Thickness	
	est., m/s	error, %	est., mm	error, %	est., m/s	error, %	est., mm	error, %
I	1560	1.30	4.85	3.00	1560	1.30	4.85	3.00
II	3130	2.13	6.93	1.00	3120	2.44	6.93	1.00
III	1550	0.65	51.66	0.43	1550	0.65	51.66	0.43

Table 4.5: Estimated speed and thickness, case 1.

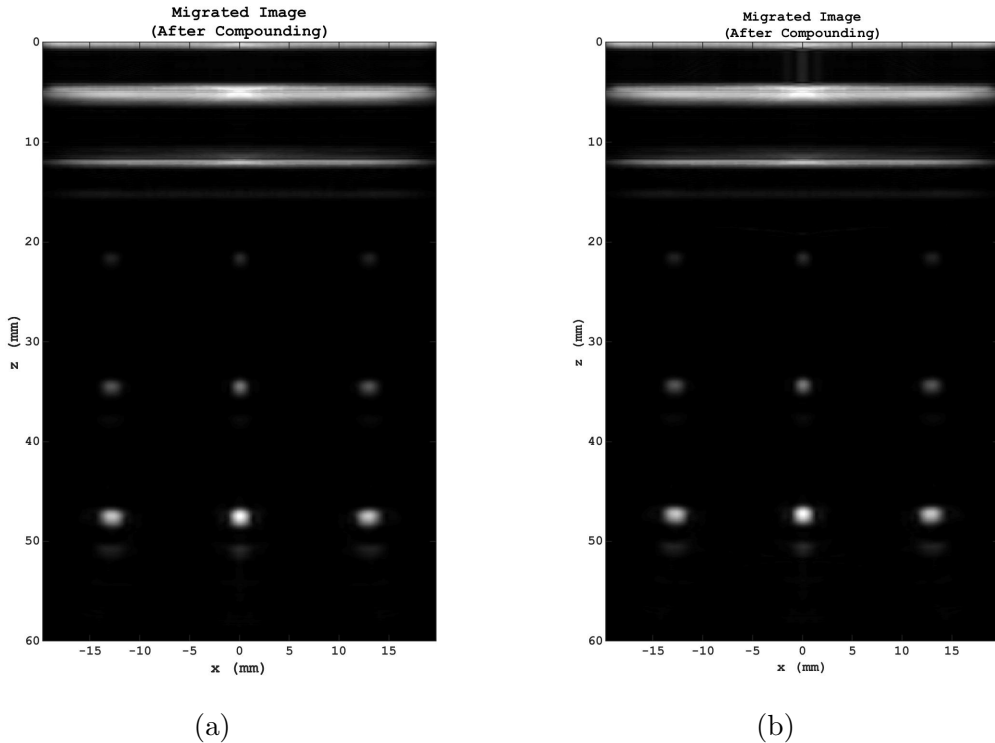


Figure 4.6: Migration results using estimated SOS profile, case 2. (a) Original (PW-PSM), (b) Low-cost (LCPWPSM).

Layer	Original				Low-cost			
	Speed		Thickness		Speed		Thickness	
	est., m/s	error, %	est., mm	error, %	est., m/s	error, %	est., mm	error, %
I	1550	0.65	4.85	3.00	1550	0.65	4.85	3.00
II	3190	0.25	7.01	0.14	3190	0.25	7.01	0.14
III	1530	0.65	51.58	0.27	1520	1.30	51.66	0.43

Table 4.6: Estimated speed and thickness, case 2.

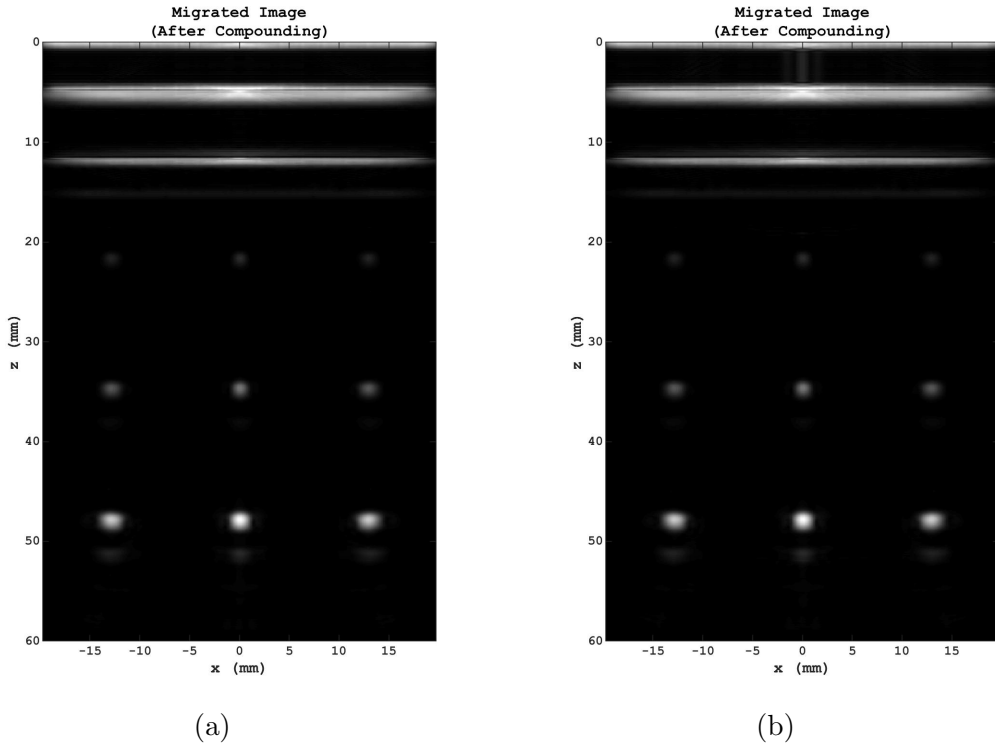


Figure 4.7: Migration results using estimated SOS profile, case 3. (a) Original (PW-PSM), (b) Low-cost (LCPWPSM).

Layer	Original				Low-cost			
	Speed		Thickness		Speed		Thickness	
	est., m/s	error, %	est., mm	error, %	est., m/s	error, %	est., mm	error, %
I	1560	1.30	4.85	3.00	1560	1.30	4.85	3.00
II	3130	2.13	6.85	2.14	3120	2.44	6.85	2.14
III	1550	0.65	51.74	0.58	1520	1.30	51.66	0.43

Table 4.7: Estimated speed and thickness, case 3.

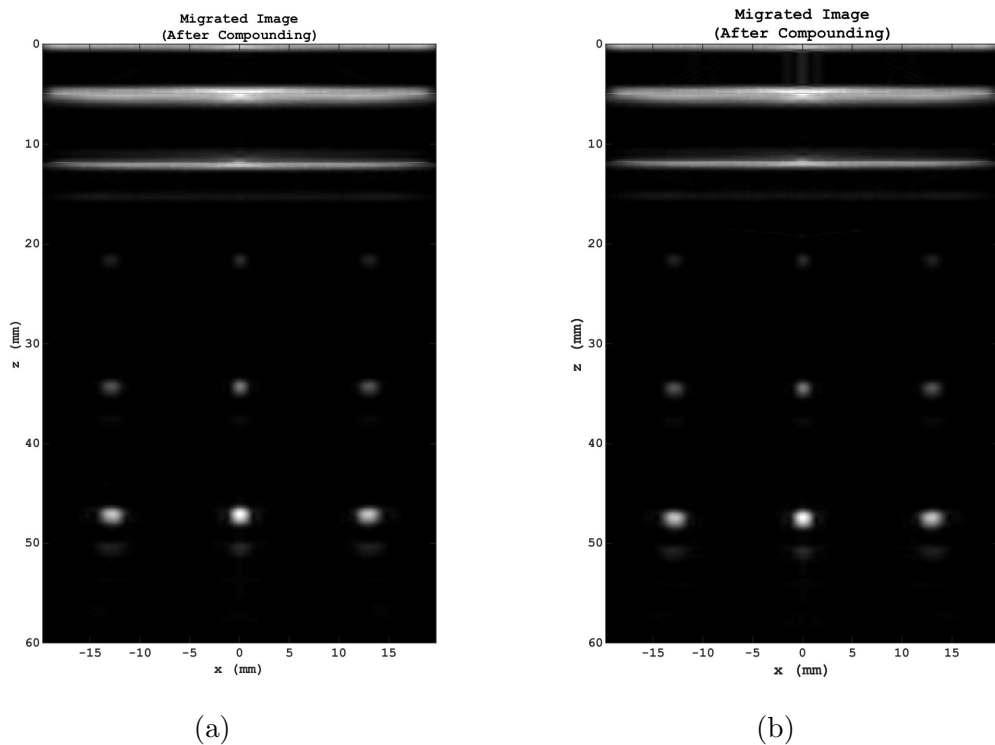


Figure 4.8: Migration results using estimated SOS profile, case 4. (a) Original (PW-PSM), (b) Low-cost (LCPWPSM).

Layer	Original				Low-cost			
	Speed		Thickness		Speed		Thickness	
	est., m/s	error, %	est., mm	error, %	est., m/s	error, %	est., mm	error, %
I	1550	0.65	5.00	0.00	1550	0.65	5.00	0.00
II	3320	3.81	6.78	3.14	3260	1.93	6.78	3.14
III	1510	1.94	51.66	0.43	1530	0.65	51.66	0.43

Table 4.8: Estimated speed and thickness, case 4.

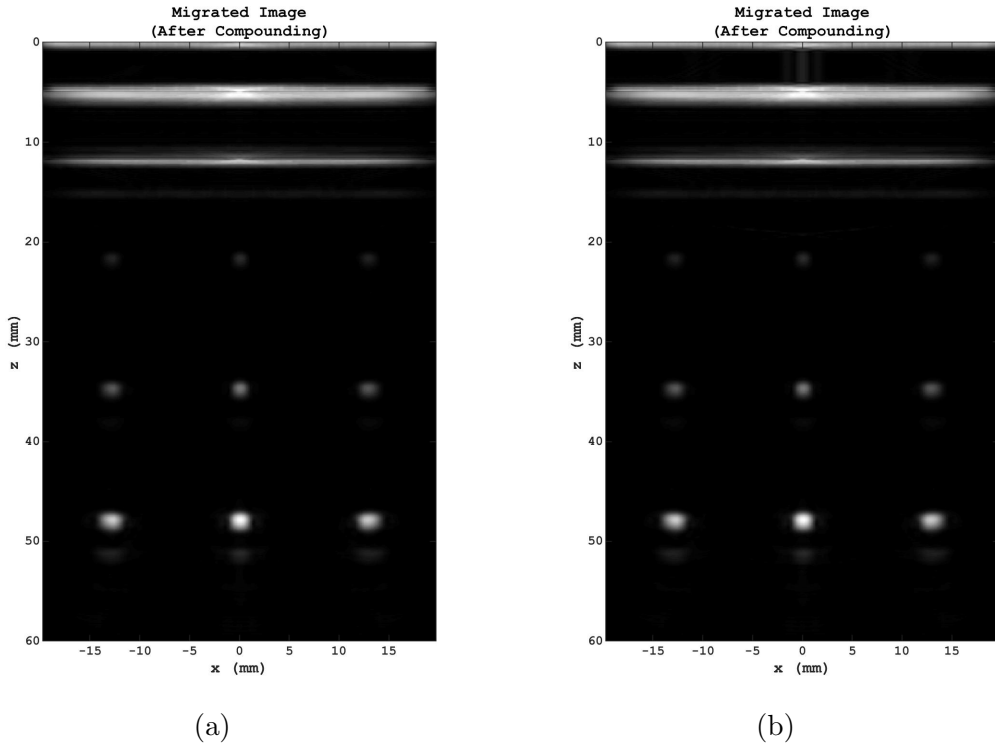


Figure 4.9: Migration results using estimated SOS profile, case 5. (a) Original (PW-PSM), (b) Low-cost (LCPWPSM).

Layer	Original				Low-cost			
	Speed		Thickness		Speed		Thickness	
	est., m/s	error, %	est., mm	error, %	est., m/s	error, %	est., mm	error, %
I	1560	1.30	4.87	2.60	1560	1.30	4.87	2.60
II	3130	2.13	6.88	1.71	3130	2.13	6.88	1.71
III	1550	0.65	51.69	0.49	1550	0.65	51.69	0.49

Table 4.9: Estimated speed and thickness, case 5.

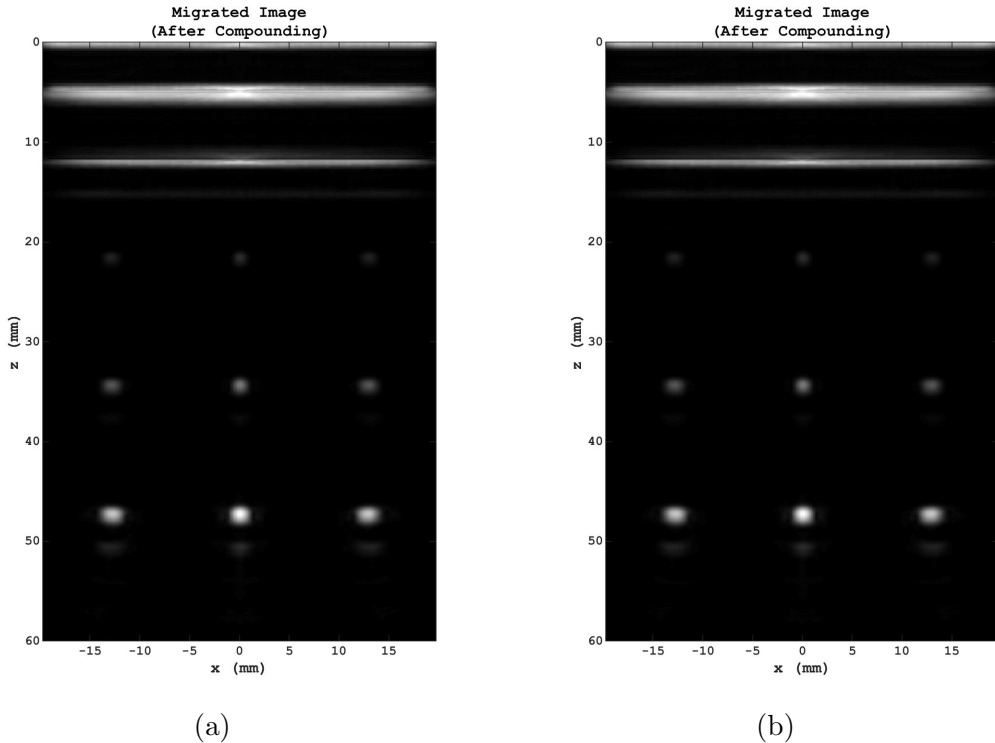


Figure 4.10: Migration results using estimated SOS profile, case 6. (a) Original (PW-PSM), (b) Low-cost (LCPWPSM).

Layer	Original				Low-cost			
	Speed		Thickness		Speed		Thickness	
	est., m/s	error, %	est., mm	error, %	est., m/s	error, %	est., mm	error, %
I	1550	0.65	4.83	3.40	1550	0.65	4.83	3.40
II	3190	0.25	7.02	0.28	3190	0.25	7.02	0.28
III	1520	1.30	51.59	0.29	1520	1.30	51.59	0.29

Table 4.10: Estimated speed and thickness, case 6.

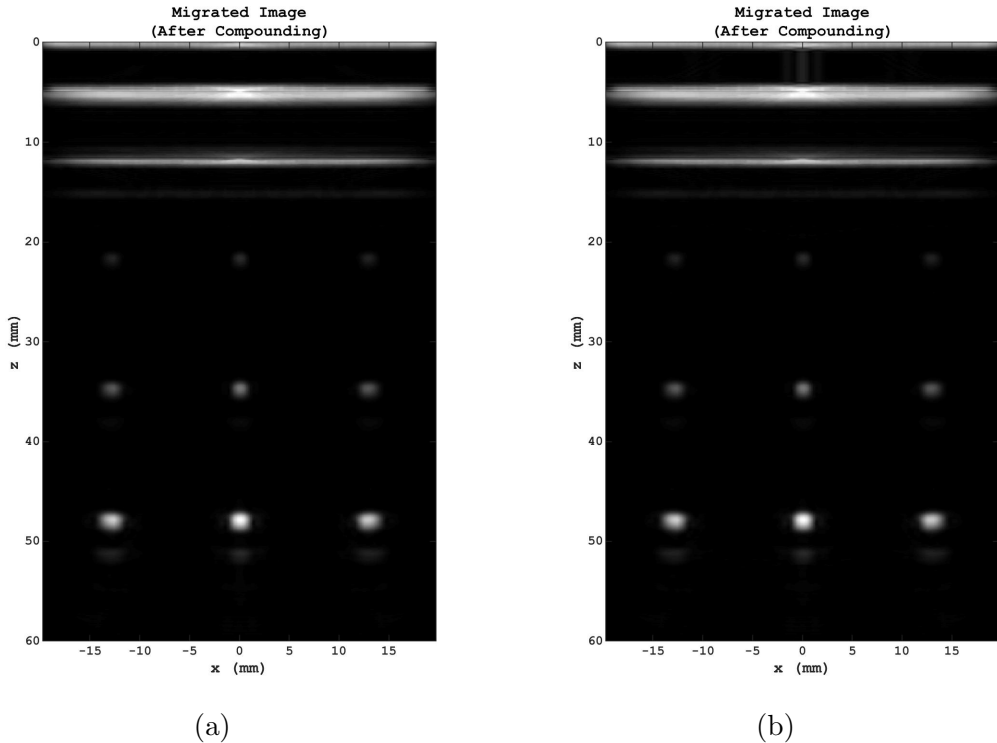


Figure 4.11: Migration results using estimated SOS profile, case 7. (a) Original (PW-PSM), (b) Low-cost (LCPWPSM).

Layer	Original				Low-cost			
	Speed		Thickness		Speed		Thickness	
	est., m/s	error, %	est., mm	error, %	est., m/s	error, %	est., mm	error, %
I	1560	1.30	4.85	3.00	1560	1.30	4.85	3.00
II	3130	2.13	6.89	1.57	3130	2.13	6.89	1.57
III	1550	0.65	51.70	0.50	1550	0.65	51.70	0.50

Table 4.11: Estimated speed and thickness, case 7.

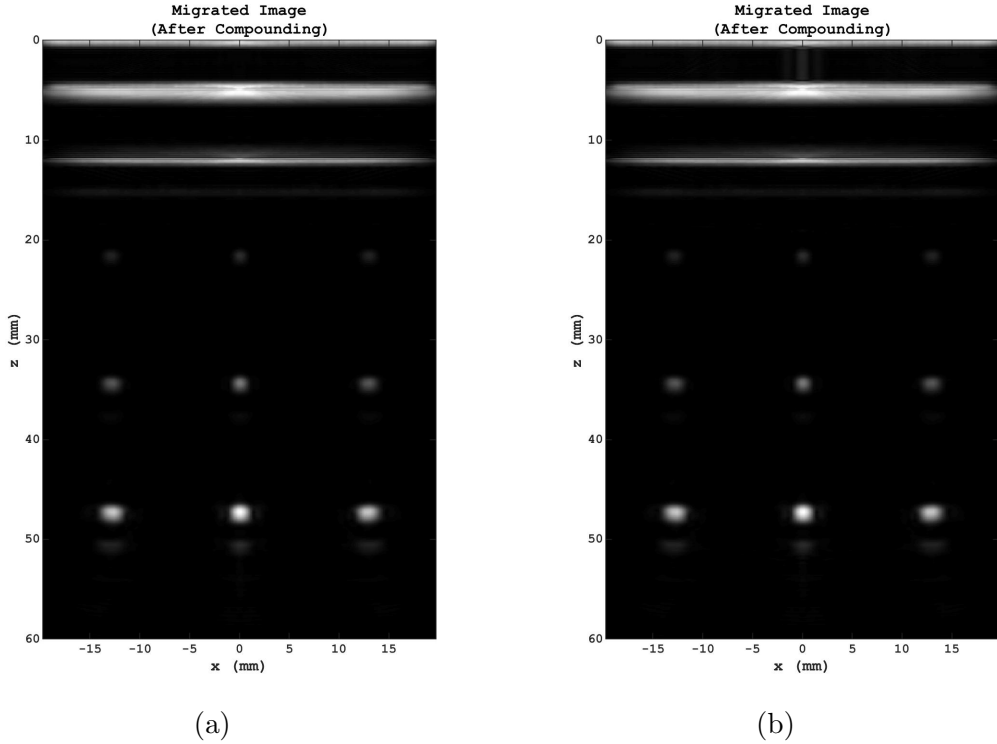


Figure 4.12: Migration results using estimated SOS profile, case 8. (a) Original (PW-PSM), (b) Low-cost (LCPWPSM).

Layer	Original				Low-cost			
	Speed		Thickness		Speed		Thickness	
	est., m/s	error, %	est., mm	error, %	est., m/s	error, %	est., mm	error, %
I	1550	0.65	4.82	3.60	1550	0.65	4.82	3.60
II	3200	0.06	7.04	0.57	3200	0.06	7.04	0.57
III	1520	1.30	51.58	0.27	1520	1.30	51.58	0.27

Table 4.12: Estimated speed and thickness, case 8.

Table 4.13(a) and 4.13(b) show the structural similarity index (SSIM) and the Pearson correlation coefficient values between the reference image obtained using true SOS profile and the images obtained using estimated SOS profile, for all eight cases involving the original (PWPSM) and low-cost (LCPWPSM) versions. The SSIM values are between 0.935 and 0.964 for PWPSM and between 0.931 and 0.958 for LCPWPSM

indicating no significant changes in the reconstructed image structure. The Pearson correlation coefficient values are between 0.951 and 0.977 for PWPSM and between 0.955 and 0.973 for LCPWPSM indicating good correlation with the reference image.

Structural similarity index (SSIM)								
Case	1	2	3	4	5	6	7	8
Original	0.944	0.944	0.947	0.964	0.962	0.945	0.961	0.935
Low-cost	0.941	0.940	0.945	0.958	0.956	0.940	0.956	0.931

(a)

Pearson correlation coefficient								
Case	1	2	3	4	5	6	7	8
Original	0.956	0.962	0.951	0.977	0.969	0.959	0.969	0.958
Low-cost	0.960	0.962	0.955	0.973	0.969	0.958	0.969	0.957

(b)

Table 4.13: CPWC image similarity when using estimated vs. true SOS profile. (a) Structural similarity index, (b) Pearson correlation coefficient.

4.2 Evaluation results for layer thickness estimation in SA imaging

In the previous section, we have evaluated our SOS profiling approach using a simulated dataset of CPWC imaging of a three-layer medium. In this section, we provide results for a real-data special case, an experimental SA imaging dataset of a three-layer medium (assuming that the sound speed values are already known), to be used to evaluate our thickness estimation approach on its own.

4.2.1 Dataset description

We use the experimental SA imaging dataset provided by Skjelvareid *et al.* [18][71]. The dataset was obtained using the experimental setup shown in Figure 4.13. A 31-mm-thick acrylic glass block was placed on top of a 50-mm-thick aluminum block and immersed in the water tank. Each block had four side-drilled holes that were

1.6 mm in diameter and 30 mm deep, with a vertical spacing of 6 mm and 10 mm between the holes in the acrylic glass block and the aluminum block, respectively. To prevent a dominating shadow from the upper holes onto the lower holes, the blocks were shifted horizontally by approximately 10 mm. An array of four steel pins, 0.3 mm in diameter, were placed above these two blocks with a vertical spacing of 5 mm and a horizontal spacing of 20 mm. This arrangement was subjected to a B-scan using a 2.25-MHz transducer (6 mm in diameter) that moved in steps of 1 mm with a sampling frequency of 12.5 MHz. In 111 positions, 1040 time samples were recorded, resulting in a raw dataset of size 111×1040 in (x, t) domain. To compensate for the limited dynamic range of the signal acquisition system, reflections from the interface between water and acrylic glass were damped by 10 dB, and reflections from within the aluminum layer were amplified by 20 dB during scanning.

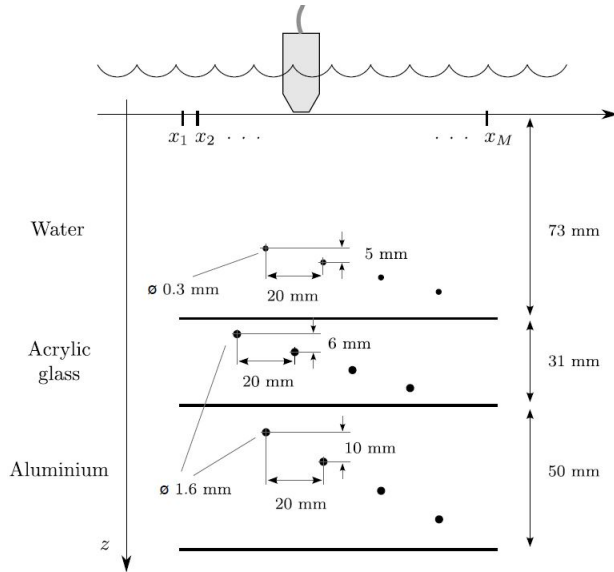


Figure 4.13: Experimental setup for SA imaging [18, 71].

Medium layer	Layer material	Thickness mm	Speed m/s
I	water	73.33	1480
II	acrylic glass	31.00	2730
III	aluminum	54.00	6320

Table 4.14: True SOS profile for SA imaging dataset.

4.2.2 Results and discussion

We show our results for four different cases, depending on the boundary detection operation $\mathbf{B}\{\cdot\}$ used for thickness estimation. They are listed in Table 4.15.

Case	Boundary detection method
1	Line detection in migrated data
2	Peak detection in migrated data
3	Line detection in raw data
4	Peak detection in raw data

Table 4.15: Different cases for thickness estimation in SA imaging.

Figure 4.14 shows the migrated images (over 40-dB dynamic range) obtained for the original SA phase shift migration method (SAPSM) and its low-cost alternative (LCSAPSM) using true thickness values listed in Table 4.14. For the low-cost version, 99% of the energy was retained in the wavefield spectrum, yielding approximately 77% savings in multiplications.

The steel pins and holes are seen as four distinct reflectors in each layer. Their width increases with depth as a result of the divergence of the transducer beam. Some spurious reflections can be seen in the second and the third layer due to multiple echoes caused by scattering. The steel pins and holes appear slightly enlarged in Figure 4.14(b) as compared to 4.14(a) but there are no visible changes in their position.

Figures 4.15 - 4.18 and Tables 4.16 - 4.19 show the migrated images that rely on our estimates of each layer's thickness for four cases listed in Table 4.15. The error in thickness estimates are within 0.98%. For cases that used line-based boundary detection, the average error in thickness estimates was 0.49%. For cases that used peak-based boundary detection, the average error in thickness estimates was 0.51%. For cases that used raw data for boundary detection, the average error in thickness estimates was 0.54%. For cases that used migrated data for boundary detection, the average error in thickness estimates was 0.46%. We should note that LCSAPSM yields the same thickness estimates as those by SAPSM, while achieving a 77% reduction in the number of complex multiplications performed during PSM-based SOS profiling.

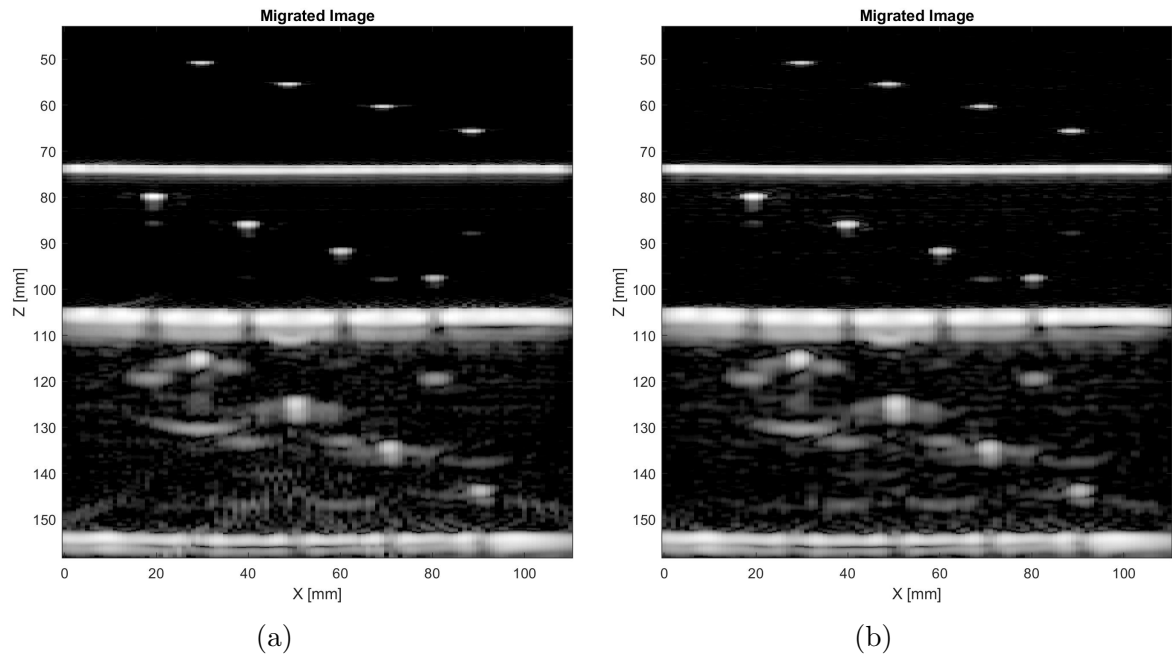


Figure 4.14: Migration results using true thickness. (a) Original (SAPSM), (b) Low-cost (LCSAPSM).

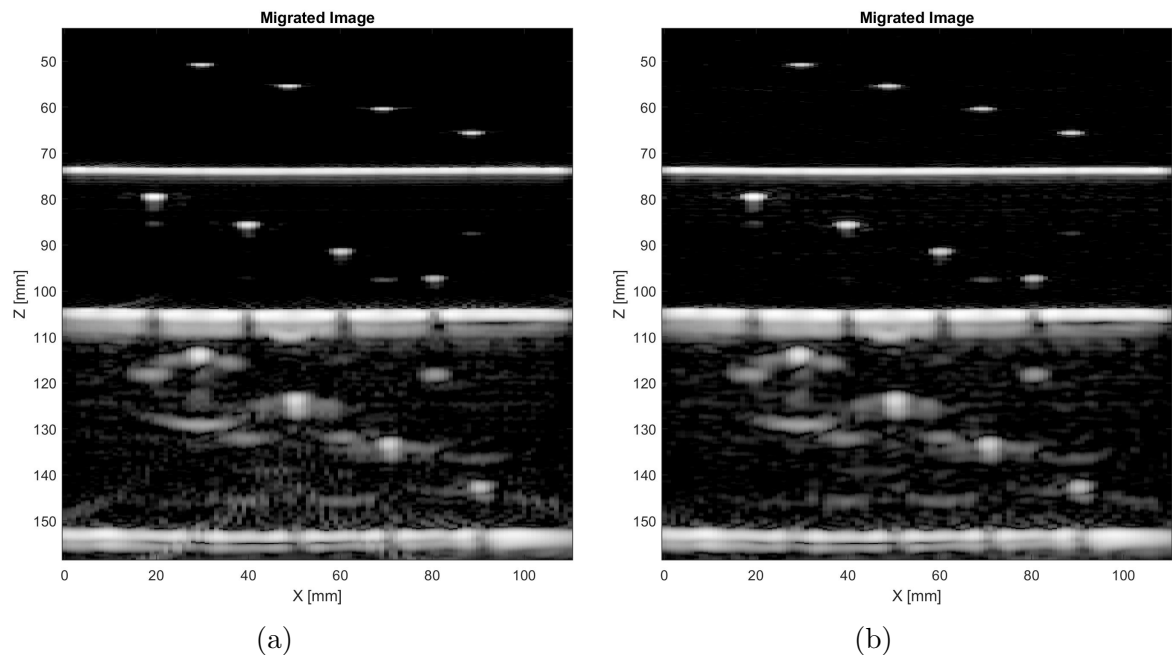


Figure 4.15: Migration results using estimated thickness, case 1. (a) Original (SAPSM), (b) Low-cost (LCSAPSM).

Layer	Original		Low-cost	
	est., mm	error, %	est., mm	error, %
I	73.63	0.51	73.63	0.51
II	31.08	0.26	31.08	0.26
III	53.59	0.76	53.59	0.76

Table 4.16: Thickness estimates, case 1.

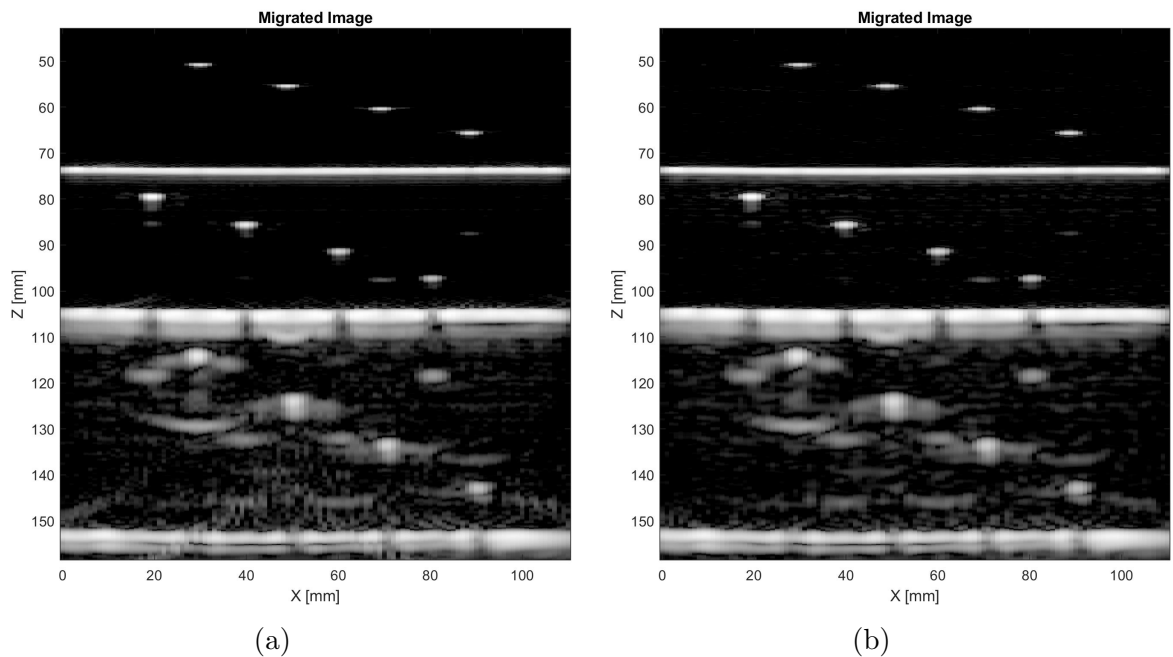


Figure 4.16: Migration results using estimated thickness, case 2. (a) Original (SAPSM), (b) Low-cost (LCSAPSM).

Layer	Original		Low-cost	
	est., mm	error, %	est., mm	error, %
I	73.63	0.41	73.63	0.41
II	30.89	0.35	30.89	0.35
III	53.77	0.43	53.77	0.43

Table 4.17: Thickness estimates, case 2.

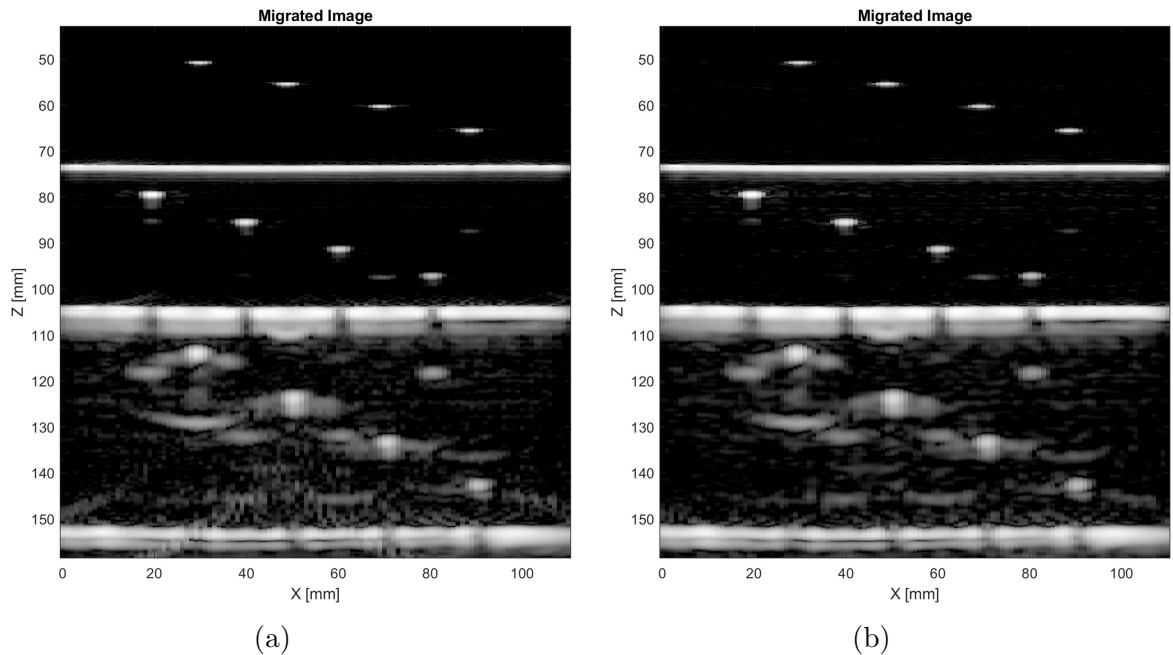


Figure 4.17: Migration results using estimated thickness, case 3. (a) Original (SAPSM), (b) Low-cost (LCSAPSM).

Layer	Original		Low-cost	
	est., mm	error, %	est., mm	error, %
I	73.70	0.50	73.70	0.50
II	30.90	0.32	30.90	0.32
III	53.69	0.57	53.69	0.57

Table 4.18: Thickness estimates, case 3.

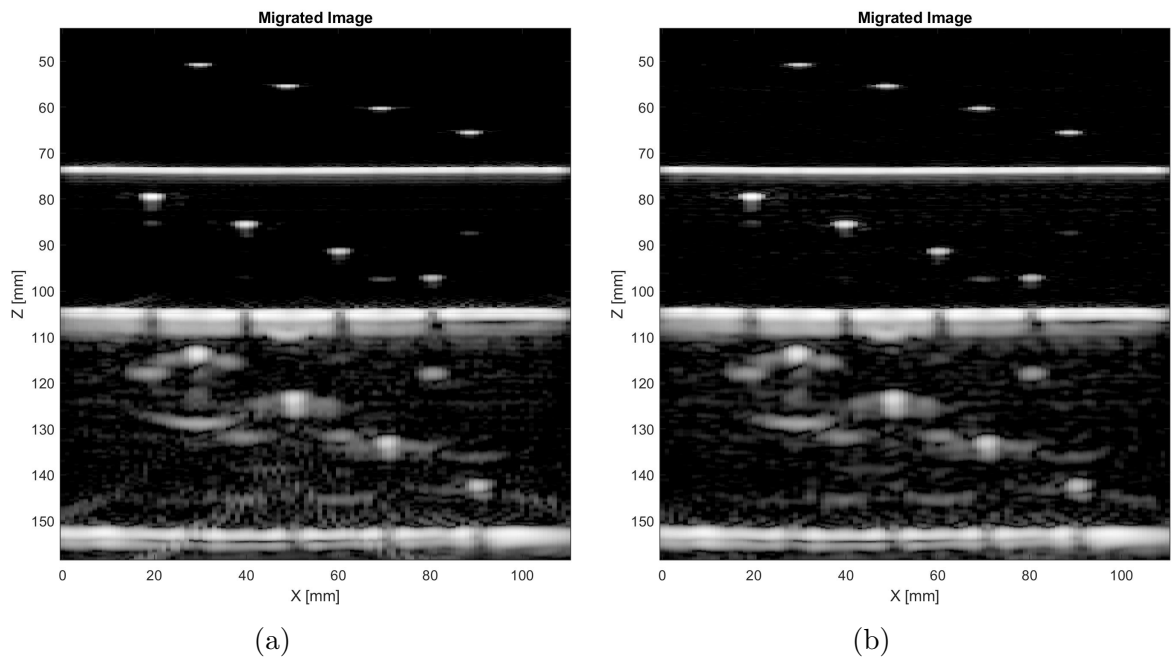


Figure 4.18: Migration results using estimated thickness, case 4. (a) Original (SAPSM), (b) Low-cost (LCSAPSM).

Layer	Original		Low-cost	
	est., mm	error, %	est., mm	error, %
I	73.70	0.50	73.70	0.50
II	31.12	0.39	31.12	0.39
III	53.47	0.98	53.47	0.98

Table 4.19: Thickness estimates, case 4.

Table 4.20(a) and 4.20(b) show the structural similarity index (SSIM) and the Pearson correlation coefficient values between the reference image obtained using true thickness values and the images obtained using estimated thickness values, for all four cases involving the original (SAPSM) and low-cost (LCSAPSM) versions. The SSIM values are between 0.826 and 0.848 for SAPSM and between 0.810 and 0.830 for LCSAPSM indicating relatively minor changes in the structure of the images obtained with estimated thickness values. These changes are likely due to mismatch in the position of the layer boundaries, differences in resolution, contrast and luminance of reflectors, and due to presence of clutter. The Pearson correlation coefficient values are between 0.745 and 0.815 for SAPSM and between 0.743 and 0.811 for LCSAPSM indicating relatively good correlation with the reference image.

Structural similarity index (SSIM)				
Cases	1	2	3	4
Original	0.826	0.841	0.848	0.827
Low-cost	0.810	0.824	0.830	0.811

(a)

Pearson correlation coefficient				
Cases	1	2	3	4
Original	0.745	0.792	0.815	0.753
Low-cost	0.743	0.792	0.811	0.752

(b)

Table 4.20: SA image similarity when using estimated vs. true SOS profile. (a) Structural similarity index, (b) Pearson correlation coefficient.

4.3 Evaluation results for sound speed estimation in single-layer CPWC imaging

In the previous section, we have evaluated our thickness estimation approach using SA experimental data obtained from a three-layer medium (assuming that the sound speed values are already known). Here, we provide additional results for another real-data special case, CPWC imaging of a single-layer medium, to be used to evaluate our sound speed estimation approach on its own. For such constant-velocity medium, PWPSM can be replaced with PW Stolt’s migration [25, 72] which is a much faster method.

4.3.1 Dataset description

The dataset in question, provided by PICMUS [73], consists of a 75 plane-wave sequence (with θ ranging from -16° to 16°) of the cross-section and longitudinal section of the carotid artery. This dataset was acquired using a Verasonics Vantage 256 research scanner (Verasonics Inc., Redmond, WA) with a L11 probe (128 transducer elements, 0.30-mm pitch) that emitted a 5.208-MHz ultrasound plane wave (2.5 cy-

cles, 67% pulse bandwidth) and sampled 1536 times at 20.832 MHz. The resulting dataset had a size of 128×1536 for each angle in (x, t) domain.

4.3.2 Results and discussion

We perform sound speed estimation using $\theta_a = 0^\circ$ and $\theta_b = 13^\circ$ for this dataset. Figure 4.19 shows migrated images (over 60-dB dynamic range) using a subset of 11 plane waves, assuming the standard value of 1540 m/s as the true speed of sound. Figures 4.20 and 4.21 show the migrated images using sound speed estimates obtained by stacking-based and summing-based vectorization $\mathbf{V}\{\cdot\}$, respectively. Table 4.21 shows our estimated values and their respective errors. As one can see, the error in sound speed estimates are within 0.91%.

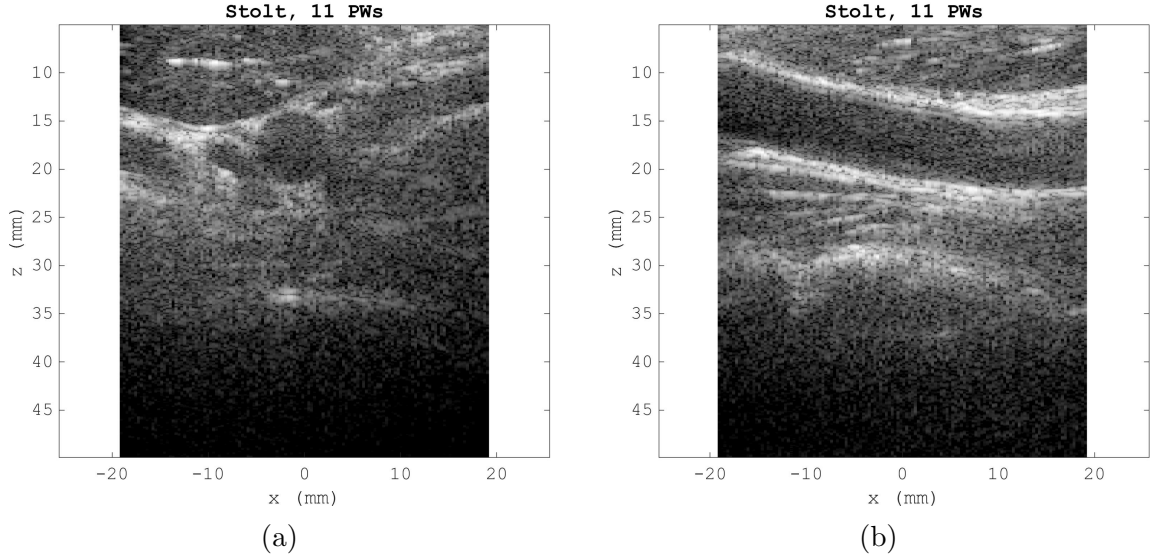


Figure 4.19: Migrated carotid artery images using true speed. (a) Cross-section, (b) Longitudinal section.

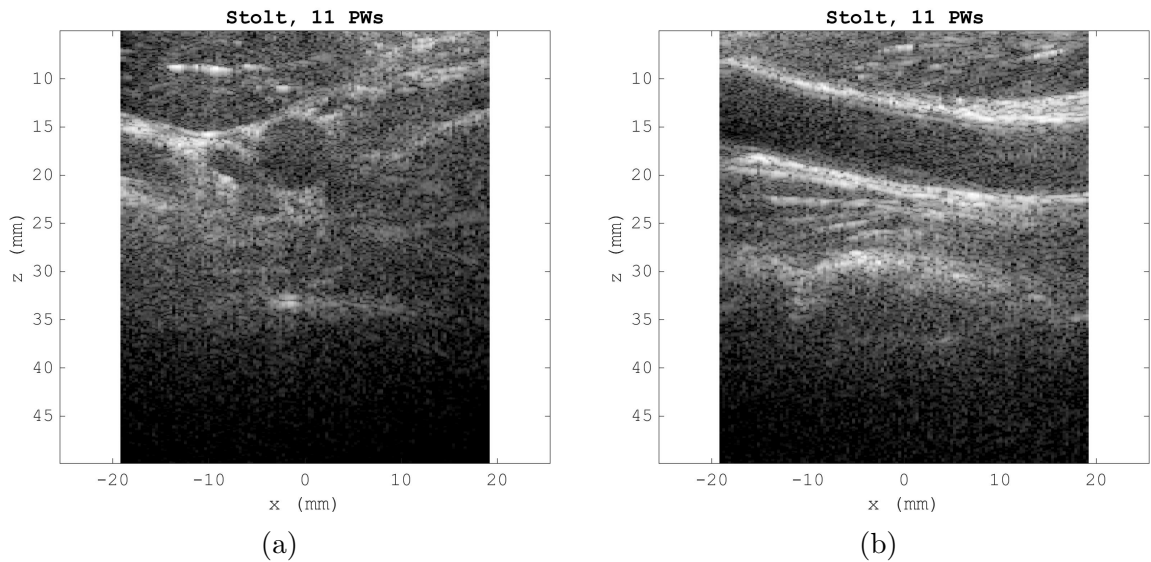


Figure 4.20: Migrated carotid artery images using estimated speed (stacking-based vectorization). (a) Cross-section, (b) Longitudinal section.

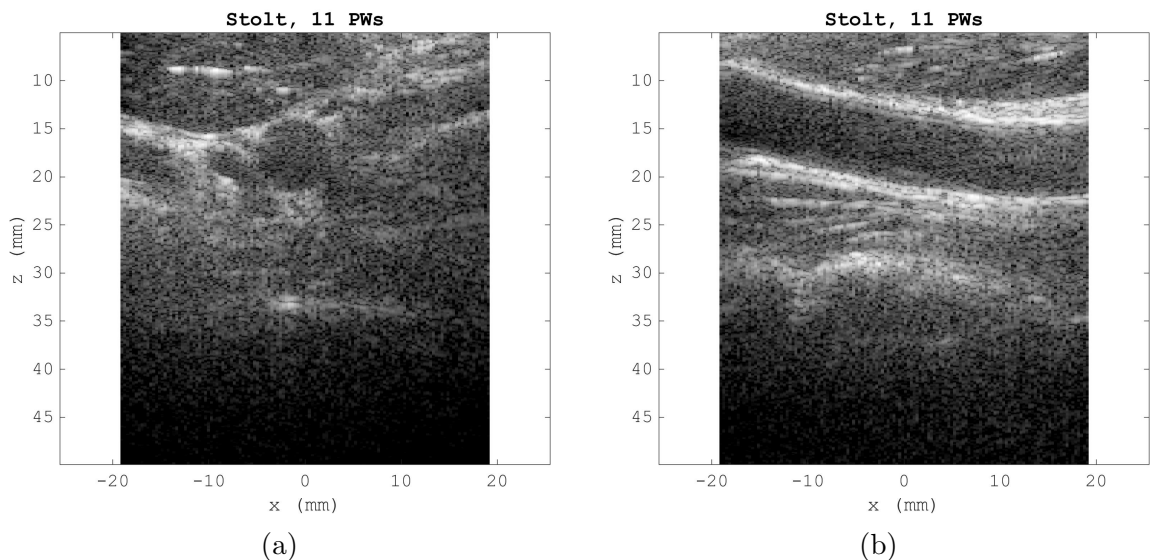


Figure 4.21: Migrated carotid artery images using estimated speed (summing-based vectorization). (a) Cross-section, (b) Longitudinal section.

Image	Stacking		Summing	
	est., m/s	error, %	est., m/s	error, %
cross-section	1542	0.13	1526	0.91
longitudinal section	1552	0.78	1553	0.84

Table 4.21: Speed estimates for PW Stolt's migration.

Table 4.22(a) and 4.22(b) show the structural similarity index (SSIM) and the Pearson correlation coefficient values between the reference images obtained using true sound speed values and the images obtained using estimated sound speed values. The SSIM values are between 0.981 and 0.999 for images obtained using both stacking-based and summing-based vectorization methods, which indicates nearly identical structure in comparison to the reference images. The Pearson correlation coefficient values are between 0.975 and 0.999 for images obtained using both stacking-based and summing-based vectorization methods, which indicates excellent correlation with the reference images.

Structural similarity index (SSIM)		
Image	Stacking	Summing
cross-section	0.999	0.981
longitudinal section	0.985	0.982

(a)

Pearson correlation coefficient		
Image	Stacking	Summing
cross-section	0.999	0.982
longitudinal section	0.978	0.975

(b)

Table 4.22: Constant-velocity image similarity using estimated vs. 1540 m/s speed.
(a) Structural similarity index, (b) Pearson correlation coefficient.

4.4 Summary

In this chapter, we have presented the evaluation results for our proposed SOS profiling method. For each layer, SOS profiling involves two steps: 1) finding sound speed estimates using the cosine similarity criterion, and 2) finding layer thickness estimates via end-of-layer boundary detection, using the sound speed estimates from the previous step. We have evaluated two vectorization approaches – stacking and summing – for sound speed estimation, and two boundary detection approaches – peak-based and line-based – for layer thickness estimation. For the latter, we have considered both raw and migrated zero-angle data. Finally, we have also presented evaluation results for our low-cost version of the PW phase-shift migration method that reduces the number of complex multiplications during PSM.

Our speed estimation errors are within 4% of their true values for PWPSM and LCPWPSM and within 1% of their true values for single-layer CPWC imaging using PW Stolt’s migration. Our thickness estimation errors are within 4% of their true values for PWPSM and LCPWPSM and within 0.6% of their true values for SAPSM and LCSAPSM.

The average error in speed estimates using stacking-based vectorization in PWPSM and LCPWPSM cases is 1.36% and 1.46% respectively, and in case of PW Stolt’s migration, it is 0.46%. The average error in speed estimates using summing-based vectorization in PWPSM and LCPWPSM cases is 1.01% and 1.22% respectively, and in case of PW Stolt’s migration, it is 0.88%. Note that stacking is more expensive compared to summing, as the former results in a larger vector $s_{\theta_k}(z)$ due to column concatenation, which leads to more expensive cosine similarity computations. However, stacking preserves individual pixels in the image, unlike summing where columns of the image are summed together. In general, a strong reflector might corrupt the cosine similarity value when summing is used.

The average error in thickness estimates using line-based boundary detection in PWPSM and LCPWPSM cases is 1.38% and 1.40% respectively, and in both SAPSM and LCSAPSM cases, it is 0.48%. The average error in thickness estimates for peak-based boundary detection in both PWPSM and LCPWPSM cases is 1.59%, and in both SAPSM and LCSAPSM cases, it is 0.51%. Note that line detection is more expensive compared to peak detection, as the former involves using the computation-intensive Hough transform. Cheaper peak-based boundary detection (where we sum the data along the x -axis and use the resulting z -axis vector for peak detection) may

give false positive results if a horizontally stretched reflector stronger than the end-of-layer boundary is present. If migrated data is used for boundary detection, the average error in thickness estimates is 1.42% in PWPSM, 1.43% in LCPWPSM, and 0.45% in both SAPSM and LCSAPSM cases. If raw data is used, the average error in thickness estimates is 1.52% in PWPSM, 1.53% in LCPWPSM, and 0.54% in both SAPSM and LCSAPSM cases.

From the above results, minimal difference in performance can be observed between PWPSM and LCPWPSM (saving 93% of complex multiplications during PSM). Similarly, LCSAPSM also matched the performance of SAPSM while offering 76% savings.

Chapter 5

Conclusion and Future work

This chapter provides a summary of our main results and outlines different potential directions for future development and research work.

5.1 Conclusion

This thesis describes a two-step approach to SOS profiling for CPWC ultrasound imaging of stratified media. For each medium layer, we first estimate its sound speed based on cosine similarity (obtained for two vectors derived from migrated data corresponding to two PW emission angles), and then we find the layer thickness by means of boundary detection (based on our sound speed estimate). For speed estimation we considered two different ways to vectorize migrated data: 1) summing, whereby the (z, x) -domain data matrix columns are combined into a z -axis vector via summation over the x -axis, and 2) stacking, whereby the said data matrix is flattened by concatenating its columns into one. For layer thickness estimation, we considered two different ways of detecting an end-of-layer boundary: 1) peak detection, where we look for a peak location within a vector obtained from an image section, and 2) line detection, where we look for a horizontal line in an image section using the Hough transform. We also considered two choices of the said image sections: 1) migrated data over a known depth range from $d_{(l)}^{\min}$ to $d_{(l)}^{\max}$ for a given layer l , and 2) zero-angle raw data over an estimated travel-time range from $t_{(l)}^{\min}$ to $t_{(l)}^{\max}$ (derived from $d_{(l)}^{\min}$ and $d_{(l)}^{\max}$). Putting all of the aforementioned options together yields a total of eight different cases under consideration, which we have examined in Chapter 4. Finally, we have also described a computationally cheaper extrapolation process (based on a

spectral energy threshold), which leads to a significant reduction in the number of complex multiplications performed during PSM.

To evaluate our SOS profiling approach, we performed experiments over different datasets. First, we used nine-angle CPWC data produced by the K-WAVE toolbox that simulated ultrasound propagation in the three-layer medium, mimicking tissue-bone-tissue layer arrangement. The maximum errors of our speed and thickness estimates were 3.81% and 3.60%, respectively. Approximately, 93% saving in complex multiplications were achieved when we used our low-cost PSM migration method. Second, we used real monostatic SA data, obtained for the three-layer medium (water-glass-metal), to evaluate our thickness estimation step on its own, using the known values of sound speed for the layer materials. Our thickness estimates were accurate within a 0.98% error margin, and our low-cost PSM method resulted in 76% fewer complex multiplications during PSM. Finally, we used in-vivo data of CPWC imaging of the carotid artery (provided by PICMUS) to evaluate our sound speed estimation step on its own, as there is only one layer present (soft tissue). The maximum error of our speed estimates was only 0.91%. We should note that for a single-layer (i.e., constant-velocity) medium, PWPSM can be replaced by much faster PW Stolt's migration proposed in [25, 72].

5.2 Future work

Several promising research directions can be pursued based on the work presented in this thesis. With respect to the low cost alternative for phase shift migration, future work can be focused on investigating methods to adaptively determine the energy threshold settings (based on the data being processed). The thresholds heavily impact the quality of the reconstructed image and the amount of multiplication savings that can be achieved.

Our second suggestion would be to investigate efficient polar approximations during downward extrapolation. PSM extrapolation affects only the phase of the 2D wavefield spectrum while preserving the amplitude. Therefore by performing computations using the polar representation of the spectrum, complex multiplications during extrapolation can be replaced by real additions [74].

Our final suggestion would be to merge sound speed and thickness estimation into a single optimization problem, as well as use deep learning approaches that reconstruct migrated data using self-tuned neural networks, trained and validated

using appropriate reference datasets.

Appendix A

Imaged target cross-sections after SOS profiling

In this section we show lateral cross-section images and FWHM values for the imaged ball-shaped targets described in Chapter 4 (see section 4.1). The reader can compare the presented images and data with those shown in Figures 4.4(c) and 4.4(d) and Tables 4.4(a), to confirm the accuracy of our SOS profiling approach.

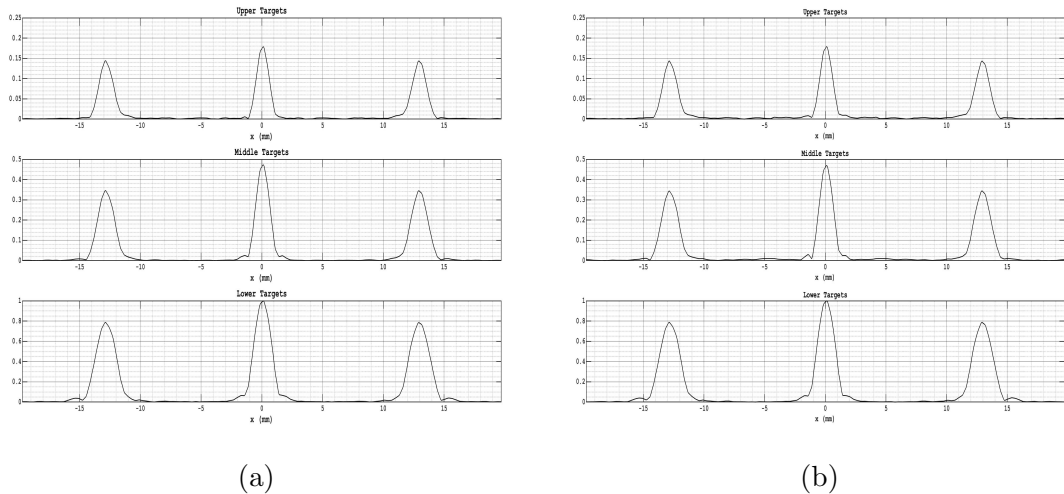


Figure A.1: Lateral cross-section for estimated SOS profile, case 1. (a) Original (PW-PSM), (b) Low-cost (LCPWPSM).

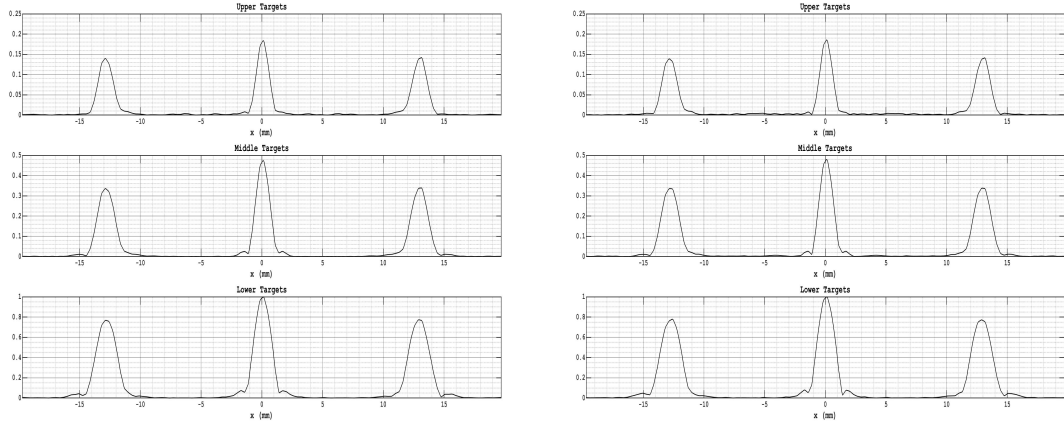
Target group	z mm	FWHM,mm		
		L	C	R
Upper	21.637	1.365	1.182	1.349
Middle	34.650	1.555	1.270	1.553
Lower	47.663	1.874	1.599	1.860

Target group	z mm	FWHM,mm		
		L	C	R
Upper	21.637	1.360	1.179	1.351
Middle	34.727	1.592	1.309	1.589
Lower	47.817	1.909	1.638	1.913

(a)

(b)

Table A.1: Target resolution quality for estimated SOS profile, case 1. (a) Original (PWPSM), (b) Low-cost (LCPWPSM).



(a)

(b)

Figure A.2: Lateral cross-section for estimated SOS profile, case 2. (a) Original (PWPSM), (b) Low-cost (LCPWPSM).

Target group	z mm	FWHM,mm		
		L	C	R
Upper	21.560	1.421	1.167	1.384
Middle	34.496	1.648	1.319	1.627
Lower	47.432	1.954	1.637	1.938

Target group	z mm	FWHM,mm		
		L	C	R
Upper	21.483	1.439	1.180	1.401
Middle	34.342	1.670	1.320	1.646
Lower	47.201	1.950	1.639	1.945

(a)

(b)

Table A.2: Target resolution quality for estimated SOS profile, case 2. (a) Original (PWPSM), (b) Low-cost (LCPWPSM).

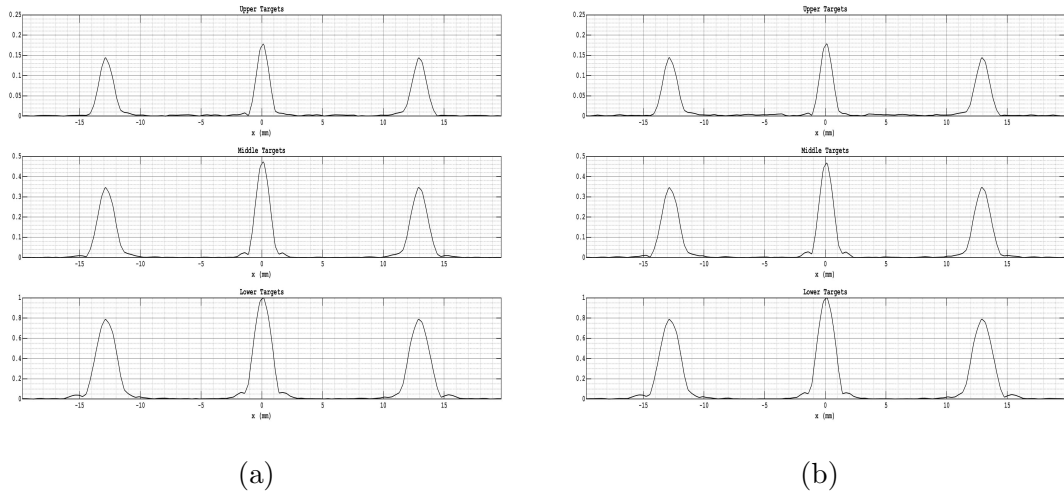


Figure A.3: Lateral cross-section for estimated SOS profile, case 3. (a) Original (PWPSM), (b) Low-cost (LCPWPSM).

Target group	z mm	FWHM,mm		
		L	C	R
Upper	21.637	1.358	1.186	1.343
Middle	34.650	1.593	1.314	1.589
Lower	47.817	1.911	1.638	1.912

(a)

Target group	z mm	FWHM,mm		
		L	C	R
Upper	21.560	1.358	1.186	1.347
Middle	34.650	1.592	1.323	1.589
Lower	47.817	1.910	1.637	1.905

(b)

Table A.3: Target resolution quality for estimated SOS profile, case 3. (a) Original (PWPSM), (b) Low-cost (LCPWPSM).

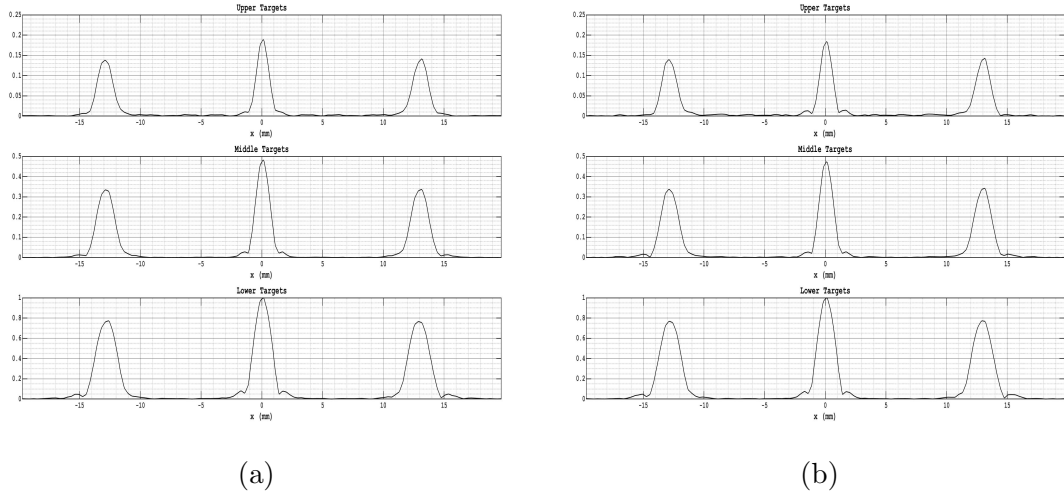


Figure A.4: Lateral cross-section for estimated SOS profile, case 4. (a) Original (PWPSM), (b) Low-cost (LCPWPSM)

Target group	z mm	FWHM,mm		
		L	C	R
Upper	21.560	1.496	1.162	1.438
Middle	34.265	1.689	1.323	1.669
Lower	47.047	1.979	1.642	1.983

(a)

Target group	z mm	FWHM,mm		
		L	C	R
Upper	21.637	1.428	1.172	1.378
Middle	34.419	1.658	1.324	1.632
Lower	47.432	1.955	1.640	1.940

(b)

Table A.4: Target resolution quality for estimated SOS profile, case 4. (a) Original (PWPSM), (b) Low-cost (LCPWPSM).

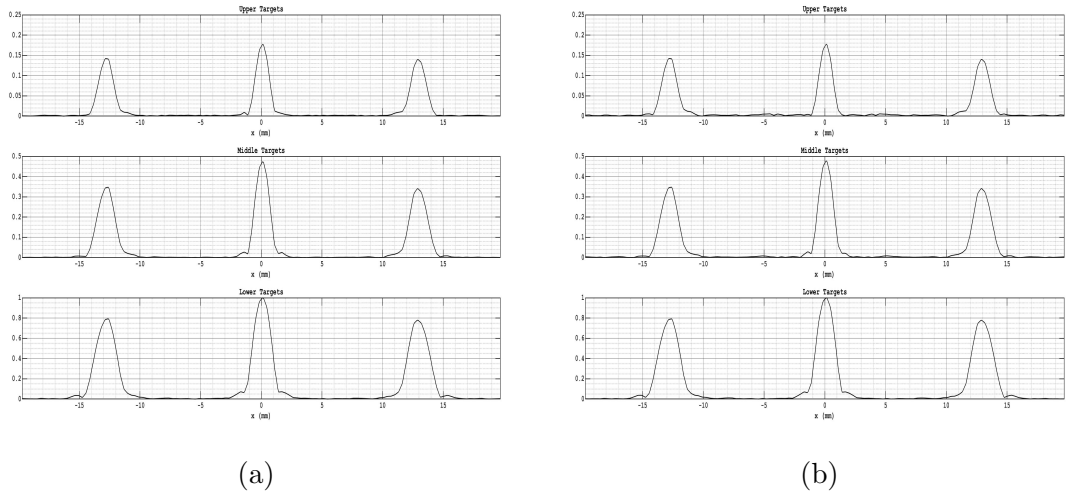


Figure A.5: Lateral cross-section for estimated SOS profile, case 5. (a) Original (PWPSM), (b) Low-cost (LCPWPSM).

Target group	z mm	FWHM,mm		
		L	C	R
Upper	21.714	1.412	1.248	1.427
Middle	34.650	1.644	1.366	1.670
Lower	47.817	1.968	1.685	1.987

(a)

Target group	z mm	FWHM,mm		
		L	C	R
Upper	21.637	1.408	1.246	1.731
Middle	34.650	1.639	1.364	1.665
Lower	47.817	1.966	1.684	1.984

(b)

Table A.5: Target resolution quality for estimated SOS profile, case 5. (a) Original (PWPSM), (b) Low-cost (LCPWPSM).

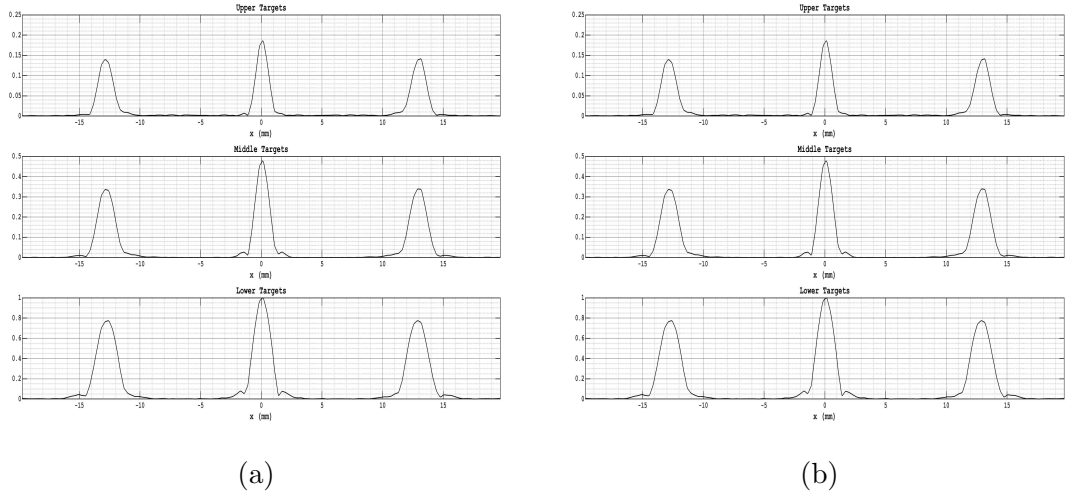


Figure A.6: Lateral cross-section for estimated SOS profile, case 6. (a) Original (PWPSM), (b) Low-cost (LCPWPSM).

Target group	z mm	FWHM,mm		
		L	C	R
Upper	21.560	1.428	1.169	1.397
Middle	34.342	1.659	1.321	1.639
Lower	47.201	1.950	1.637	1.939

(a)

Target group	z mm	FWHM,mm		
		L	C	R
Upper	21.560	1.424	1.168	1.396
Middle	34.342	1.657	1.323	1.637
Lower	47.201	1.948	1.637	1.937

(b)

Table A.6: Target resolution quality for estimated SOS profile, case 6. (a) Original (PWPSM), (b) Low-cost (LCPWPSM).

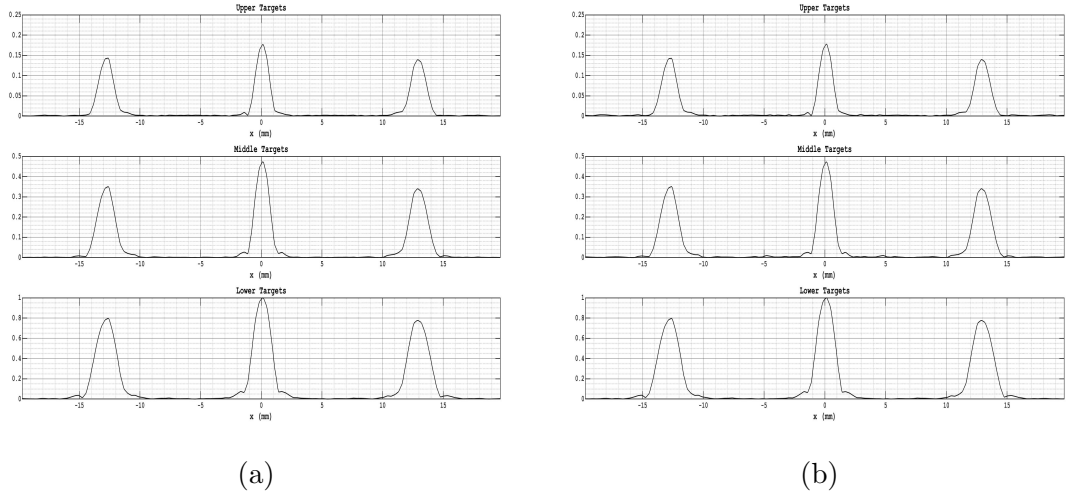


Figure A.7: Lateral cross-section for estimated SOS profile, case 7. (a) Original (PWPSM), (b) Low-cost (LCPWPSM).

Target group	z mm	FWHM,mm		
		L	C	R
Upper	21.714	1.413	1.257	1.437
Middle	34.650	1.647	1.370	1.678
Lower	47.817	1.969	1.689	2.000

(a)

Target group	z mm	FWHM,mm		
		L	C	R
Upper	21.714	1.416	1.258	1.441
Middle	34.650	1.642	1.371	1.673
Lower	47.817	1.968	1.688	1.999

(b)

Table A.7: Target resolution quality for estimated SOS profile, case 7. (a) Original (PWPSM), (b) Low-cost (LCPWPSM).

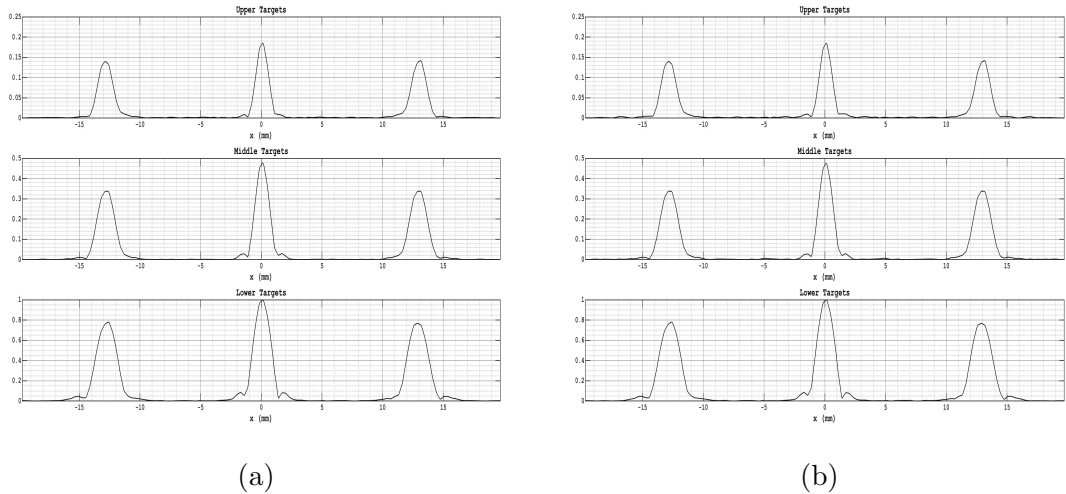


Figure A.8: Lateral cross-section for estimated SOS profile, case 8. (a) Original (PWPSM), (b) Low-cost (LCPWPSM)

Target group	z mm	FWHM,mm		
		L	C	R
Upper	21.714	1.413	1.257	1.437
Middle	34.650	1.647	1.370	1.678
Lower	47.817	1.969	1.689	2.000

(a)

Target group	z mm	FWHM,mm		
		L	C	R
Upper	21.714	1.416	1.258	1.441
Middle	34.650	1.642	1.371	1.673
Lower	47.817	1.968	1.688	1.999

(b)

Table A.8: Target resolution quality for estimated SOS profile, case 8. (a) Original (PWPSM), (b) Low-cost (LCPWPSM).

Appendix B

Overview of Hough transform

In this section, we explain how the Hough transform can be used to detect straight lines. Hough transform is a robust technique developed by Paul Hough (1962) that uses a voting-based procedure to isolate features of a particular shape within an image [65, 75, 76]. At present, the classical Hough transform is most commonly used for detection of lines, circles, ellipses, etc. in object recognition applications. In our case, we use it for detecting lines in line-based end-of-layer boundary detection for layer thickness estimation.

B.1 Theory

In an image plane, a straight line can be described by the following equation with two parameters, slope m and y -intercept b .

$$y = mx + b \quad (\text{B.1})$$

The above form has drawbacks, since it is unable to represent vertical lines ($m = 0$). An alternative would be using the following form:

$$r = x \cos(\theta) + y \sin(\theta) \quad (\text{B.2})$$

Here, the parameters θ and r represent the orientation of a line with respect to the x -axis and the distance from that line to the origin. Figure B.1 shows how points in the image plane can be mapped to the Hough space. Plotting possible (θ, r) values, defined by each (x, y) point in the Cartesian image space, produces sinusoidal curves

in the Hough parameter space. Such a point-to-curve transformation represents the Hough transform for straight lines. When viewed in the Hough parameter space, points which are co-linear (A, B, C in Figure B.1(a)) in the Cartesian image space yield intersecting curves having a common (θ, r) point (Figure B.1(b)).

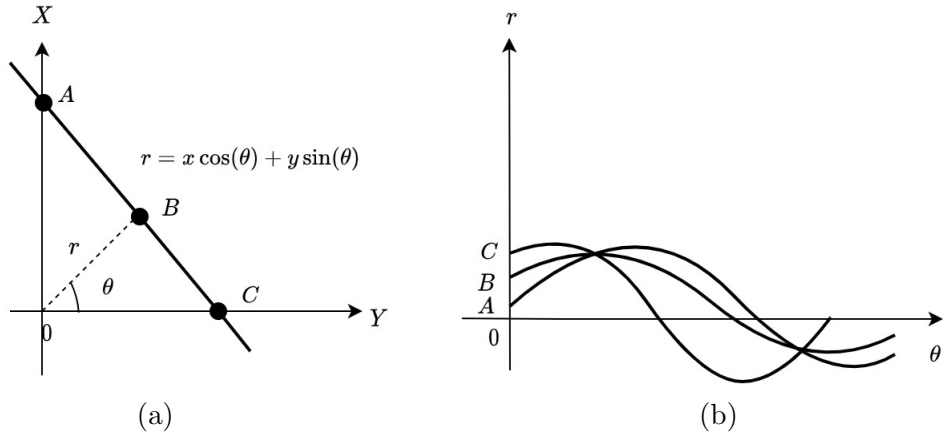


Figure B.1: Parametric Hough transform. (a)Image space, (b) Hough space.

B.2 Implementation

The Hough transform takes a binary edge map (obtained using some feature-detecting operation) as an input and attempts to locate straight lines in that map. In order to detect the presence of a specific line $y = mx + b$ inside the image (the areas where most of the Hough space lines intersect), the Hough transform algorithm uses a two-dimensional array, called accumulator. The resolution of the accumulator determines the precision with which lines can be detected, which corresponds to the number of unknown parameters in the Hough transform problem. As the algorithm runs, each edge point (x, y) is transformed into a discretized (θ, r) curve, and bins in the accumulator are incremented for all lines that pass through that point. Resulting local maxima in the accumulator array represent strong evidence of the existence of straight lines.

The Hough transform is efficient only when most votes fall in a small number of bins, so that they can be easily detected amid the background noise. Much of the efficiency of the Hough transform depends on the quality of input data, i.e., noisy images may cause the Hough transform to perform poorly.

Bibliography

- [1] D. Ensminger and L. J. Bond, *Ultrasonics: Fundamentals, Technologies, and Applications.*, New York, USA: CRC Press, 2011.
- [2] J. Park, J. B. Kang, J. H. Chang, and Y. Yoo, “Speckle reduction techniques in medical ultrasound imaging,” *Biomedical Engineering Letters*, vol. 4, no. 1, pp. 32–40, 2014.
- [3] C. Griffith and R. Nowakowski, “Powering medical ultrasound imaging,” <https://www.mouser.ca/applications/medical-ultrasound-power-supply/>.
- [4] J. A. Jensen, “Medical ultrasound imaging,” *Progress in Biophysics and Molecular Biology*, vol. 93, no. 1-3, pp. 153–165, 2007.
- [5] ——, “Ultrasound imaging and its modeling,” in *Imaging of Complex Media with Acoustic and Seismic Waves.*, Berlin, Germany: Springer, 2002, pp. 135–166.
- [6] H. T. Lutz, “Basics of ultrasound,” in *Manual of Diagnostic Ultrasound in Infectious Tropical Diseases.*, Berlin, Germany: Springer, 2006, pp. 1–19.
- [7] “Physics of ultrasound.”, NYSORA, Feb 2019, <https://www.nysora.com-foundations-of-regional-anesthesia/equipment/physics-of-ultrasound/>.
- [8] R. S. Cobbold, *Foundations of Biomedical Ultrasound.*, Oxford, New York: Oxford University Press, 2006.
- [9] “Basic principles of ultrasound.”, Australian Institute Of Ultrasound Training, 2012, http://www.dccconferences.com.au/lcmc2012/pdf/Phlebology_PrereadingFriday.pdf.
- [10] N. M. Tole and H. Ostensen, *Basic Physics of Ultrasonographic Imaging.*, Geneva, Switzerland: World Health Organization, 2005.

- [11] N. Olympus, “Ultrasonic transducers technical notes,” *Technical brochure: Olympus NDT, Waltham, MA*, 2006.
- [12] S. N. Narouze, *Atlas of Ultrasound-guided Procedures in Interventional Pain Management.*, New York, USA: Springer, 2018.
- [13] S. Hughes, “Medical ultrasound imaging,” *Physics Education*, vol. 36, no. 6, pp. 468–475, oct 2001. [Online]. Available: <https://doi.org/10.1088%2F0031-9120%2F36%2F6%2F304>
- [14] V. Madisetti, *Wireless, Networking, Radar, Sensor Array Processing, and Non-linear Signal Processing.*, Florida, USA: CRC Press, 2009.
- [15] R. Øvland, “Coherent plane-wave compounding in medical ultrasound imaging: Quality investigation of 2d b-mode images of stationary and moving objects.” Master’s thesis, Norwegian University of Science and Technology, Trondheim, Norway, 2012.
- [16] S. Holm, “Digital beamforming in ultrasound imaging,” in *IEEE Nordic Signal Processing Symposium.*, Ålesund, Norway: IEEE, 1994, pp. 228–233.
- [17] M. Tanter and M. Fink, “Ultrafast imaging in biomedical ultrasound,” *IEEE Transactions on Ultrasonics, Ferroelectrics, and Frequency Control*, vol. 61, no. 1, pp. 102–119, 2014.
- [18] M. H. Skjelvareid, T. Olofsson, Y. Birkelund, and Y. Larsen, “Synthetic aperture focusing of ultrasonic data from multilayered media using an omega-k algorithm,” *IEEE Transactions on Ultrasonics, Ferroelectrics, and Frequency Control*, vol. 58, no. 5, pp. 1037–1048, 2011.
- [19] I. Trots, A. Nowicki, M. Lewandowski, and Y. Tasinkevych, “Synthetic aperture method in ultrasound imaging,” in *Ultrasound Imaging*, M. Tanabe, Ed., Rijeka, Croatia: IntechOpen, 2011, ch. 3. [Online]. Available: <https://doi.org/10.5772/15986>
- [20] L. Demi, “Practical guide to ultrasound beam forming: Beam pattern and image reconstruction analysis,” *Applied Sciences*, vol. 8, no. 9, p. 1544, 2018.

- [21] N. T Schiefler, J. M Maia, F. K Schneider, A. J Zimbico, A. A Assef, and E. T Costa, “Generation and analysis of ultrasound images using plane wave and sparse arrays techniques,” *Sensors*, vol. 18, no. 11, p. 3660, 2018.
- [22] G. Montaldo, M. Tanter, J. Bercoff, N. Benech, and M. Fink, “Coherent plane-wave compounding for very high frame rate ultrasonography and transient elastography,” *IEEE Transactions on Ultrasonics, Ferroelectrics, and Frequency Control*, vol. 56, no. 3, pp. 489–506, 2009.
- [23] R. Cohen, Y. Sde-Chen, T. Chernyakova, C. Fraschini, J. Bercoff, and Y. C. Eldar, “Fourier domain beamforming for coherent plane-wave compounding,” in *2015 IEEE International Ultrasonics Symposium (IUS)*., Taipei, Taiwan: IEEE, 2015, pp. 1–4.
- [24] A. Ng and J. Swanevelder, “Resolution in ultrasound imaging,” *Continuing Education in Anaesthesia Critical Care & Pain*, vol. 11, no. 5, pp. 186–192, 2011.
- [25] M. Albulayli, “Migration-based image reconstruction methods for plane-wave ultrasound imaging,” Ph.D. dissertation, University of Victoria, Victoria, Canada, 2018.
- [26] S. H. Gray, J. Etgen, J. Dellinger, and D. Whitmore, “Seismic migration problems and solutions,” *Geophysics*, vol. 66, no. 5, pp. 1622–1640, 2001.
- [27] L. Le Tarnec, S. Muth, E. Montagnon, J. Porée, G. Cloutier, and D. Garcia, “Fourier fk migration for plane wave ultrasound imaging: Theoretical framework,” in *2012 IEEE International Ultrasonics Symposium.*, Dresden, Germany: IEEE, 2012, pp. 2141–2144.
- [28] J. Gazdag, “Wave equation migration with the phase-shift method,” *Geophysics*, vol. 43, no. 7, pp. 1342–1351, 1978.
- [29] D. Garcia, L. Le Tarnec, S. Muth, E. Montagnon, J. Porée, and G. Cloutier, “Stolt’s fk migration for plane wave ultrasound imaging,” *IEEE Transactions on Ultrasonics, Ferroelectrics, and Frequency Control*, vol. 60, no. 9, pp. 1853–1867, 2013.
- [30] M. Albulayli and D. Rakhmatov, “Phase-shift depth migration for plane-wave ultrasound imaging,” in *2018 40th Annual International Conference of the IEEE*

Engineering in Medicine and Biology Society (EMBC)., Honolulu, Hawaii, USA: IEEE, 2018, pp. 911–916.

- [31] A. Hindi, C. Peterson, and R. G. Barr, “Artifacts in diagnostic ultrasound,” *Reports in Medical Imaging*, vol. 6, pp. 29–48, 2013.
- [32] F. W. Kremkau and K. Taylor, “Artifacts in ultrasound imaging.” *Journal of Ultrasound in Medicine*, vol. 5, no. 4, pp. 227–237, 1986.
- [33] M. K. Feldman, S. Katyal, and M. S. Blackwood, “US artifacts,” *Radiographics*, vol. 29, no. 4, pp. 1179–1189, 2009.
- [34] D. Napolitano, C.-H. Chou, G. McLaughlin, T.-L. Ji, L. Mo, D. DeBusschere, and R. Steins, “Sound speed correction in ultrasound imaging,” *Ultrasonics*, vol. 44, pp. e43–e46, 2006.
- [35] M. Anderson, M. McKeag, and G. Trahey, “The impact of sound speed errors on medical ultrasound imaging,” *The Journal of the Acoustical Society of America*, vol. 107, no. 6, pp. 3540–3548, 2000.
- [36] Q. Chen and J. A. Zagzebski, “Simulation study of effects of speed of sound and attenuation on ultrasound lateral resolution,” *Ultrasound in Medicine & Biology*, vol. 30, no. 10, pp. 1297–1306, 2004.
- [37] D. Robinson, J. Ophir, L. Wilson, and C. Chen, “Pulse-echo ultrasound speed measurements: progress and prospects,” *Ultrasound in Medicine & Biology*, vol. 17, no. 6, pp. 633–646, 1991.
- [38] L. Pearson and D. Gardiner, “Quantitative ultrasonic nde,” in *15 th Symposium on Nondestructive Evaluation*, San Antonio, Texas, USA, 1986, pp. 234–255.
- [39] I. Kuo, B. Hete, and K. Shung, “A novel method for the measurement of acoustic speed,” *The Journal of the Acoustical Society of America*, vol. 88, no. 4, pp. 1679–1682, 1990.
- [40] D. K. Hsu and M. S. Hughes, “Simultaneous ultrasonic velocity and sample thickness measurement and application in composites,” *The Journal of the Acoustical Society of America*, vol. 92, no. 2, pp. 669–675, 1992.

- [41] M. Kondo, K. Takamizawa, M. Hirama, K. Okazaki, K. Iinuma, and Y. Takehara, “An evaluation of an in vivo local sound speed estimation technique by the crossed beam method,” *Ultrasound in Medicine & Biology*, vol. 16, no. 1, pp. 65–72, 1990.
- [42] G. Kossoff, “Paper 4.5: Reflection techniques for measurement of attenuation and velocity.” in *Ultrasonic Tissue Characterization.*, US Dept. of Commerce, National Bureau of Standards, 1976, p. 135.
- [43] M. E. Anderson and G. E. Trahey, “The direct estimation of sound speed using pulse-echo ultrasound,” *The Journal of the Acoustical Society of America*, vol. 104, no. 5, pp. 3099–3106, 1998.
- [44] F. R. Pereira, J. C. Machado, and W. C. Pereira, “Ultrasonic wave speed measurement using the time-delay profile of rf-backscattered signals: Simulation and experimental results,” *The Journal of the Acoustical Society of America*, vol. 111, no. 3, pp. 1445–1453, 2002.
- [45] H. Hachiya, S. Ohtsuki, M. Tanaka, and F. Dunn, “Determination of sound speed in biological tissues based on frequency analysis of pulse response,” *The Journal of the Acoustical Society of America*, vol. 92, no. 3, pp. 1564–1568, 1992.
- [46] R. Hatakeyama, N. Tagawa, M. Yoshizawa, and T. Moriya, “Measurement of speed of sound in skull bone and its thickness using a focused ultrasonic wave,” *Japanese Journal of Applied Physics*, vol. 41, no. 5S, p. 3327, 2002.
- [47] B. C. Byram, G. E. Trahey, and J. A. Jensen, “A method for direct localized sound speed estimates using registered virtual detectors,” *Ultrasonic imaging*, vol. 34, no. 3, pp. 159–180, 2012.
- [48] M. Jakovljevic, S. Hsieh, R. Ali, G. Chau Loo Kung, D. Hyun, and J. J. Dahl, “Local speed of sound estimation in tissue using pulse-echo ultrasound: Model-based approach,” *The Journal of the Acoustical Society of America*, vol. 144, no. 1, pp. 254–266, 2018.
- [49] S. J. Sanabria, M. B. Rominger, and O. Goksel, “Speed-of-sound imaging based on reflector delineation,” *IEEE Transactions on Biomedical Engineering*, vol. 66, no. 7, pp. 1949–1962, 2018.

- [50] D. Robinson, F. Chen, and L. Wilson, “Measurement of velocity of propagation from ultrasonic pulse-echo data,” *Ultrasound in Medicine & Biology*, vol. 8, no. 4, pp. 413–420, 1982.
- [51] D. Robinson, C. Chen, and L. S. Wilson, “Image matching for pulse echo measurement of ultrasonic velocity,” *Image and Vision Computing*, vol. 1, no. 3, pp. 145–151, 1983.
- [52] J. Ophir, “Estimation of the speed of ultrasound propagation in biological tissues: A beam-tracking method,” *IEEE Transactions on Ultrasonics, Ferroelectrics, and Frequency Control*, vol. 33, no. 4, pp. 359–368, 1986.
- [53] J. Krucker, J. B. Fowlkes, and P. L. Carson, “Sound speed estimation using automatic ultrasound image registration,” *IEEE Transactions on Ultrasonics, Ferroelectrics, and Frequency Control*, vol. 51, no. 9, pp. 1095–1106, 2004.
- [54] X. Qu, T. Azuma, J. T. Liang, and Y. Nakajima, “Average sound speed estimation using speckle analysis of medical ultrasound data,” *International journal of Computer Assisted Radiology and Surgery*, vol. 7, no. 6, pp. 891–899, 2012.
- [55] M. Razavy, “Determination of the wave velocity in an inhomogeneous medium from the reflection coefficient,” *The Journal of the Acoustical Society of America*, vol. 58, no. 5, pp. 956–963, 1975.
- [56] D. Dameron, “Determination of the acoustic velocity in tissues using an inhomogeneous media model,” *IEEE Transactions on Sonics and Ultrasonics*, vol. 26, no. 2, pp. 69–74, 1979.
- [57] H.-C. Shin, R. Prager, H. Gomersall, N. Kingsbury, G. Treece, and A. Gee, “Estimation of average speed of sound using deconvolution of medical ultrasound data,” *Ultrasound in Medicine & Biology*, vol. 36, no. 4, pp. 623–636, 2010.
- [58] ——, “Estimation of speed of sound in dual-layered media using medical ultrasound image deconvolution,” *Ultrasonics*, vol. 50, no. 7, pp. 716–725, 2010.
- [59] S. M. Riad, “The deconvolution problem: An overview,” *Proceedings of the IEEE*, vol. 74, no. 1, pp. 82–85, 1986.

- [60] M. Cho, L. Kang, J. Kim, and S. Lee, “An efficient sound speed estimation method to enhance image resolution in ultrasound imaging,” *Ultrasonics*, vol. 49, no. 8, pp. 774–778, 2009.
- [61] C. Yoon, Y. Lee, J. H. Chang, T. Song, and Y. Yoo, “In vitro estimation of mean sound speed based on minimum average phase variance in medical ultrasound imaging,” *Ultrasonics*, vol. 51, no. 7, pp. 795–802, 2011.
- [62] A. V. G. De Sousa, W. C. D. A. Pereira, and J. C. Machado, “An ultrasonic theoretical and experimental approach to determine thickness and wave speed in layered media,” *IEEE Transactions on Ultrasonics, Ferroelectrics, and Frequency Control*, vol. 54, no. 2, pp. 386–393, 2007.
- [63] S. J. Park, J. Lee, W. Y. Lee, and Y. Yoo, “Mean sound speed estimation with focusing quality evaluation for medical ultrasound imaging,” in *2011 IEEE International Ultrasonics Symposium.*, Orlando, Florida, USA: IEEE, 2011, pp. 2205–2208.
- [64] J. Lee, Y. Yoo, C. Yoon, and T. Song, “A computationally efficient mean sound speed estimation method based on an evaluation of focusing quality for medical ultrasound imaging,” *Electronics*, vol. 8, no. 11, p. 1368, 2019.
- [65] P. V. Hough, “Method and means for recognizing complex patterns,” Dec. 18 1962, US Patent 3,069,654.
- [66] R. O. Duda and P. E. Hart, “Use of the Hough transformation to detect lines and curves in pictures,” *Communications of the ACM*, vol. 15, no. 1, pp. 11–15, 1972.
- [67] B. Treeby, B. Cox, and J. Jaros, “k-wave a matlab toolbox for the time domain simulation of acoustic wave fields,” *User Manual Version 1. 0. 1*, 2012.
- [68] “Defining an ultrasound transducer example,” http://www.k-wave.org/documentation/example_us_defining_transducer.php.
- [69] T. L. Szabo, *Diagnostic Ultrasound Imaging: Inside Out.*, Oxford, UK: Academic Press, 2004.
- [70] “Simulating b-mode ultrasound images example,” http://www.k-wave.org/documentation/example_us_bmode_linear_transducer.php.

- [71] M. H. Skjelvareid, “Synthetic aperture ultrasound imaging with application to interior pipe inspection,” Ph.D. dissertation, Universitetet of Tromsø, Tromsø, Norway, 2012.
- [72] M. Albulayli and D. Rakhmatov, “Fourier domain depth migration for plane-wave ultrasound imaging,” *IEEE Transactions on Ultrasonics, Ferroelectrics, and Frequency Control*, vol. 65, no. 8, pp. 1321–1333, 2018.
- [73] H. Liebgott, A. Rodriguez-Molares, F. Cervenansky, J. A. Jensen, and O. Bernard, “Plane-wave imaging challenge in medical ultrasound,” in *2016 IEEE International Ultrasonics Symposium (IUS)*., Tours, France: IEEE, 2016, pp. 1–4.
- [74] W. A. Mousa and A. F. Al-Battal, “Computationally efficient phase shift plus interpolation seismic migration method,” *IEEE Geoscience and Remote Sensing Letters*, vol. 17, no. 5, pp. 775–778, 2020.
- [75] J. Yu, J. Duan, and K.-n. Su, “A Hough transform based method for gait feature extraction,” *Journal of Image and Graphics*, vol. 10, pp. 1304–1309, 2005.
- [76] L. G. Shapiro and G. C. Stockman, *Computer Vision.*, New Jersey, USA: Prentice Hall, 2001.